LAPPEENRANTA-LAHTI UNIVERSITY OF TECHNOLOGY LUT

Pekko Jaatinen

DESIGN AND CONTROL OF A PERMANENT MAGNET BEARINGLESS MACHINE

ACTA UNIVERSITATIS LAPPEENRANTAENSIS 879

Pekko Jaatinen

DESIGN AND CONTROL OF A PERMANENT MAGNET BEARINGLESS MACHINE

Dissertation for the degree of Doctor of Science (Technology) to be presented with due permission for public examination and criticism in the Auditorium of the Student Union House at Lappeenranta–Lahti University of Technology LUT, Lappeenranta, Finland on the 29th of November, 2019, at noon.

Acta Universitatis
Lappeenrantaensis 879

Supervisors Professor Olli Pyrhönen
LUT School of Energy Systems
Lappeenranta–Lahti University of Technology LUT
Finland

Dr. Rafal P. Jastrzebski
LUT School of Energy Systems
Lappeenranta–Lahti University of Technology LUT
Finland

Reviewers Univ.-Prof. DI Dr. sc. techn. Wolfgang Amrhein
Institute of Electric Drives and Power Electronics
Johannes Kepler University Linz
Austria

Associate Professor Luca Peretti
Division of Electrical Energy Engineering
KTH Royal Institute of Technology
Sweden

Opponent Associate Professor Luca Peretti
Division of Electrical Energy Engineering
KTH Royal Institute of Technology
Sweden

ISBN 978-952-335-442-5
ISBN 978-952-335-443-2 (PDF)
ISSN-L 1456-4491
ISSN 1456-4491

Lappeenranta–Lahti University of Technology LUT
LUT University Press 2019

Abstract

Pekko Jaatinen
Design and control of a permanent magnet bearingless machine
Lappeenranta 2019
75 pages
Acta Universitatis Lappeenrantaensis 879
Diss. Lappeenranta-Lahti University of Technology LUT
ISBN 978-952-335-442-5, ISBN 978-952-335-443-2 (PDF)
ISSN-L 1456-4491, ISSN 1456-4491

The overall efficiency of high-speed applications can be improved by applying direct drive motor technology. Operating in the high-speed region is a demanding task for the traditional bearing technology. With active magnetic bearings, the rotor can be supported by the magnetic force. As the shaft is rotating in the air, polluting oil lubrication is not needed, and in practice, the rotor system is maintenance free. However, the magnetic bearing construction increases the rotor length, which has an adverse effect on the dynamical behavior of the rotor. Bearingless motor technology combines the levitating force capability of the magnetic bearing with the traditional electrical motor. This integrated structure enables a shorter machine length than with the active magnetic bearings.

Compared with the traditional electrical machine design flow, additional parameters must be taken into account when incorporating the bearingless feature into a motor system. It is important to analyze the interaction of the generated torque and the levitating force. The main objective is to minimize this interaction so that the control of the bearingless machine is more straightforward. The rotor controlled by bearingless motors constitutes a multi-input multi-output system. The system includes cross-couplings between the rotor and the motor units. This issue must be taken account in the control of the bearingless machine.

This doctoral dissertation addresses issues related to the design of a bearingless machine. The main focus is on how to minimize the interaction between torque and levitation force generation. A model-based control approach is adopted to control the bearingless machine by taking into account the cross-couplings. The model is validated by a system identification approach, and the controllers are tested experimentally in the bearingless machine.

Keywords: bearingless, control, design, full-levitation, identification, self-levitation

Acknowledgments

This study was carried out at the Laboratory of Control Engineering and Digital Systems at LUT University, Finland, between years 2014 and 2018.

The author would like to thank Professor Olli Pyrhönen, who has provided a most unique opportunity to work on projects related to magnetic levitation together with the exceptional research team. My sincere thanks go to Dr. Rafal Jastrzebski for his useful comments and fruitful discussions over the past years. For the valuable discussions and the joint effort in the various tasks I would like to thank Mr. Teemu Sillanpää, Mr. Jouni Vuojolainen, and Dr. Niko Nevaranta. I also wish to thank Professor Juha Pyrhönen and Dr. Janne Nerg for their guidance in the machine design. Without the hard work of the guys of LUT Voima this project would not have succeeded. Therefore, my thanks go to Mr. Jouni Ryhänen, Mr. Petri Pesonen, Mr. Antti Suikki, and Mr. Tomi Kangasmäki. I would like to express my sincere gratitude to Dr. Hanna Niemelä for improving the language of this doctoral dissertation.

I am grateful for the guidance that Professor Akira Chiba provided on the design of the bearingless machine during my visit at the Tokyo Institute of Technology. I express my gratitude to Dr. Hiroya Sugimoto and Dr. Kyohei Kiyota for their help with the FEM modeling software.

My special thanks are reserved for Dimmu Borgir, whose music has boosted me through the long nights.

The financial support by the Research Foundation of Lappeenranta University of Technology is gratefully acknowledged.

Lastly, I would like to thank my family for their continuous support during this long project. My deepest gratitude goes to my wife Mira and always so sunny daughter Mimosa.

Pekko Jaatinen
October 2019
Lappeenranta, Finland

”Tee enemmän, nuku vähemmän.”
Tietyn alan dosentti

Contents

Abstract

Acknowledgments

Contents

List of publications 9

Nomenclature 11

1 Introduction 15
- 1.1 Background of the study . . . 16
- 1.2 Motivation and objectives of the study . . . 17
- 1.3 Outline of the doctoral dissertation . . . 19
- 1.4 Scientific contributions . . . 22

2 Bearingless motor design 23
- 2.1 Overview of the electromagnetic design . . . 23
- 2.2 Rotor geometric optimization . . . 25
- 2.3 Design scalability . . . 29
- 2.4 Stator and rotor structure optimization . . . 30
- 2.5 Machine design using the genetic algorithm . . . 33

3 System modeling 37
- 3.1 General modeling guidelines . . . 37
- 3.2 Motor model . . . 38
- 3.3 Force model . . . 38
  - 3.3.1 One-degree-of-freedom AMB . . . 39
  - 3.3.2 Bearingless motor . . . 39
- 3.4 Rotor model . . . 41
  - 3.4.1 Point-mass model . . . 41
  - 3.4.2 Rigid rotor model . . . 41
- 3.5 Actuator model . . . 43

4 Control 45
- 4.1 Overview of the control system . . . 46
- 4.2 Levitation control . . . 47
  - 4.2.1 Axial AMB control . . . 47
  - 4.2.2 Radial position control with pole placement . . . 48
  - 4.2.3 Radial position control with the LQR method . . . 49
  - 4.2.4 Disturbance estimator . . . 50
  - 4.2.5 Radial position control with the H_∞ loop-shaping approach . . . 51
- 4.3 Torque control . . . 53

4.3.1 Scalar control 53
4.4 Experimental results 54
4.4.1 Model validation 54
4.4.2 Levitation experiments 55
4.4.3 Rotation experiments 57

5 Conclusions and future study **61**
5.1 Future study 62

References **63**

Appendix A **68**

Appendix B **71**

Appendix C **73**

Appendix D **75**

Publications

List of publications

This doctoral dissertation is based on the following papers. The rights have been granted by the publishers to include the papers in the dissertation.

Publication I
Jaatinen, P., Jastrzebski, R. P, Sugimoto, H., Pyrhönen, O., and Chiba, A. (2015). Optimization of the rotor geometry of a high-speed permanent magnet bearingless motor with segmented magnets. In *18th International Conference on Electrical Machines and Systems (ICEMS)*, Pattaya, Thailand, pp. 962–967.

Publication II
Jastrzebski, R. P., Jaatinen, P., Sugimoto, H., Pyrhönen, O., and Chiba, A. (2015). Design of a bearingless 100 kW electric motor for high-speed applications. In *18th International Conference on Electrical Machines and Systems (ICEMS)*, Pattaya, Thailand, pp. 2008–2014.

Publication III
Jaatinen, P., Jastrzebski, R. P., Pyrhönen, O., and Chiba, A. (2017). Improving of bearingless 6-slot IPM motor radial force characteristics using rotor skew. In *IEEE International Electric Machines and Drives Conference (IEMDC)*, Miami, FL, USA, pp. 1–7.

Publication IV
Jastrzebski, R. P., Jaatinen, P., Chiba, A., and Pyrhönen, O. (2018). Design optimization of permanent magnet bearingless motor using differential evolution. In *IEEE Energy Conversion Congress and Expo (ECCE)*, Portland, OR, USA, pp. 2327–2334.

Publication V
Jaatinen, P., Vuojolainen, J., Nevaranta, N., Jastrzebski, R., and Pyrhönen, O. (2019). Control system commissioning of fully levitated bearingless machine. *Modeling, Identification and Control*, vol. 40, no. 1, pp. 27–39.

Publication VI
Jaatinen, P., Vuojolainen, J., Sillanpää, T., Nevaranta, N., Jastrzebski, R., and Pyrhönen, O. (2018). Motion control of a dual-motor interior permanent magnet bearingless machine. In *IEEE 18th International Conference on Power Electronics and Motion Control (PEMC)*, Budapest, Hungary, pp. 717–722.

Publication VII
Jaatinen, P., Nevaranta, N., Vuojolainen, J., Jastrzebski, R., and Pyrhönen, O. (2019). H_∞ control of a dual motor bearingless machine. In *IEEE International Electric Machines and Drives Conference (IEMDC)*, San Diego, CA, USA, pp. 875–881.

Nomenclature

Abbreviations

AMB	Active magnetic bearing
DE	Differential evolution
DOF	Degree of freedom
FEM	Finite element method
FPGA	Field programmable gate array
GA	Genetic algorithm
IPM	Interior permanent magnet
LQR	Linear quadratic regulator
MIMO	Multi-input multi-output
PID	Proportional-integral-derivative
PRBS	Pseudorandom binary sequence
RN	Reluctance network
SPM	Surface permanent magnet
VFD	Variable frequency drive

Greek Symbols

α	angle around y-axis	rad
β	angle around x-axis	rad
ϵ	maximum perturbation	-
$\mathbf{\Gamma}$	discrete input matrix	-
$\mathbf{\Phi}$	discrete system matrix	-
μ_0	magnetic constant	Vs/Am
Ω	rotor speed	rad/s
ω	electrical angle	rad/s
ω_{cc}	bandwidth of the current controller	rad/s
ω_{pc}	bandwidth of the position controller	rad/s
ω_{ref}	bandwidth of the reference weight	rad/s
ϕ_{error}	force error angle	deg
ψ	flux linkage	Wb-t
ψ'_{PM}	force constant	N/mm
ρ	scalar gain	-

Symbols

$\mathbf{\Delta}_{M\mathrm{s}}$	perturbed disturbance	-
$\mathbf{\Delta}_{N\mathrm{s}}$	perturbed disturbance	-
$\hat{\mathbf{x}}$	estimated state vector	-
$\mathbf{A}_{\mathrm{r}}$	system matrix of AMB rotor system	-
$\mathbf{A}$	state matrix	-
$\mathbf{A}_{\mathrm{d}}$	disturbance system matrix	-

$\mathbf{B}_{\mathrm{r}}$	input matrix of AMB rotor system	-
$\mathbf{B}$	input matrix	-
$\mathbf{C}_{\mathrm{r}}$	output matrix of AMB rotor system	-
$\mathbf{C}$	output matrix	-
$\mathbf{C}_{\mathrm{D}}$	disturbance output matrix	-
$\mathbf{D}$	feedforward matrix	-
$\mathbf{D}_{\mathrm{r}}$	damping matrix	-
$\mathbf{F}$	force vector	N
$\mathbf{G}$	system model	-
$\mathbf{G}_{\mathrm{a}}$	transfer function of the inner control loop	-
$\mathbf{G}_{\mathrm{r}}$	gyroscopic matrix	-
$\mathbf{G}_{\mathrm{s}}$	shaped open-loop system model	-
$\mathbf{I}$	identity matrix	-
$\mathbf{K}$	feedback gain matrix	-
$\mathbf{K}_1$	reference gain matrix	-
$\mathbf{K}_2$	feedback gain matrix	-
$\mathbf{K}_{\mathrm{I}}$	integrator gain matrix	-
$\mathbf{K}_{\mathrm{i}}$	current stiffness matrix	N/A
$\mathbf{K}_{\mathrm{x}}$	position stiffness matrix	N/mm
$\mathbf{L}$	state estimator gain matrix	-
$\mathbf{M}$	mass matrix	-
$\mathbf{M}_{\mathrm{s}}$	coprime of system model	-
$\mathbf{N}_{\mathrm{s}}$	coprime of system model	-
$\mathbf{q}$	rotor displacement vector	-
$\mathbf{Q}_1$	state weight matrix	-
$\mathbf{Q}_2$	input weight matrix	-
$\mathbf{T}_{\mathrm{bc}}$	transformation matrix	-
$\mathbf{T}_{\mathrm{cs}}$	transformation matrix	-
$\mathbf{u}$	input vector	-
$\mathbf{w}$	disturbance vector	-
$\mathbf{W}_1$	diagonal weight matrix	-
$\mathbf{W}_{\mathrm{i}}$	input filter matrix	-
$\mathbf{W}_{\mathrm{ref}}$	reference filter matrix	-
$\mathbf{x}$	state vector	-
$\mathbf{x}_d$	disturbance state vector	-
$\mathbf{y}$	output vector	-
a	distance to motor location	mm
A_{a}	pole area	m^2
b	distance to motor location	mm
C	rotor clearance	mm
c	distance to sensor location	mm
D	rotor displacement	mm
d	distance to motor location	mm
d_{i}	excitation signal to plant input	-

d_o	excitation signal to plant output	-
f	force	N
i	current	A
i_bias	bias current	A
I_x	rotor inertia with respect to the x-axis	kgm^2
I_y	rotor inertia with respect to the y-axis	kgm^2
I_z	rotor inertia with respect to the z-axis	kgm^2
i_c	control current	A
J	inertia	kgm^2
k	discrete time	s
k_i	current stiffness	N/A
k_x	position stiffness	N/mm
L	inductance	H
m	mass	m
M'	derivative of mutual inductance	H/mm
n	number of turns	-
p	pole pair number	-
q	rotor displacement	mm
R	resistance	Ohm
r	reference input	-
s	air-gap distance	mm
s_0	nominal air gap	mm
t	continuous time	s
t_e	torque	Nm
u	voltage	V
u_ex	input with excitation signal	-
w_a1	prefilter parameter	rad/s
w_a2	prefilter parameter	rad/s
w_b	prefilter parameter	rad/s
w_c	prefilter parameter	rad/s
x	rotor position in the x-axis	mm
y	rotor position in the y-axis	mm

Subscripts

d	direct axis
D-end	machine D-end
dis	displacement
I	integrator
L	levitation winding
max	maximum
mech	mechanical
min	minimum
n	input or output vector size

ND-end	machine ND-end
PM	permanent magnet
q	quadrature axis
r	rotor reference frame
ref	reference
T	torque winding
x	x-axis
y	y-axis
z	z-axis

Other Symbols

$\mathcal{J}$	cost function	-

1 Introduction

Applications powered by electrical motors consume more than half of the electrical energy produced in the world (Kultere and Presch, 2018). Over the past few years, along with global trends of sustainable energy consumption and production, regulations related to electrical motor efficiency have tightened, and consequently, the efficiency of machines has improved. However, regardless of the application, an efficiency analysis should be performed considering the transmission as a whole. For example, many fans and high-speed compressors are driven in a nonoptimal operating point through a gearbox system. At the present time, gearboxes can be replaced with direct-drive motor technology. The operating point of an electrical machine can easily be adjusted with a variable frequency drive (VFD). To further improve the electrical machine efficiency and minimize the overall physical footprint, a high-speed design approach can be adopted. Compressor applications, in particular, benefit from high rotational speeds. For instance, by increasing the rotational speed of the compressor system, a three-stage compressor can be reduced to a two-stage one, the compression ratio remaining the same.

It is well known that operation in a high-speed region is a demanding task for traditional bearing solutions. In general, with respect to the controller and the inverter, the high-speed region can be defined to be over 20 000 r/min (Pyrhönen, 1991). A more descriptive parameter to determine the high-speed region is the peripheral speed of the rotor. Considering the mechanical and maximum stress, a common maximum limit for the peripheral speed is 200 m/s (van der Geest et al., 2015; Miller, 2010). The rotor peripheral speed determines the absolute maximum rotational speed as it influences the stress of the rotor material. Operation in the high-speed region sets a strict requirement for the bearing solution to be used. Mechanical bearings are prone to wear at high operating speeds, which has an impact on the maintenance interval. The speed range can be extended with ceramic bearings; however, a need for regular maintenance is still present. An alternative bearing solution is the fluid film bearing, where oil is constantly pumped into the bearing. In air compressor applications, in particular, oil is an unwanted substance in the air stream, and therefore, the system requires additional oil filters.

High-speed applications can be equipped with active magnetic bearings (AMBs) to replace traditional retainer bearings. In this solution, the rotor is levitated with electromagnets, and thus, there is no physical contact between the stator and the rotor. There is no mechanical contact either, and therefore, the bearing solution is maintenance free in practice. With AMBs, the rotational speed is only limited by the strength of the rotor structure. A drawback of the AMBs is that they increase the rotor length as the additional active parts require space on the rotor. An alternative option is to apply bearingless or self-levitation motor technology. In this approach, the motor unit produces both the torque and the levitating force. In a basic construction, this can be achieved by two different winding sets wound on one stator unit. A further benefit of a bearingless motor approach is that standard industrial VFDs can also be used for the levitation winding control. A bearingless machine is a more integrated system compared with a traditional AMB rotor system solution. Overall, a bearingless system has a lower component count and a smaller footprint and provides better rotor dynamics.

In this doctoral dissertation, the design requirements of the interior permanent magnet (IPM) bearingless machine are studied. In addition, the research considers modeling and control aspects of this machine type. Further on in this chapter, the background, motivation, and objectives of this study are presented. Moreover, seven publications comprising this study are introduced. The rest of this work is divided into four chapters including conclusions.

1.1 Background of the study

In 1842, a British mathematician Samuel Earnshaw published his theorem where he states that there is no stable or static position to levitate a permanent magnet (Earnshaw, 1842). In other words, to levitate a ferromagnetic object in a magnetic field, at least one degree of freedom (DOF) has to be actively controlled. Owing to the limitations of the technology available, it took almost a century to achieve practical results related to magnetic levitation. The first studies on a closed-loop controlled magnetic levitation system date back to the 1930s. Research into levitating and rotating a small ferromagnetic object at 1200 r/min was conducted in (Holmes, 1937). From the 1970s onwards there has been a steady growth in publications related to the study of active magnetic bearings. As a result of the development in the digital electronics and the digital control, the interest in magnetic levitation accelerated in the 1980s.

A traditional bearing concept of a horizontal-oriented electrical machine includes two mechanical bearings. These mechanical bearings can be replaced with AMBs that levitate the rotor in the radial direction. Typically, an axial magnetic bearing is also needed to control the axial movement of the rotor. Less commonly, conical bearings or hybrid axial-radial AMBs are applied (Amati et al., 2016; Sikora and Pilat, 2018). Fig. 1.1 depicts the general structure of an electrical machine equipped with AMBs. It is clearly seen that adding AMBs to the system increases the axial length of the rotor.

An alternative option to the AMB rotor system is to equip the rotor with self-levitation or bearingless motor technology. A bearingless motor is a combination of a traditional electrial motor and a radial AMB. The history of bearingless motors dates back to the 1980s. At that time, Professor Akira Chiba was conducting his PhD research. The idea of the bearingless machine started to evolve from the magnetic attractive force between the rotor and the stator; this force was noticeable when the bearing housing bolts were loose (Chiba et al., 2005). In the year 1989, a patent related to the general idea of bearingless machines was filed.

Since then, different bearingless machine types have been studied including induction machines (Chiba, Power, and Rahman, 1991a,b), reluctance machines (Chiba et al., 1991c), switched-reluctance machines, permanent magnet machines divided into surface perma-

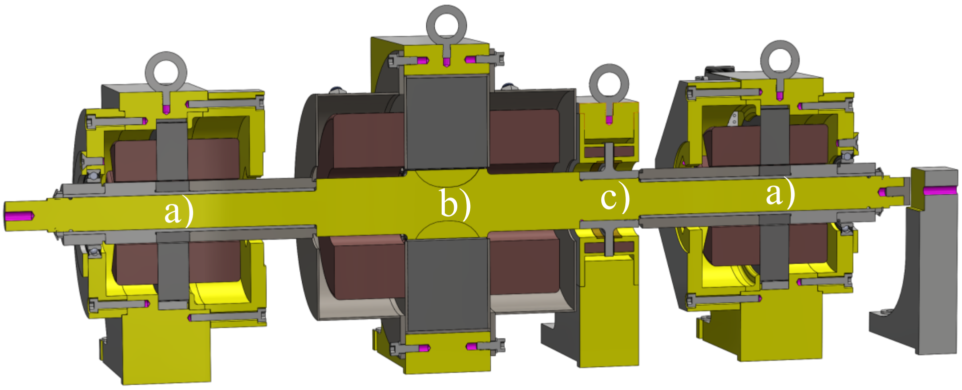

Figure 1.1. Example of an AMB rotor system. a) Radial magnetic bearings, b) solid-rotor induction machine, and c) axial magnetic bearing.

nent magnet (SPM) (Tetsuo Ohishi and Dejima, 1994; Ooshima et al., 1994), and IPM types (Okada et al., 1996). In addition to these, the bearingless function has been included in some uncommon machine types. A homopolar bearingless machine consists of two motor units, where the flux is passing through the stator back (Michioka et al., 1996; Ichikawa et al., 2001). In the consequent type of permanent magnet bearingless machine, the rotor magnets have the same polarity (Amemiya et al., 2005). The benefit of a structure of this kind is that the angle measurement is not needed. Disc-shaped rotors constitute a branch of bearingless machines of their own (Gruber et al., 2009, 2015).

A common winding structure in the bearingless machine is to have two separate three-phase winding sets for the torque and levitation functions. Alternative winding structures have been proposed, such as the bridge-configured polyphase winding structure, where the torque winding is divided into two paths, and an external isolated power supply produces the levitating current (Khoo, 2005). Middle-point current injection has been proposed where an external power supply is connected between the motor windings (Chiba et al., 2011). A parallel winding configuration is presented in (Oishi et al., 2013). Different winding configurations have been presented in the literature; this work focuses on the analysis of a separate three-phase winding scheme for generation of torque and levitation force.

1.2 Motivation and objectives of the study

Minimization of the overall axial length of the high-speed machine is beneficial as the rotor critical speed will increase. The complexity of a high-speed electrical machine with a magnetically levitated rotor system can be reduced by applying the bearingless technology. For example, the evolution of high-speed compressor systems is illustrated in Fig. 1.2. It can be seen that when the mechanical complexity of the system decreases and the integration level increases, higher operating speeds can be achieved.

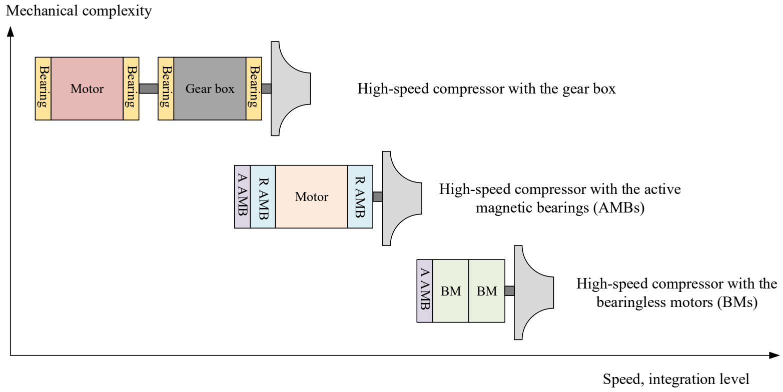
Mechanical complexity
Bearing
Motor
Bearing
Bearing
Gear box
Bearing
High-speed compressor with the gear box
A AMB
R AMB
Motor
R AMB
High-speed compressor with the active magnetic bearings (AMBs)
A AMB
BM
BM
High-speed compressor with the bearingless motors (BMs)
Speed, integration level

Figure 1.2. Evolution of the system integration. The notation ‘A AMB’ refers to an axial AMB and ‘R AMB’ to a radial AMB.

The objective of this study is to optimize the bearingless electrical machine design for a high-speed application and control it with model-based control methods. The selection of the bearingless machine type is based on the levitating force production capabilities and the overall system controllability. A separate winding construction is selected as it is straightforward to assemble and the control of torque and levitation generation can be easily separated. The radial force generation capabilities of a surface permanent magnet (SPM) and an interior permanent magnet (IPM) bearingless motors are studied in (Tetsuo Ohishi and Dejima, 1994). The induction-type bearingless motor generates the highest radial force. However, the controllability of this kind of bearingless machine is problematic with a standard squirrel cage rotor structure (Chiba and Fukao, 1998). The IPM-type bearingless machine is selected as it is capable of generating a higher radial force than the SPM type. Furthermore, the rotor structure with embedded magnets is easier to manufacture and the iron protects the permanent magnets from demagnetization and excessive eddy current losses. The minimum pole numbers for the winding sets are two and four. To minimize the force ripple without any special rotor construction, the two-pole winding is selected for the levitation windings (Matsuzaki et al., 2012). A rotor structure where the air gap is placed between the interior magnet poles is selected to further optimize the rotor controllability, even though some of the radial-force-generating capabilities are lost (Ooshima et al., 2004). With this structure, the dq inductance is more uniform. With the described analysis, the IPM-type bearingless machine is selected, the design of which is further optimized keeping the controllability in mind.

A rotor system with bearingless motor units is shown in Fig. 1.3. When comparing this construction with the AMB system, the benefits are clear. Bearingless motor technology enables an overall more compact machine structure. The presented system consists of several components that have dynamical properties. These components together comprise a multi-input multi-output (MIMO) control system. For these reasons, the model-based control approach is justified in order to provide more accurate control performance.

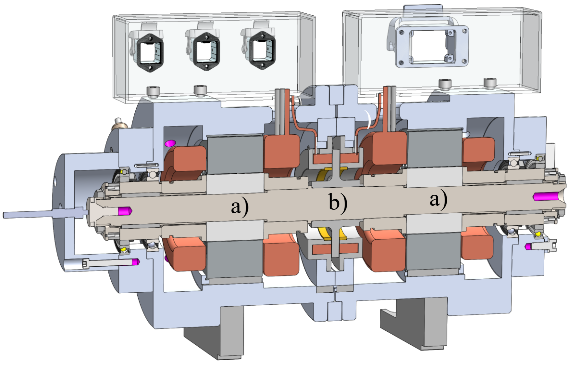

Figure 1.3. Example of a bearingless rotor system. a) Bearingless motor unit and b) axial magnetic bearing.

1.3 Outline of the doctoral dissertation

In this doctoral dissertation, design- and control-related issues of a high-speed permanent magnet bearingless machine are studied. More precisely, the focus is on a machine of an IPM type. The design part of this work concentrates on optimization of the IPM bearingless machine and ensuring the functionality of the machine. Furthermore, the scalability of the proposed design for higher powers is analyzed besides automation of the design process by using genetic algorithms. A model-based control approach is introduced for the permanent magnet bearingless machine. Together with the system identification method, several controllers are experimentally verified.

The main contributions of this doctoral dissertation are presented in the following publications:

Publication I concentrates on rotor optimization to minimize the force error angle. To this end, it is important to analyze the generated force vectors. With this analysis, the functionality of the levitation feature is ensured. The bearingless machine is manufactured based on the design presented in this publication. The experimental results reported in later publications are conducted with this test machine.

Publication II focuses on scaling of the machine design presented in **Publication I** for a higher power level. This paper concentrates on optimization of the overall efficiency of the 100 kW IPM bearingless machine. The force error angle is further minimized by applying stator skew.

Publication III presents a tooth-coil-wound stator for the machine discussed in **Publication I** to further reduce the machine axial length. This is achieved by a smaller end winding length of the tooth coil. Additional optimization is needed to reduce the force error angle, which is enlarged by the increased harmonics in the air gap. Stator and rotor skew is proposed to minimize the force error angle.

Publication IV addresses the optimization problem of permanent magnet bearingless machines. Considering the design from the aspects of torque and force generation, a multivariable problem is formed. By introducing a genetic algorithm in the design flow, the optimization of the full design can be automated. Genetic algorithms are incorporated in the initial design and in the finite element method (FEM) design phase. The outcome of the FEM design is verified by experimental measurements.

Publication V reports a model-based control for the bearingless machine designed in **Publication I**. Modeling of the bearingless rotor system by adopting a rigid rotor approach is carried out. Pole placement and linear quadratic regulator (LQR) based MIMO controllers are synthesized. The rotor model is validated by the system identification method using step sine and binary pseudorandom excitation signals. Finally, the controller performance is verified by lift-up tests and a rotational test.

Publication VI investigates a MIMO LQR radial controller with a disturbance estimator. Rotor vibration is analyzed during an experimental test, and the results are compared with the vibration limits defined by an ISO standard (ISO 14839-3:2004(E), 2004).

Publication VII studies the robust control approach applied to a bearingless machine with levitation control. A loop-shaping H_∞ controller is synthesized and the performance is compared with a PID controller. The output sensitivity of the controllers is compared with respect to the levels given in the ISO standard. The output sensitivity of the controllers is measured by a system identification method by applying a binary pseudorandom excitation signal.

The author of this doctoral dissertation is the main contributor in **Publications I, III, V–VII**. The scaled bearingless motor in **Publication II** is based on the author's design. In **Publication IV**, the author is responsible for conducting the practical experiments. The system identification procedures presented in **Publications V–VII** are the work of Mr. Jouni Vuojolainen. The practical measurements presented in this doctoral dissertation are entirely conducted by the author of this study.

The author has also been the main or coauthor in the following publications. These papers are listed here but are not discussed in detail in this doctoral dissertation.

VIII. Jaatinen, P., Jastrzebski, R., Lindh, T., and Pyrhönen, O. (2013). Implementation of a flux-based controller for active magnetic bearing system. In *IEEE International Conference on Industrial Informatics (INDIN)*, Bochum, Germany, pp. 141–145.

IX. Jastrzebski, R., Smirnov, A., Nerg, J., Jaatinen-Värri, A., Jaatinen P., Lindh, T., Pyrhönen, O., Sopanen, J., and Backman, J. (2013). Laboratory testing of an active magnetic bearing supported permanent magnet 3.5 kW blower prototype. In *15th European Conference On Power Electronics And Applications (EPE)*, Lille, France, pp. 1–9.

X. Jastrzebski, R., Matusiak, D., Sillanpää, T., Romanenko, A., Jaatinen, P., Tolsa, K., Lindh, T., and Pyrhönen, O. (2014). Modelling and evaluation of radial-axial PCB capacitive position sensor prototype. In *16th European Conference On Power Electronics And Applications (EPE)*, Lappeenranta, Finland, pp. 1–8.

XI. Jaatinen, P., Sillanpää, T., Jastrzebski, R., Sikanen, E., and Pyrhönen, O. (2016). Automated parameter identification platform for magnetic levitation systems: case bearingless machine. In *Proc. of 15th International Symposium on Magnetic Bearings (ISMB)*, Kitakyushu, Japan, pp. 275–281.

XII. Jastrzebski, R., Jaatinen, P., and Pyrhönen, O. (2016). Modelling and control design simulations of permanent magnet flux-switching linear bearingless motor. In *Proc. of 15th International Symposium on Magnetic Bearings (ISMB)*, Kitakyushu, Japan, pp. 296–303.

XIII. Jastrzebski, R., Jaatinen, P., and Pyrhönen, O. (2016). Efficiency of buried permanent magnet type 5 kW and 50 kW high-speed bearingless motors with 4-pole motor windings and 2-pole suspension windings. In *Proc. of 15th International Symposium on Magnetic Bearings (ISMB)*, Kitakyushu, Japan, pp. 172–179.

XIV. Jaatinen, P., Jastrzebski, R., and Pyrhönen, O. (2016). Comparison of winding arrangements of a high-speed interior permanent magnet bearingless machine. In *19th International Conference on Electrical Machines and Systems (ICEMS)*, Chiba, Japan, pp. 1–6.

XV. Jastrzebski, R., Sillanpää, T., Jaatinen, P., Smirnov, A., Vuojolainen, J., Lindh, T., Laiho, A., and Pyrhönen O. (2016). Automated design of AMB rotor systems with standard drive, control software and hardware technologies. In *Proc. of 15th International Symposium on Magnetic Bearings (ISMB)*, Kitakyushu, Japan, pp. 467–473.

XVI. Jastrzebski, R., Vuojolainen, J., Jaatinen, P., Sillanpää, T., and Pyrhönen, O. (2016). Commissioning of modular 10 kW magnetically levitated test rig. In *19th International Conference on Electrical Machines and Systems (ICEMS)*, Chiba, Japan, pp. 1–6.

XVII. Sikanen, E., Jastrzebski, R., Jaatinen, P., Sillanpää, T., Smirnov, A., Sopanen, J., and Pyrhönen, O. (2016). Mechanical design of reconfigurable active magnetic bearing test rig. In *Proc. of 15th International Symposium on Magnetic Bearings (ISMB)*, Kitakyushu, Japan, pp. 331–337.

XVIII. Jastrzebski, R., Jaatinen, P., Pyrhönen, O., and Chiba, A. (2017). Current injection solutions for active suspension in bearingless motor. In *19th European Conference On Power Electronics And Applications (EPE)*, Warsaw, Poland, pp. 1–8.

XIX. Jastrzebski, R., Jaatinen, P., Pyrhönen, O., and Chiba, A. (2017). Design of 6-slot inset PM bearingless motor for high-speed and higher than 100 kW applications. In *IEEE International Electric Machines and Drives Conference (IEMDC)*, Miami, FL, USA, pp. 1–6.

XX. Jastrzebski, R., Jaatinen, P., and Pyrhönen, O. (2017). Modeling and control design simulations of a linear flux-switching permanent-magnet-levitated motor. *Mechanical Engineering Journal*, vol. 4, issue 5, pp. 1–12.

XXI. Subhadyuti, S., Jastrzebski, R., Kepsu, D., Zenger, K., Jaatinen, P., and Pyrhönen, O. (2018). Modelling & model-based control of a bearingless 100 kW electric motor for high-speed applications. In *20th European Conference On Power Electronics And Applications (EPE)*, Riga, Latvia, pp. 1–10.

XXII. Nevaranta, N., Jaatinen, P., Gräsbeck, K., and Pyrhönen, O. (2019). Interactive learning material for control engineering education using Matlab live scripts. In *IEEE 17th International Conference on Industrial Informatics (INDIN)*, Helsinki-Espoo, Finland, pp. 1–6.

XXIII. Jaatinen, P., Nevaranta, N., Vuojolainen, N., Lindh, T., and Pyrhönen, O. (2019). Monitoring concept for a high-speed machine application with a magnetically levitated rotor system. In *45th Annual Conference of the Industrial Electronics Society (IECON)*, Lisbon, Portugal, pp. 1–6.

1.4 Scientific contributions

The main scientific contributions of this doctoral dissertation are:

- Minimization of the force error angle by optimization of the rotor geometry and application of stator and rotor skew. Additionally, the stability criteria of the force error angle are experimentally verified.
- The scalability of the proposed bearingless machine construction is analyzed up to the highest power bearingless motor present in the world at the time of this study.
- Automation of the bearingless motor design process by using genetic algorithms.
- Identification of bearingless rotor dynamics by using system identification methods such as step sine and binary pseudorandom excitation.
- A model-based optimal control approach including LQR and H_∞ is applied to regulate the rotor radial position in four degrees of freedom.

2 Bearingless motor design

A general design flow of torque production in a bearingless machine follows the same principles as in the traditional electrical machines (Pyrhönen et al., 2013). An integrated levitation function adds an iterative loop to the design flow where the performance of the levitation is evaluated. There is cross-coupling present between the both functions. This makes the full design flow a multivariable iterative process. The main target is to achieve the best design for levitation and torque production while minimizing the magnetic cross-coupling. The general design flow is presented in Fig. 2.1.

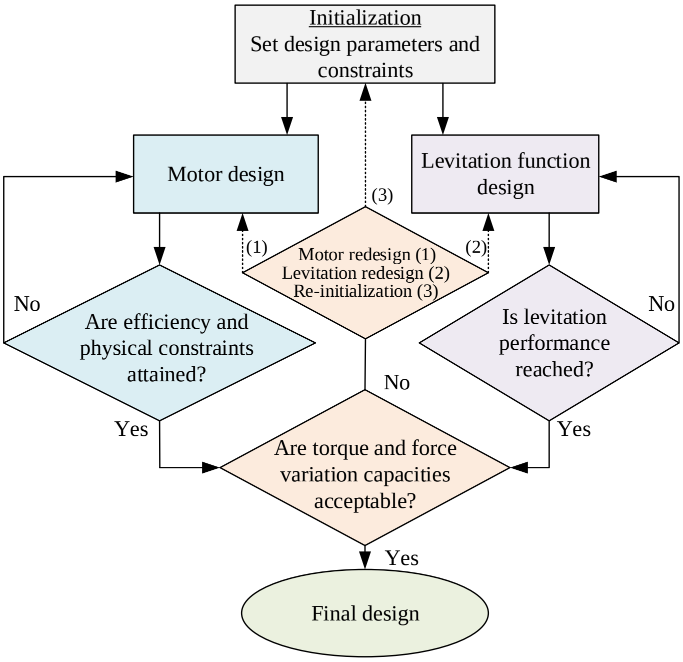
Initialization
Set design parameters and constraints
Motor design
Levitation function design
(3)
(1)
(2)
Motor redesign (1)
Levitation redesign (2)
Re-initialization (3)
No
Are efficiency and physical constraints attained?
Is levitation performance reached?
No
No
Yes
Yes
Are torque and force variation capacities acceptable?
Yes
Final design

Figure 2.1. General design flow of the bearingless machine.

In this doctoral dissertation, the analysis is particularly focused on a double-winding scheme of a dual motor interior permanent magnet bearingless machine.

2.1 Overview of the electromagnetic design

In the rotating electrical machine design, the objective is to meet the requirements for speed, power, and torque. By including an additional winding to produce radial force, the bearingless motor is formed. The operating principle of the bearingless motor is shown in Fig. 2.2. The inner two-pole winding generates the magnetic flux to produce the radial force. The outer four-pole winding is the motor winding to produce the torque. With the levitation winding, the air-gap flux is intentionally altered to be nonsymmetrical to produce radial force in a certain direction. Fig. 2.2 shows how the air-gap flux is increased on the one side and reduced on the opposite side of the air gap. The radial force is produced in the direction of the arrow. By altering the magnitude and angle of the current vector in the levitation winding with respect to the rotor angle, the radial force can be produced in any angle.

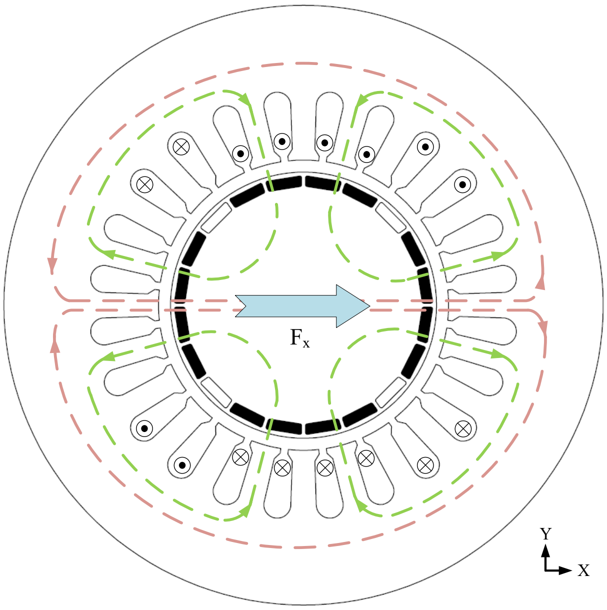

Figure 2.2. Principle of generating radial force in a bearingless machine in the x-axis direction. The winding system is presented in the two-phase form to simplify the drawing. The outer winding layer is the four-pole torque winding, and the inner layer is the two-pole levitation winding.

To be able to produce radial force in addition to torque, a correct winding scheme must be selected. The number of pole pairs of the levitation winding has to be ± 1 compared with the pole pair number of the torque winding (Chiba et al., 2005). This is valid with the double winding scheme. The key issue in the design of a bearingless machine is to analyze the force error angle. This angle is determined in Fig. 2.3, where the force in the x-axis is the target direction. However, there is also a disturbance force present in the y-axis. The force error angle describes how much disturbing force is present. The main source of the force error angle is caused by the machine design, that is, how well the cross-coupling is minimized between the winding sets. The maximum error angle can be 17 degrees, which is the stability limit (Chiba et al., 2005). As a rule of thumb, the target of the error angle should be less than 5 degrees to guarantee stability. Delays in the control system and the operating point of the motor can cause an increase in the force error angle. The maximum error angle can be determined by an experimental test. The result of the test is presented in Fig. 2.4. In this experiment, the feedback signal of the rotor angle is set to a constant value. The force error angle is then produced by rotating the rotor manually until the control system starts to drift towards the unstable state. It is seen that when the rotor angle reaches the value of 16.7 degrees, the rotor position control starts to oscillate. This confirms the analytical analysis of the stability limit presented in (Chiba et al., 2005).

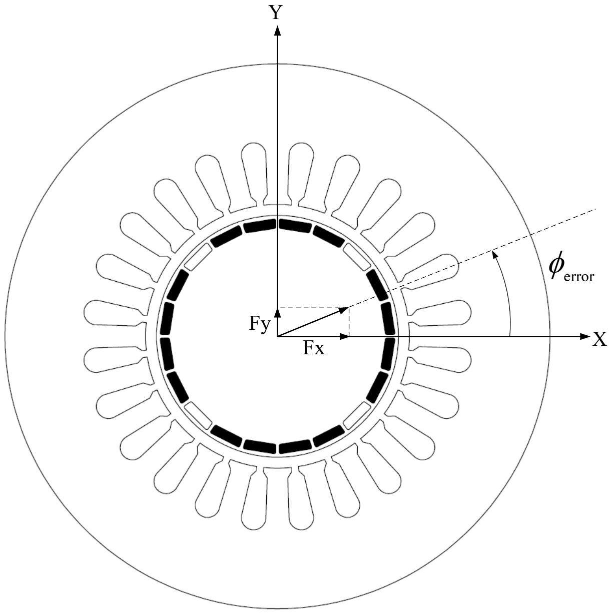

Figure 2.3. Graphical presentation of the force error angle.

Several aspects have to be taken into account in the design phase of the bearingless motor. The force error angle should be minimized to ensure the stability and controllability of the bearingless motor. The force ripple should be inspected, as a linear behavior is desired. The force required to levitate the rotor should be evaluated in a lift-up situation to guarantee that the magnetic pull and gravity can be overcome. The research methodology is based on the initial analytical model, which is further analyzed in the FEM software. Based on the optimized FEM design, a prototype machine is manufactured. The prototype machine is used to verify the FEM analysis result by experimental tests.

2.2 Rotor geometric optimization

In **Publication I**, the rotor structure of the interior permanent magnet bearingless motor was optimized with the FEM software. The designed bearingless machine construction includes two motor units with an axial AMB. The target operating speed of the machine is 30000 r/min and the power per motor unit is 5 kW. The parameters of the machine can be found in Appendix A. The main aim was to minimize the force error angle. This optimization problem was approached by quantitatively comparing eight different rotor structures with segmented magnets. The target of this approach was to find the optimal magnet pole pitch angle. The configurations of the rotor magnet structures are presented

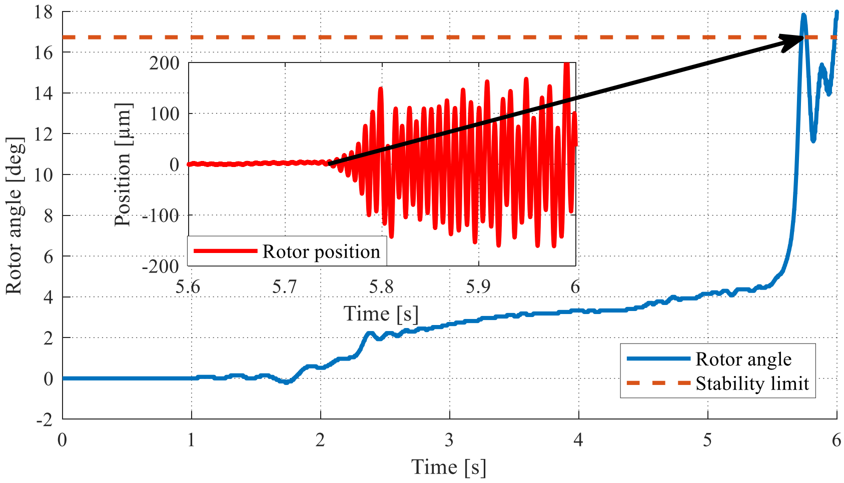

Figure 2.4. Limit for the force error angle determined by the experimental test. The rotor is turned manually when the angle feedback in the controller is set to a constant value. The nonlinear behavior and the sudden increase and vibration of the rotor angle after 5.5 s are caused by the cogging torque of the rotor magnets.

in Fig. 2.5. The limits on the number of magnets are based on the mechanical strength of the rotor together with the manufacturability.

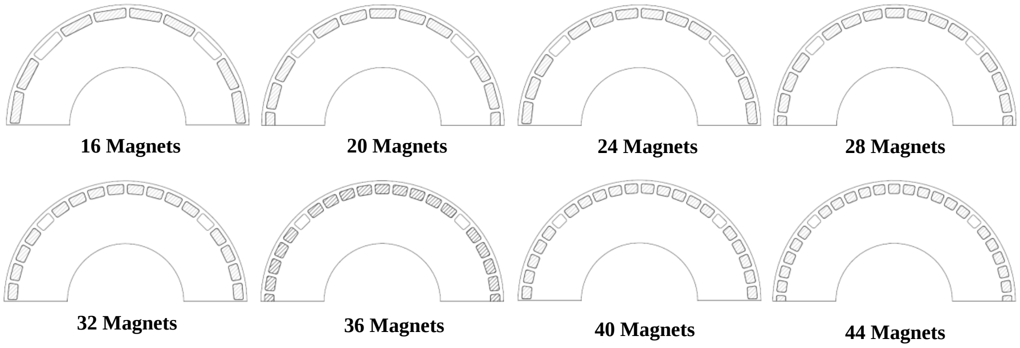

Figure 2.5. Different magnet configurations in the IPM bearingless machine rotor.

The force error angle ϕ_{error}, according to Fig. 2.3, can be mathematically expressed as

$$\phi_{\text{error}} = tan^{-1}\frac{F_{\text{y}}}{F_{\text{x}}}, \tag{2.1}$$

where F_{x} is the radial force in the x-direction and F_{y} is the radial force in the y-direction. The force error angle is analyzed during the maximum constant load on the levitation winding to present the worst-case scenario. The result of the error angle comparison is shown in Fig. 2.6, where the best of four cases are presented. Of these, the 16-magnet rotor structure provides the lowest force error angle. The peak value of the force error angle is 3.03 degrees in this case.

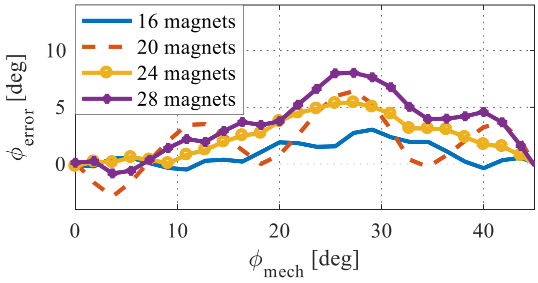

Figure 2.6. Force error angle at the maximum load on the levitation winding.

Based on the rotor geometrical optimization, the 16-magnet configuration was selected to be the rotor structure of the prototype machine. Further analysis was conducted with the selected magnet configuration. The force error angle was then analyzed at the maximum current on the levitation winding and the full load on the torque winding as shown in Fig. 2.7.

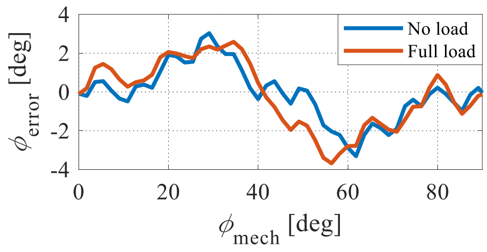

Figure 2.7. Force error angle at the maximum load on the levitation winding with no load and full load on the torque winding.

The error angle curve shows that the effect of full load on the torque winding is minimal. It can be concluded that the loading does not affect the force error angle when this kind of motor structure is used. The linearity of the radial force generation is analyzed in Fig. 2.8 in no-load and full-load situations on the torque winding. The FEM analysis shows that the produced radial force is linear as a function of levitation current. Loading of the bearingless motor will increase the amplitude of the produced radial force. The effect is quite linear and it can be easily taken into account in the control system.

Torque produced by the bearingless motor as a function of current i_{q} is plotted in Fig. 2.9 with different loading currents in the levitation winding. The analysis shows that the loading of the levitation winding does not significantly affect the torque generation. The radial force ripple as a function of rotor angle is depicted in Fig. 2.10a and in 2.10b, where the motor is fully loaded. It can be seen that the levitation force without loading is approximately linear up to 120 N. By introducing the full motor load, the force ripple level is increased. It can be concluded that the produced radial force is linear.

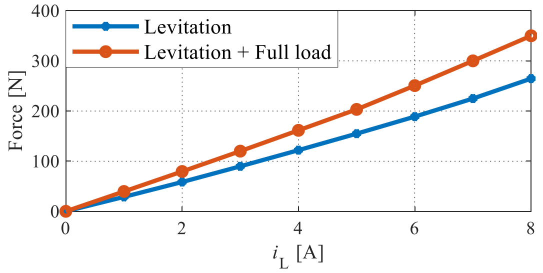

Figure 2.8. Average radial force as a function of current in the no-load and full-load situations.

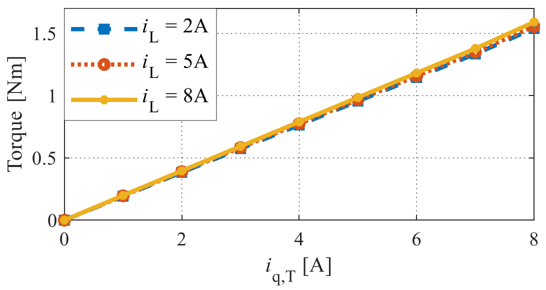

Figure 2.9. Motor torque as a function of $i_{q,T}$ current in different loading conditions in the levitation winding.

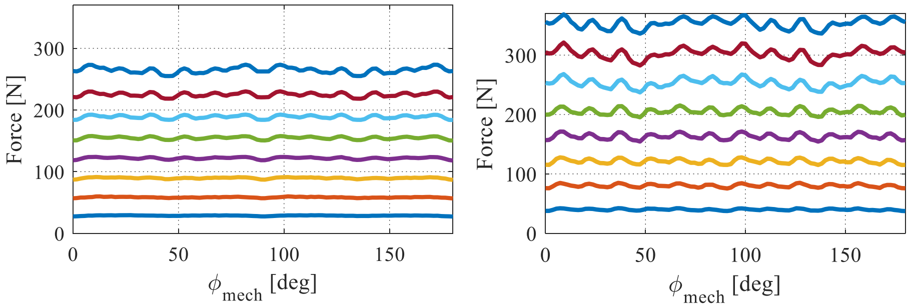

a) b)

Figure 2.10. Radial force as a function of rotor angle. a) Force is produced with a sinusoidal levitation current with a constant rms value from 1 to 8 A. b) Force is produced with a sinusoidal levitation current with a constant rms value from 1 to 8 A at the full motor load.

2.3 Design scalability

In **Publication II**, the scalability of the design presented in **Publication I** was evaluated. The output power was scaled up to tenfold keeping the nominal speed at 30000 r/min. Thus, the total output power of the full machine was 100 kW. The machine parameters can be found in Appendix B. The initial design is based on the analytical approach where the machine parameters are tuned. Fine-tuning of the design was done in the FEM software. An analysis of the radial force generation and the force error angle as a function of different loading conditions is presented in Fig. 2.11. In the full load condition with the maximum levitation current, the peak force error angle reaches 6.7 degrees. To further optimize the motor performance, continuous stator skew was applied. The effect of the 15-degree stator skew is presented in Fig. 2.12. Based on the FEM analysis, it can be concluded that the 15-degree stator skew is an effective method to remove the highest harmonic component from the force waveform.

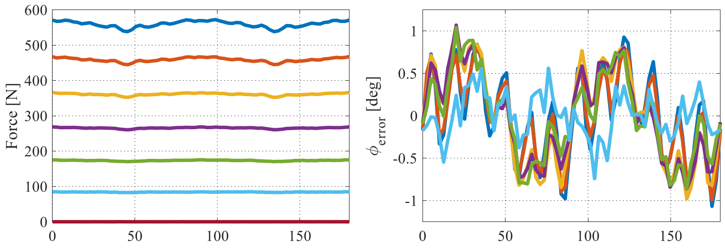

(a) For amplitude at $i_{\mathrm{q,T}}$ = 0 A (b) For error angle at $i_{\mathrm{q,T}}$ = 0 A

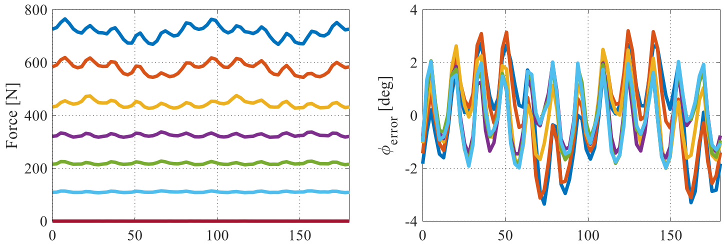

(c) For amplitude at $i_{\mathrm{q,T}}$ = 36 A (d) For error angle at $i_{\mathrm{q,T}}$ = 36 A

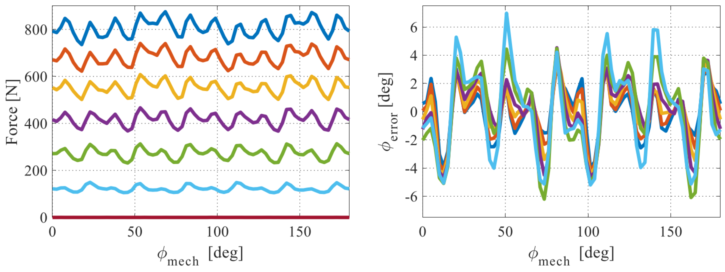

(e) For amplitude at $i_{\mathrm{q,T}}$ = 72 A (e) For error angle at $i_{\mathrm{q,T}}$ = 72 A

Figure 2.11. Radial force amplitude from 0 to 24 A in the levitation winding as a function of different motor load conditions together with the force error angle from each case.

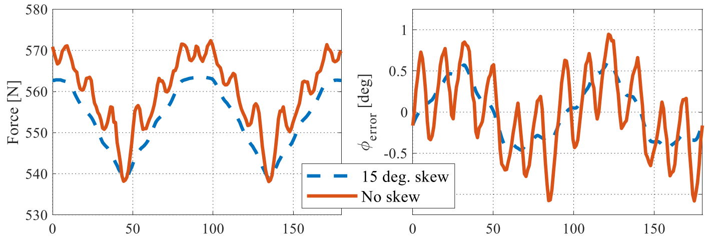

(a) For amplitudes $i_{q,T}$ = 0 A, i_L = 24 A

(b) For amplitudes $i_{q,T}$ = 0 A, i_L = 24 A

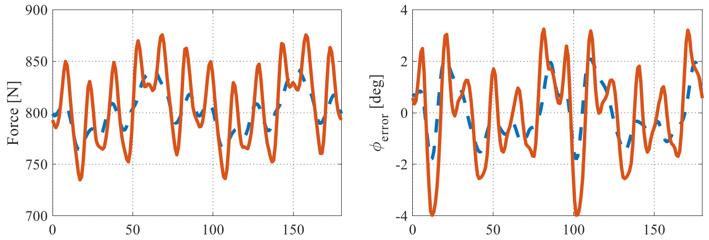

(c) For amplitudes $i_{q,T}$ = 72 A, i_L = 24 A

(d) For amplitudes $i_{q,T}$ = 72 A, i_L = 24 A

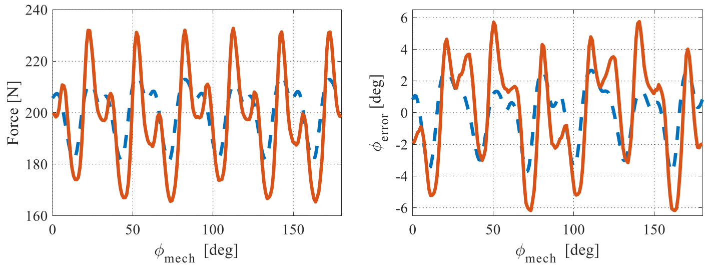

(e) For amplitudes $i_{q,T}$ = 72 A, i_L = 6 A

(e) For amplitudes $i_{q,T}$ = 72 A, i_L = 6 A

Figure 2.12. Radial force amplitude and force error angle with and without the 15-degree stator skew.

The efficiency of the designed bearingless motor presented in **Publication I** is compared with the scaled design in Fig. 2.13. In this comparison, the efficiencies of the one bearingless motor unit is presented based on the FEM simulation. The operating point used in the simulation presents the nominal load and 130% radial force to levitate the rotor. It can be seen that the scaled and more optimized motor design provides an 8 percentage units higher efficiency.

2.4 Stator and rotor structure optimization

In **Publication III**, the rotor and the stator structures were further optimized by applying stator and rotor skew. In the analysis, distributed and tooth-coil winding schemes were compared. With the distributed winding construction, the flux distribution in the air gap is more sinusoidal than with the tooth-coil approach. However, the distributed winding needs space for the long end windings, which leads to a longer rotor structure. The motor cross-sections with the both winding schemes are shown in Fig. 2.14 and Fig. 2.15. In a

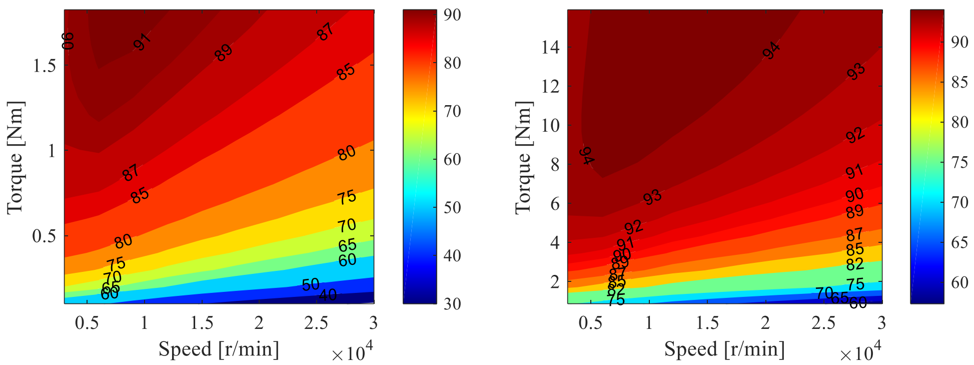

a)

b)

Figure 2.13. Efficiency map based on the FEM simulations. a) 5 kW bearingless motor during nominal load and i_L = 3 A, b) 50 kW motor during nominal load and i_L = 6 A (Jastrzebski et al., 2016).

high-speed application, it is beneficial to have a shorter rotor structure. A shorter rotor is stiffer, and thus, the natural bending frequencies are higher.

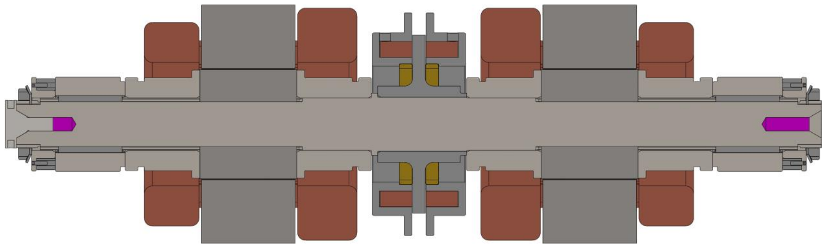

Figure 2.14. Cross-section of the bearingless machine with distributed windings.

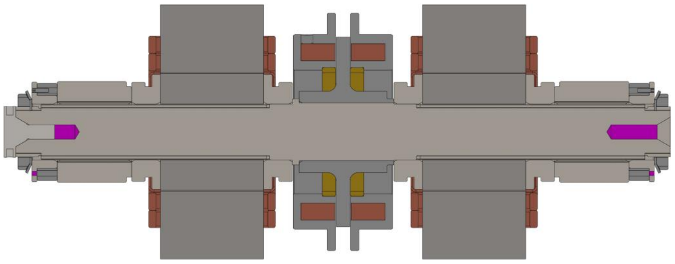

Figure 2.15. Cross-section of the bearingless machine with tooth-coil windings.

Two different skewing methods were compared; continuous skew, which is generally applied to the stator part, and step skew, which is applied to the rotor. Step skew can be applied to the rotor with embedded magnets. Step skew helps in the reduction of the eddy current losses as the magnets are axially segmented by default. The rotor structures with three- and five-step skew are presented in Fig. 2.16.

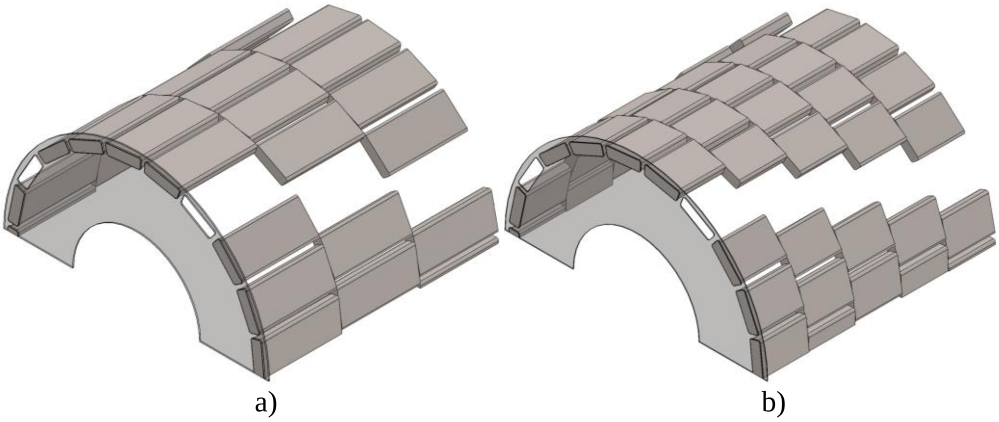

Figure 2.16. Segmented rotor skew with a) three steps and b) five steps.

In Fig. 2.17, a comparison of the skew method with respect to the force error angle is presented. The initial error angle with the tooth-coil winding scheme is 7.1 degrees; this is more than two times as high as in the distributed winding case.

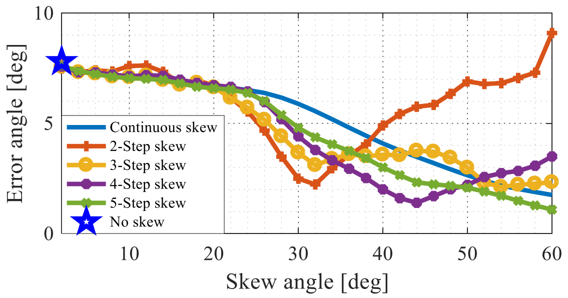

Figure 2.17. Comparison of the effect of different skewing methods on the force error angle.

The analysis results show that the force error angle starts to decrease rapidly after the 20-degree skew angle. The force error angle is under 5 degrees in every analyzed step skew case after 30 degrees of skew angle.

The force ripple from the average force is compared with different skewing methods as a function of skew angle in Fig. 2.18a. The skewing reduces the force ripple but it is not as effective as with the force error angle.

In Fig. 2.18b, the loss of the radial force is analyzed as a function of skew angle. The most effective skewing method when considering the minimization of the loss of radial force is the continuous skew. Based on the results, the most preferable skew angle is 30 degrees. A stator or rotor with this skew angle is feasible to manufacture. The continuous skew was left out from the final selection as the error angle is more than 5 degrees with the selected skew angle. The rest of the skewing methods meet the demand for force error angle. It can be concluded that the step skew is suitable for reducing the force error angle of a tooth-coil-wound bearingless motor.

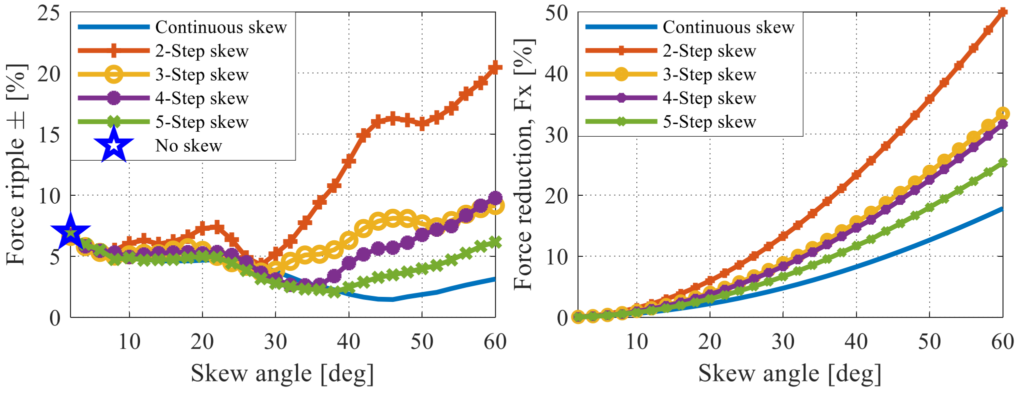

a) b)

Figure 2.18. Comparison of the effect of different skewing methods on a) the radial force ripple and on b) he reduction in the radial force.

2.5 Machine design using the genetic algorithm

In **Publication IV**, the multivariable optimization problem was treated with the genetic algorithm (GA) approach. The initial design was conducted with analytical equations. A differential evolution (DE) algorithm was used to optimize the following design parameters: air-gap length, ratio of equivalent core length, permanent-magnet-induced voltage, tangential stress, peak flux densities in the stator and the rotor, and the slot dimensions. An analytical method, in particular, a reluctance network (RN), is a good approach for the initial bearingless machine design. However, it is time consuming to develop an accurate analytical model that takes all the required parameters accurately into account. Thus, FEM tools are needed to more accurately tune the final parameters and geometrical features of the machine. A FEM-based design approach can also be equipped with an evolution algorithm that automatically evaluates and selects the best design. The proposed design flow is presented in Fig. 2.19.

The accuracy of the FEM-based design was verified by experimental measurements. For this purpose, a special force measurement rig was developed as shown in Fig. 2.20. The measurement system consists of stepper motors, which are used to control the position of

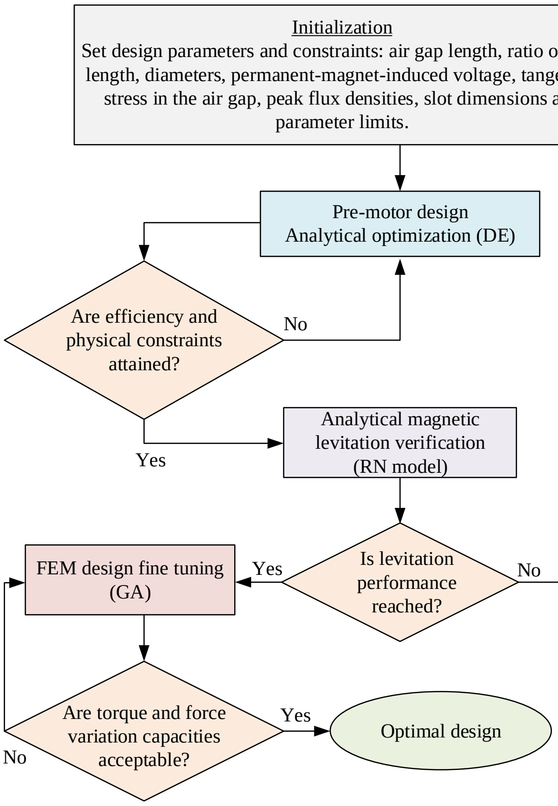
Initialization
Set design parameters and constraints: air gap length, ratio of core length, diameters, permanent-magnet-induced voltage, tangential stress in the air gap, peak flux densities, slot dimensions and parameter limits.
Pre-motor design
Analytical optimization (DE)
Are efficiency and physical constraints attained?
No
Yes
Analytical magnetic levitation verification (RN model)
Is levitation performance reached?
No
Yes
FEM design fine tuning (GA)
Are torque and force variation capacities acceptable?
No
Yes
Optimal design

Figure 2.19. Bearingless machine design flow using the evolution algorithm approach.

the linear track mover. The rotor can be connected to the linear track mover through the force measurement sensor. With this setup, the rotor position can be controlled in the xy plane of the air gap, at the same time measuring the force acting on the rotor in the xyz plane. A detailed description of the force measurement system is presented in Appendix C.

The force error angle of the designed 10 kW bearingless machines was experimentally determined using the presented measurement rig. The measurement results of the force error angle are compared with the FEM simulation in Fig. 2.21a. In the experiment, the force error angle of the both motor units was measured. The experiment was conducted by supplying maximum levitation current in the x-axis direction, and the force error angle was varied by turning the rotor manually in 15-degree steps. The mechanical structure of the force measurement rig caused the rotor to drift from the magnetic center during rotation. For this reason, the magnetic center was traced separately for every angle. This reduced the accuracy of the measurement. However, when comparing the measurement result with the FEM simulation, the corresponding trend is easily seen.
The same measurement platform was used to experimentally determine the current stiffness of the bearingless motor unit and the unbalance magnetic pull. Current stiffness

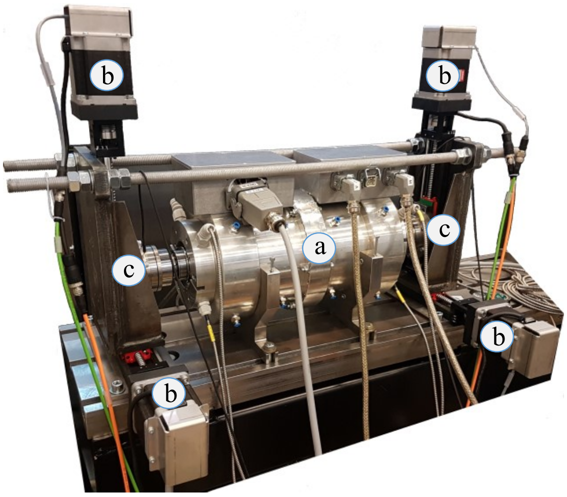

Figure 2.20. Bearingless machine in the force measurement rig. a) Bearingless machine, b) stepper motor, and c) 3-axis force sensor.

was measured by supplying current to the levitation winding and measuring the produced force at the magnetic center. The results of the measurement are shown in Fig. 2.21b and c. The unbalance pull caused by the permanent magnets in the rotor was measured by moving the rotor along the x-axis. Both results correlate closely with the FEM analysis. Based on the measurement, it can be concluded that the FEM analysis produces reliable results.

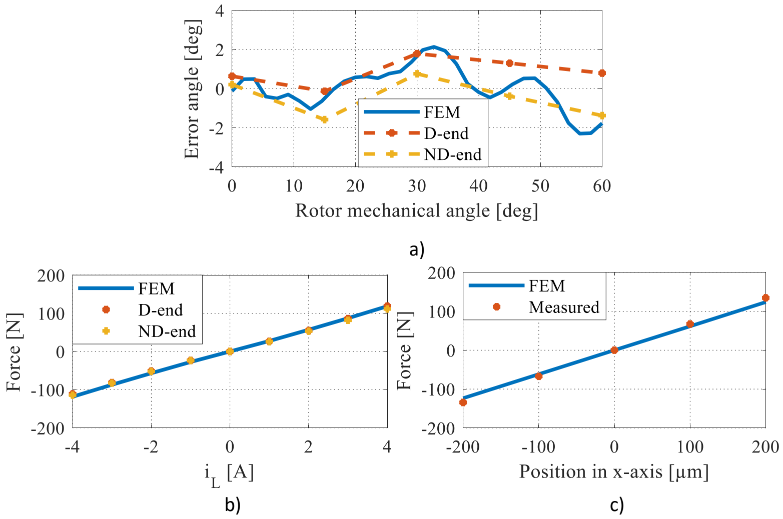

Figure 2.21. a) Measured force error angle compared with the FEM result, b) measured current stiffness and c) measured unbalance magnetic pull compared with the FEM result.

3 System modeling

Linear control approach requires a linear system model where the controller can be synthesized. As the model in the control synthesis is linear, some simplifications are made in the modeling process. A bearingless machine system itself consists of several inputs and outputs as shown in Fig. 3.1. The machine contains five separate winding systems that provide torque for rotation and force to levitate the rotor in the radial and axial directions. The bearingless machine can be placed into the category of multiport electrical machines (Cheng et al., 2018). It is natural to use a state-space modeling approach to present the dynamical equation of the MIMO system. The model of the bearingless machine is only one part of the whole system model; the rotor dynamics model provides crucial information about the cross-coupling of the rotor and the stator parts together with the rotor flexible modes. For the simulation purposes, a variable frequency drive model with pulse width modulation is needed.

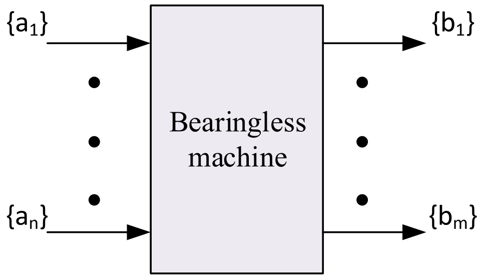

Figure 3.1. Bearingless machine system comprising several inputs (a_n) and outputs (b_m). Depending on the machine configuration, the input ports can consist of current and/or voltage terminals. The outputs are controlled quantities such as rotor position and rotor speed and torque.

3.1 General modeling guidelines

The system dynamics can be presented by adopting a state-space approach. The differential equations of the system under study in the continuous time domain can be formed as

$$\begin{aligned}\dot{\mathbf{x}}(t) &= \mathbf{A}\mathbf{x}(t) + \mathbf{B}\mathbf{u}(t)\\ \mathbf{y}(t) &= \mathbf{C}\mathbf{x}(t) + \mathbf{D}\mathbf{u}(t),\end{aligned} \tag{3.1}$$

where $\mathbf{A}$ is the system matrix, $\mathbf{B}$ is the input matrix, $\mathbf{C}$ is the system matrix, $\mathbf{D}$ is the feedforward matrix, $\mathbf{x}$ is the state vector, $\mathbf{u}$ is the input vector, and $\mathbf{y}$ is the output vector. Often, the feedforward matrix is equal to zero and can thus be neglected.

3.2 Motor model

The mathematical model of the motor winding in the dq rotor reference frame is described by

$$\begin{aligned} u_{\mathrm{d,T}} &= R_{\mathrm{T}} i_{\mathrm{d,T}} + \frac{d}{dt}(L_{\mathrm{d,T}} i_{\mathrm{d,T}}) - \omega L_{\mathrm{q,T}} i_{\mathrm{q,T}}, \\ u_{\mathrm{q,T}} &= R_{\mathrm{T}} i_{\mathrm{q,T}} + \frac{d}{dt}(L_{\mathrm{q,T}} i_{\mathrm{q,T}}) + \omega L_{\mathrm{d,T}} i_{\mathrm{d,T}}, \end{aligned} \tag{3.2}$$

where u_{T} is the voltage in the motor windings, R_{T} is the resistance of the motor windings, L_{T} is the inductance of the motor windings, ω is the electrical angle of the rotor, and i_{T} is the current in the motor windings. The subscript T denotes the torque-generating part.

The motor flux linkages are described by

$$\begin{aligned} \psi_{\mathrm{d,T}} &= L_{\mathrm{d,T}} i_{d,T} + \psi_{\mathrm{PM}}, \\ \psi_{\mathrm{q,T}} &= L_{\mathrm{q,T}} i_{\mathrm{q,T}}. \end{aligned} \tag{3.3}$$

The produced electrical torque can be expressed as

$$t_{\mathrm{e}} = \frac{3}{2} p[\psi_{\mathrm{PM}} i_{\mathrm{q,T}} + (L_{\mathrm{d,T}} - L_{\mathrm{q,T}}) i_{\mathrm{q,T}} i_{\mathrm{d,T}}], \tag{3.4}$$

where p is the number of the pole pairs and ψ_{PM} is flux linkage produce by the permanent magnets. The torque equation can be simplified by employing the $i_{\mathrm{d}} = 0$ control principle, which gives

$$t_{\mathrm{e}} = \frac{3}{2} p(\psi_{\mathrm{PM}} i_{\mathrm{q,T}}) = k_{\mathrm{T}} i_{\mathrm{q,T}}, \tag{3.5}$$

where k_{T} is the torque constant.

3.3 Force model

In order to form a model-based controller for a magnetic levitation system, a linear force model is needed. The model describes how the levitation system behaves as a function of air gap and control current. The nonlinear parameters of position and current stiffness are linearized around the operating point.

3.3.1 One-degree-of-freedom AMB

An axial AMB is considered in modeling of the 1-DOF magnetic levitation system. The magnetic force produced in the electromagnet can be calculated based on the energy stored in the air gap (Schweitzer and Maslen, 2009)

$$f = \frac{1}{4}\mu_0 n^2 A_{\mathrm{a}} \frac{i^2}{s^2}, \tag{3.6}$$

where μ_0 is the magnetic constant, n is the number of coil turns, A_{a} is the surface area of the AMB pole, i is the coil current, and s is the air-gap distance. The nonlinear behavior of the produced magnetic force is seen in (3.6) as the force amplitude is quadratically proportional to the current and inverse-quadratically proportional to the air gap. Opposite electromagnets are needed to control the rotor position in the air gap as only subtracting force is produced by one electromagnet. The nonlinear function of the produced magnetic force must be linearized for the control synthesis purposes. A constant bias current is added to the electromagnets to linearize the current for force correlation around the operating point. The resultant force of two opposite magnetic poles is given by

$$f_{\mathrm{z}} = f_{+} - f_{-} = \frac{1}{4}\mu_0 n^2 A_{\mathrm{a}} \left[\frac{(i_{\mathrm{b}} + i_{\mathrm{z}})^2}{(s_0 - z_{\mathrm{dis}})^2} - \frac{(i_b - i_{\mathrm{z}})^2}{(s_0 + z_{\mathrm{dis}})^2} \right], \tag{3.7}$$

where i_{b} is the bias current, i_{z} is the control current, s_0 is the nominal air gap, and z_{dis} is the air-gap displacement.

By assuming the movement of the ferromagnetic object small with respect to the air-gap distance, that is, $z_{\mathrm{dis}} \ll s_0$, the nonlinear force function (3.12) can be linearized as

$$f_{\mathrm{z}} = \frac{\mu_0 n^2 A_a i_{\mathrm{b}}}{s_0^2} i_z + \frac{\mu_0 n^2 A_a i_{\mathrm{b}}^2}{s_0^3} z_{\mathrm{dis}} = k_{\mathrm{i}} i_{\mathrm{z}} + k_{\mathrm{x}} z_{\mathrm{dis}}, \tag{3.8}$$

where k_{i} is the current stiffness, and k_{x} is the position stiffness. The linearized force model can now be used in the control synthesis.

3.3.2 Bearingless motor

A general version of the bearingless motor consists of separate winding sets that are responsible for producing levitation force and rotating torque. The modeling principles are presented in (Chiba et al., 2005), where the flux linkage model is derived for the both winding sets as

$$\begin{bmatrix}\psi_{\mathrm{d,T}}\\ \psi_{\mathrm{q,T}}\\ \psi_{\mathrm{d,L}}\\ \psi_{\mathrm{q,L}}\end{bmatrix} = \begin{bmatrix} L_{\mathrm{d,T}} & 0 & M'_{\mathrm{d}}x_{\mathrm{r}} & -M'_{\mathrm{d}}y_{\mathrm{r}}\\ 0 & L_{\mathrm{q,T}} & M'_{\mathrm{q}}y_{\mathrm{r}} & M'_{\mathrm{q}}x_{\mathrm{r}}\\ M'_{\mathrm{d}}x_{\mathrm{r}} & M'_{\mathrm{q}}y_{\mathrm{r}} & L_{\mathrm{d,L}} & 0\\ -M'_{\mathrm{d}}y_{\mathrm{r}} & M'_{\mathrm{q}}x_{\mathrm{r}} & 0 & L_{\mathrm{q,L}}\end{bmatrix} \begin{bmatrix}i_{\mathrm{d,T}}\\ i_{\mathrm{q,T}}\\ i_{\mathrm{d,L}}\\ i_{\mathrm{q,L}}\end{bmatrix} + \begin{bmatrix}\psi_{\mathrm{PM}}\\ 0\\ \psi'_{\mathrm{PM}}x_{\mathrm{d}}\\ -\psi'_{\mathrm{PM}}y_{\mathrm{q}}\end{bmatrix}, \tag{3.9}$$

where $\psi_{\mathrm{d,T}}$ and $\psi_{\mathrm{q,T}}$ are the flux linkages produced by the torque winding in the rotor reference frame, $\psi_{\mathrm{d,L}}$ and $\psi_{\mathrm{q,L}}$ are the flux linkages produced by the levitation winding in the rotor reference frame, $L_{\mathrm{d,T}}$ and $L_{\mathrm{q,T}}$ are the self-inductances of the torque winding, $L_{\mathrm{d,L}}$ and $L_{\mathrm{q,L}}$ are the self-inductances of the levitation winding, M'_{d} and M'_{q} are the mutual inductance slopes with respect to the corresponding rotor displacement, x_{r} and y_{r} are the rotor displacement in the rotor reference frame, $i_{\mathrm{d,T}}$ and $i_{\mathrm{q,T}}$ are the torque winding currents in the rotor reference frame, $i_{\mathrm{d,L}}$ and $i_{\mathrm{q,L}}$ are the levitation winding currents in the rotor reference frame, ψ_{PM} is the flux linkage produced by the permanent magnets, and ψ'_{PM} is the flux linkage produced by the permanent magnet with respect to the corresponding rotor displacement. From the flux linkage model, the force model can be derived by partial differentiation of the magnetic energy equation with respect to the rotor displacement. Subsequently, the force model is formed as

$$\begin{bmatrix}f_{\mathrm{x,r}}\\ f_{\mathrm{y,r}}\end{bmatrix} = \begin{bmatrix}\psi'_{\mathrm{PM}} + M'_{\mathrm{d}}i_{\mathrm{d,T}} & M'_{\mathrm{q}}i_{\mathrm{q,T}}\\ M'_{\mathrm{q}}i_{\mathrm{q,T}} & -\psi'_{\mathrm{PM}} - M'_{\mathrm{d}}i_{\mathrm{d,T}},\end{bmatrix} \begin{bmatrix}i_{\mathrm{d,L}}\\ i_{\mathrm{q,L}}\end{bmatrix}, \tag{3.10}$$

where $f_{\mathrm{x,r}}, f_{\mathrm{y,r}}$ are the generated radial forces in the rotor reference frame. The model presented in (3.10) can be further reduced assuming that the $i_{\mathrm{d}} = 0$ control principle is used for the torque control, and the disturbance force produced by $M'\mathrm{q}i_{\mathrm{q,T}}$ is small with respect to ψ'_{PM}

$$\begin{bmatrix}f_{\mathrm{x,r}}\\ f_{\mathrm{y,r}}\end{bmatrix} = \begin{bmatrix}\psi'_{\mathrm{PM}} & 0\\ 0 & -\psi'_{\mathrm{PM}}\end{bmatrix} \begin{bmatrix}i_{\mathrm{d,L}}\\ i_{\mathrm{q,L}}\end{bmatrix}. \tag{3.11}$$

When the simplified force model is used as presented, the analogy to the AMB force model (3.8) can be applied

$$\mathbf{F}_{\mathrm{r}} = \mathbf{K}_{\mathrm{x}}\mathbf{q}_{\mathrm{r}} + \mathbf{K}_{\mathrm{i}}\mathbf{i}_{\mathrm{d,q}}, \tag{3.12}$$

where $\mathbf{F}_{\mathrm{r}}$ is the force vector in the rotor reference frame, $\mathbf{K}_{\mathrm{x}}$ is the position stiffness matrix, $\mathbf{q}_{\mathrm{r}}$ is the position vector in the rotor reference frame, and $\mathbf{K}_{\mathrm{i}}$ is the current stiffness matrix. The position and current stiffness values can be determined by FEM simulations, which are verified by experimental identification.

3.4 Rotor model

The rotor model describes the mechanical behavior of the system, the force model being the system input. Basic modeling of the 1-DOF AMB system is presented together with the 4-DOF model that is based on the rigid rotor method. The presented modeling approach is used for the control synthesis in **Publication V**, **Publication VI**, and **Publication VII**.

3.4.1 Point-mass model

The force equation of the 1-DOF magnetic levitation system is based on Newton's second law of motion. A ferromagnetic object that is levitated with a magnetic field is modeled as a point mass

$$m\ddot{q} = k_{\mathrm{x}}q + k_{\mathrm{i}}i_{\mathrm{c}}, \tag{3.13}$$

where m is the mass of the levitated object, k_{x} is the position stiffness, k_{i} is the current stiffness, q is the levitated object position in the air gap, and i_{c} is the control current. This SISO model is used for the control design of the axial magnetic bearing.

3.4.2 Rigid rotor model

The equation of motion for the linear axially symmetric rotor with the following equation (Genta, 2005) is described by

$$\mathbf{M}\ddot{\mathbf{q}}(t) + (\mathbf{D}_{\mathrm{r}} + \Omega\mathbf{G}_{\mathrm{r}})\dot{\mathbf{q}}(t) + \mathbf{K}\mathbf{q}(t) = \mathbf{F}(t), \tag{3.14}$$

where $\mathbf{M}$ is the mass matrix, $\mathbf{D}_{\mathrm{r}}$ is the damping matrix, Ω is the rotor speed, $\mathbf{G}_{\mathrm{r}}$ is the gyroscopic matrix, $\mathbf{K}$ is the stiffness matrix, $\mathbf{F}$ is the input force vector, and $\mathbf{q}$ is the position vector in the center of mass coordinates. By assuming rigid behavior of the rotor, the model can be simplified into the following form

$$\mathbf{M}\ddot{\mathbf{q}}(t) + (\Omega\mathbf{G}_{\mathrm{r}})\dot{\mathbf{q}}(t) = \mathbf{F}(t). \tag{3.15}$$

The mass and the gyroscopic matrices are arranged in the following form

$$\mathbf{M} = \begin{pmatrix} I_{\mathrm{y}} & 0 & 0 & 0 \\ 0 & m & 0 & 0 \\ 0 & 0 & I_{\mathrm{x}} & 0 \\ 0 & 0 & 0 & m \end{pmatrix}, \quad \mathbf{G} = \begin{pmatrix} 0 & 0 & I_{\mathrm{z}} & 0 \\ 0 & 0 & 0 & 0 \\ -I_{\mathrm{z}} & 0 & 0 & 0 \\ 0 & 0 & 0 & 0 \end{pmatrix}, \tag{3.16}$$

where I_{x} is the rotor inertia with respect to the x-axis, I_y is the rotor inertia with respect to the y-axis, I_{y} is the rotor inertia with respect to the y-axis, and m is the rotor weight.

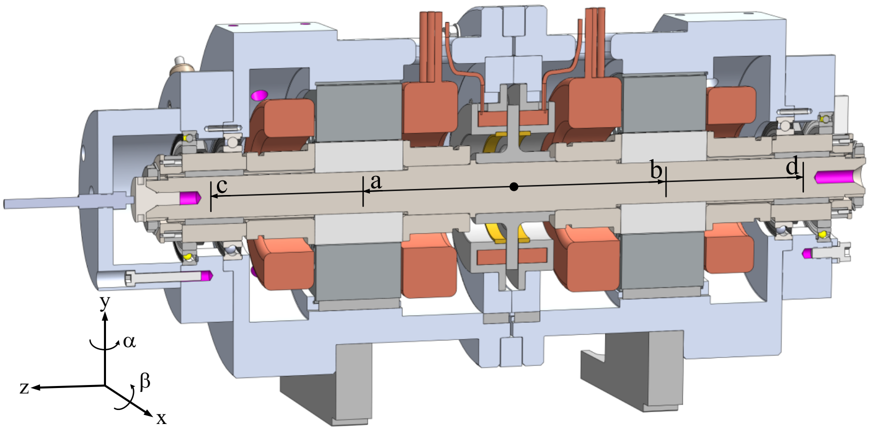

Figure 3.2. Cross-sectional view of the bearingless machine. The distances from the center of mass to the motor and the sensor locations are presented.

The rotor model is presented in the center of mass coordinates, where the position vector is $\mathbf{q} = \begin{bmatrix}\beta & x & \alpha & y\end{bmatrix}^T$. The bearingless motor units and the rotor measurement planes are in different locations compared with the center of mass, as seen in Fig. 3.2. Therefore, coordinate transformations must be carried out to correctly represent the system. Transformation of the coordinate system can be made with the subsequent matrices

$$\mathbf{T}_{\mathrm{bc}} = \begin{pmatrix} a & 0 & -b & 0 \\ 1 & 0 & 1 & 0 \\ 0 & a & 0 & -b \\ 0 & 1 & 0 & 1 \end{pmatrix}, \quad \mathbf{T}_{\mathrm{cs}} = \begin{pmatrix} c & 1 & 0 & 0 \\ 0 & 0 & c & 1 \\ -d & 1 & 0 & 0 \\ 0 & 0 & -d & 1 \end{pmatrix}, \tag{3.17}$$

where $\mathbf{T}_{\mathrm{bc}}$ is the transformation from the bearing coordinates to the center of mass coordinates, $\mathbf{T}_{\mathrm{cs}}$ is the transformation from the center of mass coordinates to the sensor coordinates, a, b are the locations of the bearingless motors from the center of mass, and c, d are the position sensor locations from the center of mass.

$$\mathbf{F}(t) = \mathbf{T}_{\mathrm{bc}}\mathbf{K}_x\mathbf{T}_{\mathrm{bc}}^{\mathrm{T}}\mathbf{q}_{\mathrm{b}} + \mathbf{T}_{\mathrm{bc}}\mathbf{K}_{\mathrm{i}}\mathbf{i}_{\mathrm{c}}, \tag{3.18}$$

where $\mathbf{F}$ is the radial force vector, $\mathbf{K}_{\mathrm{x}}$ is the diagonal position stiffness matrix, $\mathbf{K}_{\mathrm{i}}$ is the diagonal current stiffness matrix, $\mathbf{q}_{\mathrm{b}}$ is the radial position vector in the bearing coordinates, and $\mathbf{i}_{\mathrm{c}}$ is the control current vector. Thus, the coordinate transformation must be performed to the rotor model to match the coordinate system between the inputs and the outputs.

$$\mathbf{M}\ddot{\mathbf{q}}(t) = \mathbf{T}_{\mathrm{bc}}\mathbf{K}_x\mathbf{T}_{\mathrm{bc}}^{\mathrm{T}}\mathbf{q}_{\mathrm{b}} + \mathbf{T}_{\mathrm{bc}}\mathbf{K}_{\mathrm{i}}\mathbf{i}_{\mathrm{c}}, \tag{3.19}$$

By arranging the rigid rotor model in the state-space presentation, the equation takes the following form

$$\begin{aligned}
\mathbf{A}_{\mathrm{r}} &= \begin{bmatrix} \mathbf{0} & \mathbf{I} \\ (\mathbf{M})^{-1}\mathbf{T}_{\mathrm{bc}}\mathbf{K}_{\mathrm{x}}\mathbf{T}_{\mathrm{bc}}^{\mathrm{T}} & \mathbf{0} \end{bmatrix}, \\
\mathbf{B}_{\mathrm{r}} &= \begin{bmatrix} \mathbf{0} \\ (\mathbf{M})^{-1}\mathbf{T}_{\mathrm{bc}}\mathbf{K}_{\mathrm{i}} \end{bmatrix}, \\
\mathbf{C}_{\mathrm{r}} &= \begin{bmatrix} \mathbf{T}_{\mathrm{cs}} & \mathbf{0} \end{bmatrix}, \\
\mathrm{q}_{\mathrm{b}} &= \begin{bmatrix} \mathrm{q}_{\text{D-end,x}} & \mathrm{q}_{\text{D-end,y}} & \mathrm{q}_{\text{ND-end,x}} & \mathrm{q}_{\text{ND-end,y}} \end{bmatrix}^{\mathrm{T}}, \\
\mathbf{i}_{\mathrm{c}} &= \begin{bmatrix} \mathrm{i}_{\text{D-end,x}} & \mathrm{i}_{\text{D-end,y}} & \mathrm{i}_{\text{ND-end,x}} & \mathrm{i}_{\text{ND-end,y}} \end{bmatrix}^{\mathrm{T}}.
\end{aligned} \tag{3.20}$$

For control synthesis, the time-continuous system model has to be discretized with the sampling time of the control system

$$\begin{aligned}
\mathbf{x}(k+1) &= \mathbf{\Phi}\mathbf{x}(k) + \mathbf{\Gamma}\mathbf{u}(k) \\
\mathbf{y}(k) &= \mathbf{C}\mathbf{x}(k),
\end{aligned} \tag{3.21}$$

where $\mathbf{\Phi}$ is the discrete system matrix, and $\mathbf{\Gamma}$ is the discrete input matrix.

3.5 Actuator model

The actuator model describes the dynamics of the inner control loop, which includes the current control loop and the winding system. A direct method to model the actuator dynamics is to use first-order dynamics (Webster and Eren, 2014). The actuator can then be modeled as a delay in the system. The bandwidth of the current control loop can be used to describe the first-order system dynamics as

$$G_{\mathrm{a}} = \frac{\omega_{\mathrm{cc}}}{s + \omega_{\mathrm{cc}}}, \tag{3.22}$$

where G_{a} is the approximate transfer function of the inner current loop, and ω_{cc} is the bandwidth of the current controller. The actuator dynamics can be left out from the full model if the bandwidth is significantly higher than in the position control loop (Smirnov, 2012).

In the simulations presented in **Publication V**, **Publication VI**, and **Publication VII**, the actuator model is fully implemented including the inner current control loop together with the full bearingless machine model. The VFD is modeled using the two-stage switching with a pulse width modulator.

4 Control

A common factor in publications on the control of bearingless machines is the approach of PID-based rotor position regulation (Sun et al., 2016b; Wang et al., 2015; Sun et al., 2016a; Ooshima et al., 2015; Yang et al., 2010; Huang et al., 2014). A PID controller is a good solution for systems that have simple dynamics and are of a SISO type. In the case of a magnetic levitation system where several magnetic levitation units are used, the system is of a MIMO type. This generates cross-coupling between the levitation units, in other words, the rotor movement affects all units. When adopting a PID-based approach, the cross-coupling can be taken into account by adding gains between the levitation units. This, however, makes the design process more complex. By using a model-based control approach, the inherent cross-coupling of the magnetic levitation system can be taken into account. However, the mathematical model is essential for the control synthesis and analysis, and a linearized version can be used to design the MIMO model-based controller. In the bearingless machine, the control is divided into levitation and torque control. Further, a traditional AMB is used to control the rotor axial position. As the axial AMB is a SISO system, the PID controller usually suffices to achieve the control performance.

The performance of a magnetic levitating system can be determined by analyzing the system stability. In the standard (ISO 1940-1:2003(E), 2003), a sensitivity analysis method and acceptable limits for controller performance are presented. The analysis is based on the output sensitivity of the control system, which determines how sensitive the system is to output disturbances. Based on the ISO standard, the peak output sensitivity should, in the best scenario, be under 9.5 dB. At a more general level, the performance of a magnetic levitation system is analyzed by inspecting the rotor vibration. Acceptable vibration levels for the magnetic levitation systems are described in the standard (ISO 14839-3:2004(E), 2004). The vibration levels are divided into four zones depicted in Fig. 4.1.

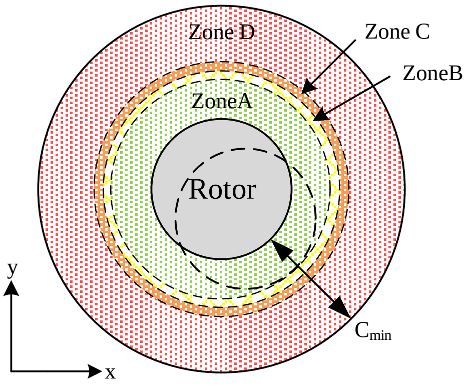

Figure 4.1. Rotor vibration zones described in the standard (ISO 14839-3:2004(E), 2004). Zone A is the acceptable area where the rotor can vibrate continuously. A description of the vibration zones is given in Appendix D. Value of the C_{min} determines the rotor minimum clearance that is generally restricted by backup bearings.

4.1 Overview of the control system

The bearingless machine under investigation consists of two bearingless motor units that are responsible for generating the rotating torque and the levitation force in the radial direction. In addition, an axial AMB is positioned in the center of the rotor to produce the stabilizing magnetic force along the shaft. In Fig. 4.2, the variable frequency drive (VFD) setup is presented. Each of the three phase windings is driven with a separate VFD. This configuration allows to use one bearingless unit as a load machine to the other unit. The axial AMB consists of two opposite coils that are driven with a VFD connected between the phases. Each VFD state is controlled with a field programmable gate array (FPGA), where the modulator and the inner current controller are implemented. The inner current control loop is illustrated in Fig. 4.3. The upper-level control loops, as shown in Fig. 4.4, are implemented in an industrial PC. Separate control loops for the axial and radial positions of the rotor are formed together with the motor speed controller. The sampling time in the industrial PC is 50 μs.

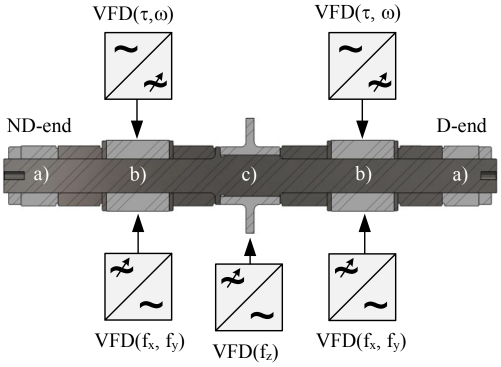

Figure 4.2. Block diagram of the bearingless machine VFD configuration; a) position sensor measurement surface, b) lamination stack of the IPM bearingless motor, and c) axial disc of the AMB.

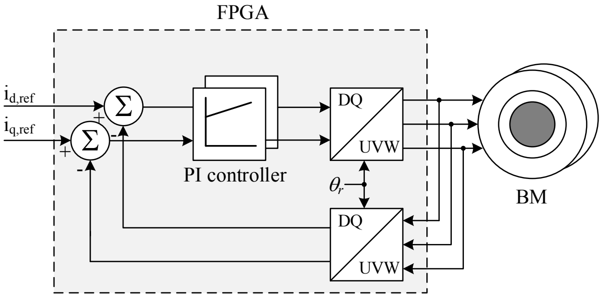

Figure 4.3. Inner current control loop implemented in the FPGA, where θ_r is the rotor electrical angle.

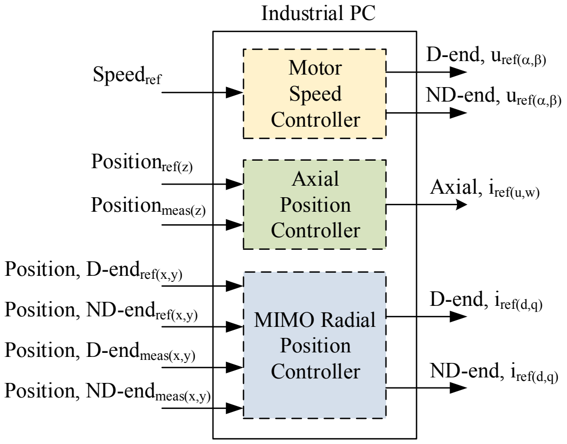
Industrial PC
Speed$_{\text{ref}}$
Motor Speed Controller
D-end, $u_{\text{ref}(\alpha,\beta)}$
ND-end, $u_{\text{ref}(\alpha,\beta)}$
Position$_{\text{ref}(z)}$
Position$_{\text{meas}(z)}$
Axial Position Controller
Axial, $i_{\text{ref}(u,w)}$
Position, D-end$_{\text{ref}(x,y)}$
Position, ND-end$_{\text{ref}(x,y)}$
Position, D-end$_{\text{meas}(x,y)}$
Position, ND-end$_{\text{meas}(x,y)}$
MIMO Radial Position Controller
D-end, $i_{\text{ref}(d,q)}$
ND-end, $i_{\text{ref}(d,q)}$

Figure 4.4. Block diagram of the control loops implemented in the industrial PC together with the inputs and the outputs.

4.2 Levitation control

Magnetic levitation systems are inherently unstable, and therefore, active control is required to stabilize the system. A PID-based control approach is presented for the axial AMB. The same control methods can be extended to the noncollocated position control of radial AMBs. For the radial position control, a MIMO state-feedback approach is presented. Various control approaches are introduced for the control synthesis, including pole placement, linear quadratic regulator, and robust control methods in **Publications V–VII**.

4.2.1 Axial AMB control

An axial AMB is used to control the rotor position in the longitudinal direction. In the prototype machine, an axial AMB is positioned in the center of the rotor. In Fig. 4.2, a cross-sectional view of the rotor is shown, and in Fig. 3.2, a more detailed presentation of the axial AMB and the axial disc is given. The axial AMB consists of a ferromagnetic rotor disc and a differential winding system placed on opposite sides of the disc. The axial AMB is a SISO system having one degree of freedom. The dynamics of the system is based on the model in (3.13). A PID control approach is used to stabilize the rotor in the axial direction. The control loop of the axial AMB is presented in Fig. 4.5.

Detailed formulation of the PID controller for a point-mass system is given in (Chiba et al., 2005). As the force produced by the opposite electromagnets is nonlinear with respect to the air gap and the supplied current, the system is linearized with a bias current. The biasing takes the following form

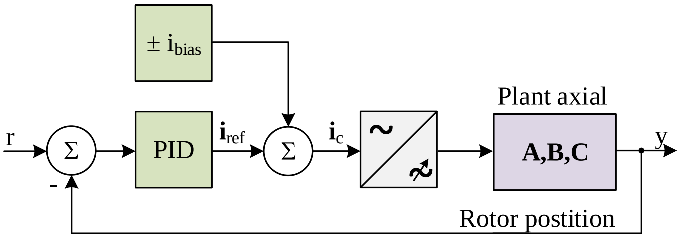

Figure 4.5. Block diagram of the control loop for the PID controller.

$$\mathbf{i}_{\text{ref}} = \begin{bmatrix} i_{\text{c}} + i_{\text{bias}} & i_{\text{c}} - i_{\text{bias}} \end{bmatrix}, \tag{4.1}$$

where the bias current i_{bias} is added to and subtracted from the reference current i_{ref} provided by the PID controller to linearize the force produced by the electromagnets around the operating point.

4.2.2 Radial position control with pole placement

A classical way to synthesize a controller for a system that is modeled with the state-space approach is the full state feedback method (Franklin et al., 2010). The state feedback is based on the knowledge of the system states, and with the feedback gain, the pole locations can be selected. In many systems, all the state variables cannot be measured directly. For this reason, a state estimator or an observer must be included in the control synthesis. Unmeasured states can then be estimated by the state estimator using the input and output signals of the system. A block diagram of the state-feedback control reported in **Publication V** is depicted in Fig. 4.6. Furthermore, this control approach includes an integral action. The integral states are augmented to the system model to remove steady-state errors in the system. Obviously, the gravity force is the main source of the steady-state error.

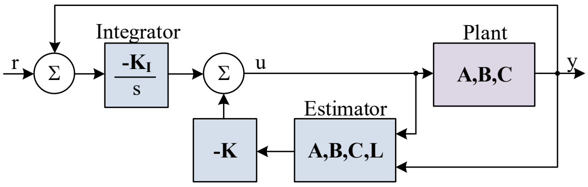

Figure 4.6. Block diagram of the state feedback controller with an integral action.

A discretized system model with the augmented integral states can be presented as

$$\begin{bmatrix}\mathbf{x}(k+1)\\ \mathbf{x}_{\mathrm{I}}(k+1)\end{bmatrix} = \begin{bmatrix}\mathbf{\Phi} & \mathbf{0}\\ \mathbf{C} & \mathbf{I}\end{bmatrix}\begin{bmatrix}\mathbf{x}(k)\\ \mathbf{x}_{\mathrm{I}}(k)\end{bmatrix} + \begin{bmatrix}\mathbf{\Gamma}\\ \mathbf{0}\end{bmatrix}\mathbf{u}(k) - \begin{bmatrix}\mathbf{0}\\ \mathbf{I}\end{bmatrix}\mathbf{r}(k), \tag{4.2}$$

where $\mathbf{x}$ is the state vector, $\mathbf{x}_{\mathrm{I}}$ is the augmented integral state vector, $\mathbf{\Phi}$ is the discrete state matrix, $\mathbf{C}$ is the output matrix, $\mathbf{I}$ is the identity matrix, $\mathbf{\Gamma}$ is the discrete input matrix, $\mathbf{u}$ is the input vector, and $\mathbf{r}$ is the reference vector.

The feedback loop is closed by feeding the states through the negative feedback gains back to the input, which gives the feedback control

$$\mathbf{u}(k) = -\begin{bmatrix}\mathbf{K} & \mathbf{K}_{\mathrm{I}}\end{bmatrix}\begin{bmatrix}\mathbf{x}(k)\\ \mathbf{x}_{\mathrm{I}}(k)\end{bmatrix}, \tag{4.3}$$

where $\mathbf{K}$ is the feedback gain matrix, and $\mathbf{K}_{\mathrm{I}}$ is the integral gain matrix. As mentioned above, all the states cannot be measured, and therefore, a state estimator must be included. The state estimator minimizes the error between the measured and the estimated outputs. By adjusting the feedback gains of the state estimator, the convergence speed can be adjusted. The discrete state estimator takes the following form

$$\hat{\mathbf{x}}(k+1) = \mathbf{\Phi}\hat{\mathbf{x}}(k) + \mathbf{\Gamma}\mathbf{u}(k) + \mathbf{L}(\mathbf{y}(k) - \mathbf{C}\hat{\mathbf{x}}(k)), \tag{4.4}$$

where $\hat{\mathbf{x}}$ is the estimated state vector, and $\mathbf{L}$ is the estimator state feedback gain matrix.

4.2.3 Radial position control with the LQR method

More sophisticated control methods have been developed to overcome the drawbacks of the full state feedback control. An example of these methods is the linear quadratic regulator (LQR) control (Franklin et al., 2010). This approach belongs to the optimal control methods. The method is based on the minimization of the cost function, where the designer can put weight on certain states and inputs. This provides an opportunity to directly manipulate the system response and the control effort. The cost function is presented in the following form

$$\mathcal{J} = \frac{1}{2}\sum_{k=0}^{N}[\mathbf{x}^{\mathrm{T}}(k)\mathbf{Q}_1\mathbf{x}(k) + \mathbf{u}^{\mathrm{T}}\mathbf{Q}_2\mathbf{u}(k)], \tag{4.5}$$

where $\mathbf{x}$ is the state vector, $\mathbf{Q}_1$ is the state weight matrix, $\mathbf{u}$ is the input vector, and $\mathbf{Q}_2$ is the input weight matrix.

In **Publication V**, the general LQR problem is extended with Bryson's rule (Bryson and Ho, 1975). With this method, the most relevant states are weighted as

$$\mathbf{Q}_1 = \mathbf{C}^{\mathrm{T}}\bar{\mathbf{Q}}_1\mathbf{C}, \tag{4.6}$$

where $\mathbf{C}$ is the output matrix, and $\bar{\mathbf{Q}}_1$ is the weighting matrix. This implies that the states of the rotor position are weighted. The state weighting matrix is determined as

$$\bar{\mathbf{Q}}_{1,\mathrm{n}} = \begin{pmatrix} 1/m_1^2 & 0 & \cdots & 0 \\ 0 & 1/m_2^2 & \cdots & 0 \\ \vdots & \vdots & \ddots & \vdots \\ 0 & 0 & \cdots & 1/m_{\mathrm{n}}^2, \end{pmatrix}, \tag{4.7}$$

where m_{n} is the maximum deviation of the rotor position, that is, vibration and the subscript n is the total number of inputs or outputs. The input weighting matrix is determined as

$$\mathbf{Q}_{2,\mathrm{n}} = \begin{pmatrix} 1/u_{1\mathrm{max}}^2 & 0 & \cdots & 0 \\ 0 & 1/u_{2\mathrm{max}}^2 & \cdots & 0 \\ \vdots & \vdots & \ddots & \vdots \\ 0 & 0 & \cdots & 1/u_{\mathrm{nmax}}^2 \end{pmatrix}, \tag{4.8}$$

where u_{nmax} is the maximum deviation of the input current. By applying Bryson's rule in the control synthesis, the tuning process can be simplified as there are only input and output weights to select, which are bound to real parameters. Iterative tuning process is presented in **Publications V**.

4.2.4 Disturbance estimator

An extension to the state estimator is to add a known disturbance model to the estimator. The operating principle is then similar to the integral action as the disturbance estimator drives the error to zero. The disturbance that can be presented with the first-order differential equation can be included in the disturbance estimator. In **Publication VI**, a disturbance estimator with the state feedback controller tuned by the LQR approach is addressed. In Fig. 4.7, a block diagram of the LQR controller with a disturbance estimator is presented. Disturbance can be modeled in the continuous time domain as (Franklin et al., 2010)

$$\begin{aligned} \dot{x}_{\mathrm{d}}(t) &= \mathbf{A}_{\mathrm{d}}\mathbf{x}_{\mathrm{d}}(t) \\ w(t) &= \mathbf{C}_{\mathrm{d}}\mathbf{x}_{\mathrm{d}}(t), \end{aligned} \tag{4.9}$$

where $\mathbf{x}_{\mathrm{d}}$ is the disturbance state vector, $\mathbf{A}_{\mathrm{d}}$ is the disturbance system matrix, w is the disturbance output vector, and $\mathbf{C}_{\mathrm{d}}$ is the disturbance output matrix. By discretizing the disturbance model with the sampling time, it takes the form

$$\begin{aligned} x_{\mathrm{d}}(k+1) &= \mathbf{\Phi}_{\mathrm{d}}\mathbf{x}_{\mathrm{d}}(k) \\ w(k) &= \mathbf{C}_{\mathrm{d}}\mathbf{x}_{\mathrm{d}}(k), \end{aligned} \tag{4.10}$$

where $\mathbf{\Phi_d}$ is the discrete system matrix. The disturbance model can be augmented to 3.21 to form a system model where the disturbance estimator can be synthesized

$$\begin{aligned} \begin{bmatrix} \mathbf{x}(k+1) \\ \mathbf{w}(k+1) \end{bmatrix} &= \begin{bmatrix} \mathbf{\Phi} & \mathbf{\Gamma}_{\mathrm{d}}\mathbf{C}_{\mathrm{d}} \\ \mathbf{0} & \mathbf{\Phi}_{\mathrm{d}} \end{bmatrix} \begin{bmatrix} \mathbf{x}(k) \\ \mathbf{w}(k) \end{bmatrix} + \begin{bmatrix} \mathbf{\Gamma} \\ \mathbf{0} \end{bmatrix} \mathbf{u}(k) \\ \mathbf{y}(t) &= \begin{bmatrix} \mathbf{C} & \mathbf{0} \end{bmatrix} \begin{bmatrix} \mathbf{x}(t) \\ \mathbf{w}(t) \end{bmatrix}. \end{aligned} \tag{4.11}$$

With a constant disturbance, the system model takes a simpler form

$$\begin{aligned} \begin{bmatrix} \mathbf{x}(k+1) \\ \mathbf{w}(k+1) \end{bmatrix} &= \begin{bmatrix} \mathbf{\Phi} & \mathbf{\Gamma}_{\mathrm{d}} \\ \mathbf{0} & \mathbf{I} \end{bmatrix} \begin{bmatrix} \mathbf{x}(k) \\ \mathbf{w}(k) \end{bmatrix} + \begin{bmatrix} \mathbf{\Gamma} \\ \mathbf{0} \end{bmatrix} \mathbf{u}(k) \\ \mathbf{y}(t) &= \begin{bmatrix} \mathbf{C} & \mathbf{0} \end{bmatrix} \begin{bmatrix} \mathbf{x}(t) \\ \mathbf{w}(t) \end{bmatrix}, \end{aligned} \tag{4.12}$$

where the system matrix of the disturbance model decreases to the identity matrix.

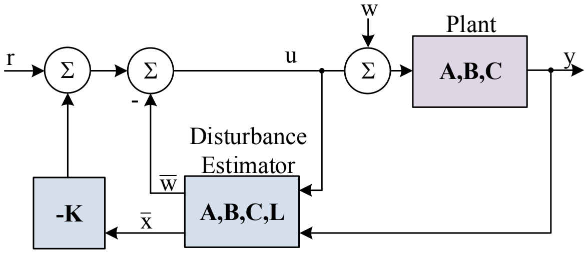

Figure 4.7. Block diagram of the LQR-based feedback controller together with the disturbance estimator.

4.2.5 Radial position control with the H_∞ loop-shaping approach

Robustness is defined in order to ensure that the system under control is stable with a certain amount of model uncertainty. In the robust control approach, the uncertainty is evaluated mathematically. The H_∞ approach is one method in the field of robust control. The H_∞ control is based on finding a stabilizing controller that minimizes the H_∞ norm (Skogestad and Postlethwaite, 2001). Different versions of the H_∞ control synthesis have been developed after its invention in the late 1980s. In the mixed-sensitivity H_∞ control, the sensitivity functions are shaped with weighting functions to minimize the H_∞ norm of the sensitivity function. A signal-based H_∞ method minimizes the selected error signal with respect to the model uncertainty. In the loop-shaping method, the open-loop plant is shaped with the weighting functions. Coprime factor uncertainty is used to guarantee the robustness limits. In **Publication VII**, the loop-shaping robust control method is applied to the radial position control of a bearingless rotor system. A two-degree-of-freedom control form is used, where the reference input has a weighting function of its own. A block diagram of the control problem is depicted in Fig. 4.8. The tuning iteration begins with weighting the open-loop system model as

$$\mathbf{G}_\mathrm{s}(\mathrm{j}\omega) = \mathbf{G}(\mathrm{j}\omega)\mathbf{W}_1(\mathrm{j}\omega), \tag{4.13}$$

where $\mathbf{G}_\mathrm{s}$ is the shaped open-loop system model, $\mathbf{G}$ is the system model, and $\mathbf{W}_1$ is the diagonal weight matrix. The weighted open-loop system model is arranged into the coprime factor form as

$$\begin{aligned}\mathbf{G}_s(s) = \mathbf{M}_\mathrm{s}^{-1}(s)\mathbf{N}_\mathrm{s}(s) = (\mathbf{M}_\mathrm{s} + \mathbf{\Delta}_\mathrm{Ms})^{-1}(s)\\ + (\mathbf{N}_\mathrm{s} + \mathbf{\Delta}_\mathrm{Ns})(s),\end{aligned} \tag{4.14}$$

where $\mathbf{M}_\mathrm{s}$ and $\mathbf{N}_\mathrm{s}$ are the coprimes of the system model, and $\mathbf{\Delta}_\mathrm{Ms}$ and $\mathbf{\Delta}_\mathrm{Ns}$ are unknown transfer functions of the perturbed disturbance. The stabilizing feedback controller is synthesized by minimizing

$$\left\| \begin{bmatrix} \mathbf{K}_2 \\ \mathbf{I} \end{bmatrix} (\mathbf{I} - \mathbf{G}_\mathrm{s}\mathbf{K}_2)^{-1}\mathbf{M}_\mathrm{s}^{-1}, \right\|_\infty \leq \epsilon^{-1}, \tag{4.15}$$

where $\mathbf{K}_2$ is the feedback controller gain matrix, and ϵ is the maximum perturbation.

The designer prefilters the open-loop system response with the weighting function

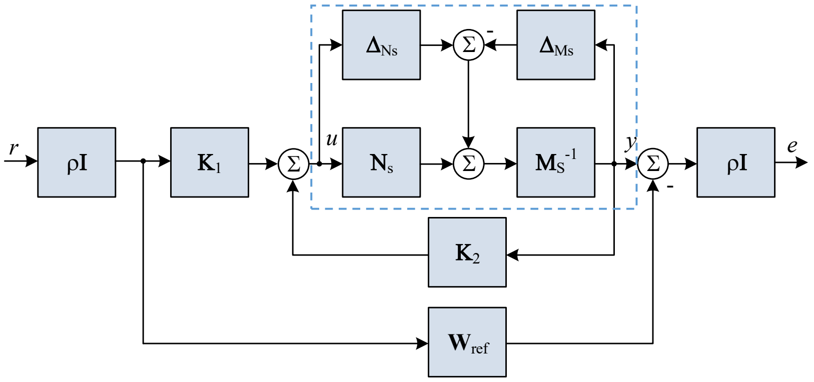

Figure 4.8. Block diagram of the H_∞ loop-shaping with the 2-DOF design scheme.

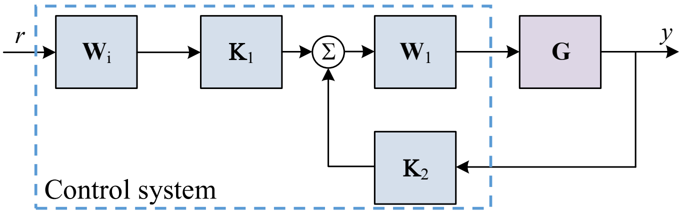

Figure 4.9. Block diagram of the implemented H_∞ controller.

$$\mathbf{W}_1(\mathrm{j}\omega) = \mathbf{I}_{4\times4} \cdot \frac{s + w_{\mathrm{a1}}}{s + w_{\mathrm{a2}}} \cdot \frac{s + w_{\mathrm{b}}}{w_{\mathrm{b}}} \cdot \frac{w_{\mathrm{c}}}{s + w_{\mathrm{c}}}, \tag{4.16}$$

where $w_{\text{a,b,c}}$ is the weighting parameter of the prefilter. The first transfer function is used to provide sufficient gain in the DC area. The crossover frequency behavior is tuned by the latter transfer functions. The selected parameters can be found in Appendix A.
The reference model is designed to follow the second-order system dynamics as

$$\mathbf{W}_{\mathrm{ref}}(\mathrm{j}\omega) = \mathbf{I}_{4\times4} \cdot \frac{\omega_{\mathrm{ref}}^2}{s^2 + 2\omega_{\mathrm{ref}} s + \omega_{\mathrm{ref}}^2}, \tag{4.17}$$

where ω_{ref} is the bandwidth of the reference weight. To guarantee a zero offset between the system output and the reference input, the following input filter is implemented

$$\mathbf{W}_{\mathrm{i}} \triangleq [(\mathbf{I} - \mathbf{G}_{\mathrm{s}}(s))\mathbf{K}_2(s))^{-1}\mathbf{G}_{\mathrm{s}}(s)\mathbf{K}_1(s)]^{-1}\mathbf{W}_{\mathrm{ref}}(s)|_{s=0}, \tag{4.18}$$

where $\mathbf{W}_{\mathrm{i}}$ is the input filter gain matrix, and $\mathbf{K}_1$ is the reference gain. The designed controller is discretized with the sampling time, and the implementation of the full controller is presented in Fig. 4.9.

4.3 Torque control

From the torque control perspective, the bearingless machine behaves as a traditional electrical machine. Depending on the machine type, a suitable control scheme can be selected without any specific features. From the levitation control's point of view, the additional flux path caused by the torque generation acts as a disturbance. This effect is based on the machine design and the loading condition. However, in this work, the cross-coupling between levitation and torque windings is neglected as the machine is driven in the no-load condition.

4.3.1 Scalar control

The simplest method to rotate a permanent magnet synchronous machine is to take a scalar control approach. For high-speed applications where no fast load dynamics is present, the

scalar control is suitable (Halkosaari, 2006). An additional benefit of this control method is sensorless operation.
The scalar control of dual motor bearingless machines is depicted in Fig. 4.10. In this method, the same voltage reference based on the speed command is sent to the VFDs of the both motors.

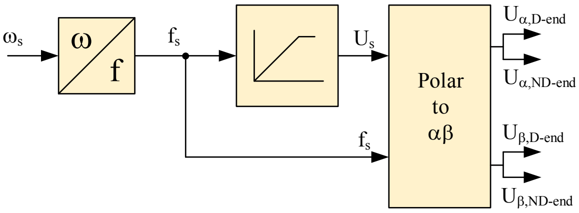

Figure 4.10. Scalar control for dual bearingless motors.

4.4 Experimental results

The presented modeling approach and the controllers used in the study are experimentally verified with the prototype machine. An identification method is used for the model and controller verification. The functionality of the bearingless machine is tested with lift-up, levitation, and rotational experiments.

4.4.1 Model validation

Model validation is an important phase in the model-based control implementation. Errors in the modeling can cause difficulties during operation. An identification procedure is used to measure the system dynamics. By comparing the measured system dynamics with the analytical model, the correspondence can be verified. The identification procedure is conducted in practice by injecting an excitation signal into the system to excite a frequency spectrum of interest. The system model can be calculated as

$$G(\mathrm{j}\omega) = \frac{Y(\mathrm{j}\omega)}{U(\mathrm{j}\omega)}, \tag{4.19}$$

where $G(\mathrm{j}\omega)$ is the model of the system to be identified, $Y(\mathrm{j}\omega)$ is the system output, and $U(\mathrm{j}\omega)$ is the excited input signal. A basic setup of the implemented identification setup is illustrated in 4.11. The block diagram presents the excitation signal inputs, where d_i is the signal injected to the plant input and d_o is the signal to the plant output. The plant model can be identified from the response between the excitation signal d_o and the system output y. Similarly, the system output sensitivity can be determined between d_o and the output y.

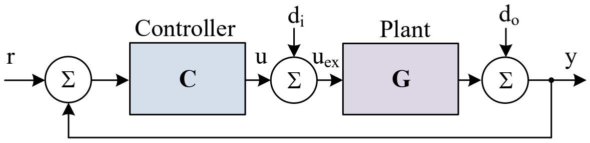

Figure 4.11. Block diagram of the general identification measurement setup.

The excitation signal is produced by using the pseudorandom binary sequence (PRBS) method in the frequency spectrum of 1 to 750 Hz. The identified plant model is compared with the analytical model in Fig. 4.12.

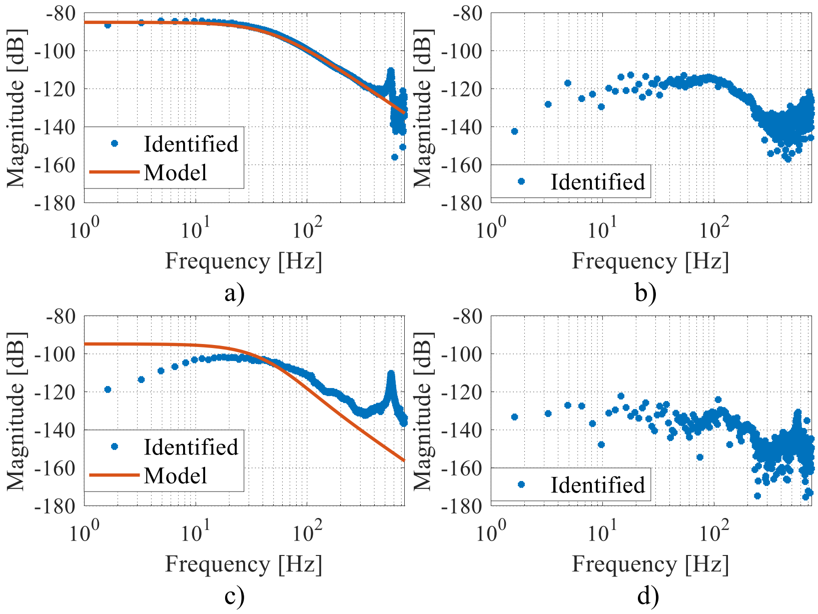

Figure 4.12. Identified plant model of the D-end x-axis, where the responses are from the D-end x-axis to a) D-end x-axis, b) D-end y-axis, c) ND-end x-axis, and d) ND-end y-axis.

The results show that the rigid dynamics corresponds well with the analytical model. However, the cross-coupling dynamics does not follow the model. It is clear that the cross-coupling is not fully described in the analytical model, and for this reason, further analysis is needed.

4.4.2 Levitation experiments

The performance of the designed controllers is tested with practical experiments. The most straightforward initial test is lifting the rotor to the origin from the backup bearings, which is the magnetic center of the bearingless motor. The lift-up test with pole placement and the LQR controller is presented in Fig. 4.13. These experiments are discussed in **Publication V**. The upper diagram pair presents the simulation and measurement results of the pole placement method. Correspondingly, the lower figure pair presents the simulation and measurement results of the LQR control approach.

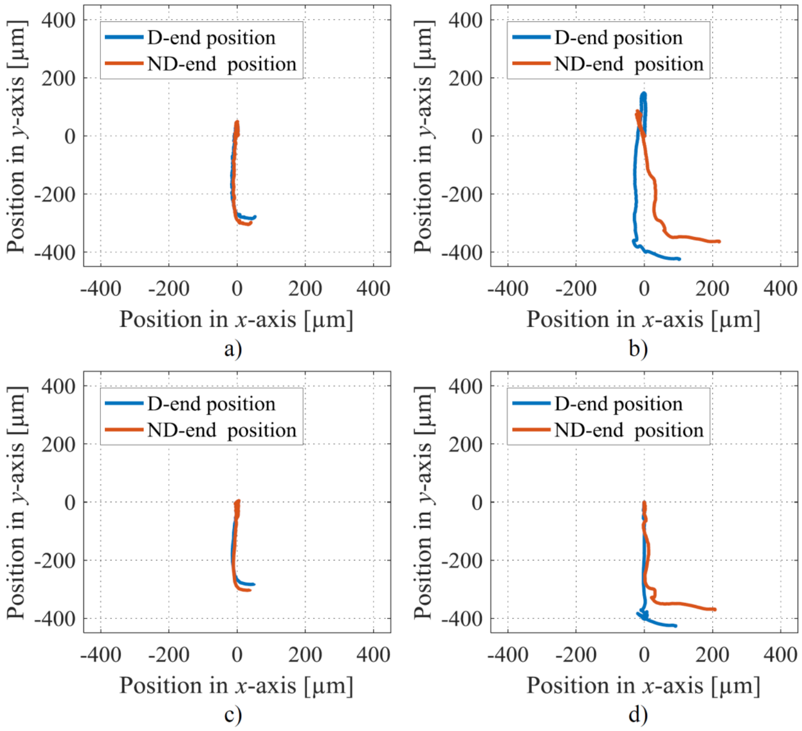

Figure 4.13. Rotor lift-up test; a) simulation with pole placement, b) experimental test with pole placement, c) simulation with LQR, and d) experimental test with LQR.

The results show that the best performance is achieved with the LQR control approach. Compared with pole placement, LQR generates no overshoot, whereas in the pole placement lift-up test, the overshoot is 170 µm at the D-end motor. In principle, the simulation results follow the experimental results. However, the responses are larger in the experimental results, which indicates that the applied model does not fully describe the system behavior. It is pointed out that the initial starting position of the rotor is lower in the experimental case as the mechanical center and the magnetic center are not aligned. Moreover, the presented modeling approach is effective to describe the bearingless rotor system behavior. The LQR control approach using Bryson's tuning rule simplifies the control synthesis and provides superior performance compared with the pole placement method.

In **Publication VII**, a loop-shaping H_∞ controller for the bearingless rotor system is considered. The identification routine described in Section 4.4.1 is used to experimentally determine the system output sensitivity. In this case, the excitation signal is injected into the plant output, and the response is analyzed between the excitation signal and system outputs. The system sensitivity to the output disturbance is depicted in Fig. 4.14.

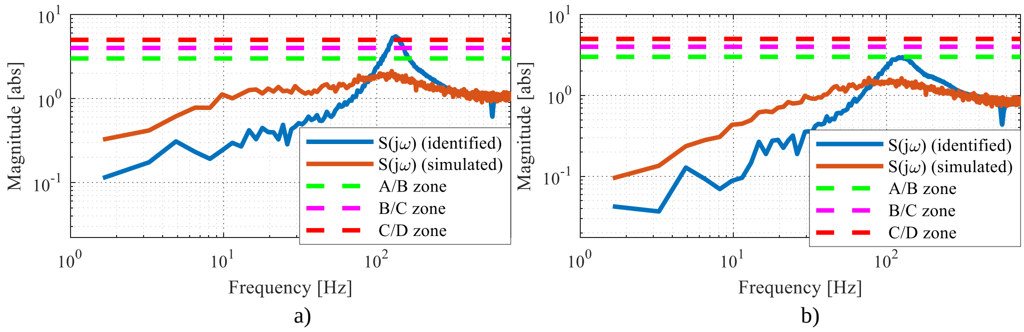

a)

b)

Figure 4.14. Identified system output sensitivity compared with simulation, employing a) PID controller and b) H_∞ loop-shaping controller.

In this experiment, a SISO PID-based radial position controller is compared with a MIMO controller that is tuned by using the loop-shaping H_∞ approach. Furthermore, in Fig. 4.14, the sensitivity function limits are drawn. The measurement results show that the sensitivity peak of the SISO PID controller reaches to the D zone. The sensitivity with the H_∞ controller reaches to the limit of the A zone. On the other hand, the simulation results show a much better sensitivity response. This indicates that the model is not accurate enough. A comparison between the analytical model and the identified one is presented in Fig. 4.12. It is seen that the diagonal part of the model is accurate but the cross-coupling between the axes includes nonmodeled dynamics. Moreover, the H_∞ controller provides a peak sensitivity that is within the acceptable limits defined by the standard. However, a more accurate system model is needed to improve the control performance.

4.4.3 Rotation experiments

The synthesized 5-DOF levitation controllers are experimentally tested under rotor rotation. In **Publication V**, a model-based control approach is presented using pole placement and LQR control methods. The initial rotation test is conducted with the LQR radial position controller applying a low rotational speed at 300 r/min. Experimental results of the initial rotation test are illustrated in Fig. 4.15. The test is carried out by supplying a rotating electrical field to the D-end motor. The results show the rotating current waveforms of the both levitation windings and the D-end motor winding. The experimental results confirm that the presented control approach is able to levitate and rotate the bearingless rotor system.

In **Publication VI**, an LQR controller with the disturbance estimator approach is applied

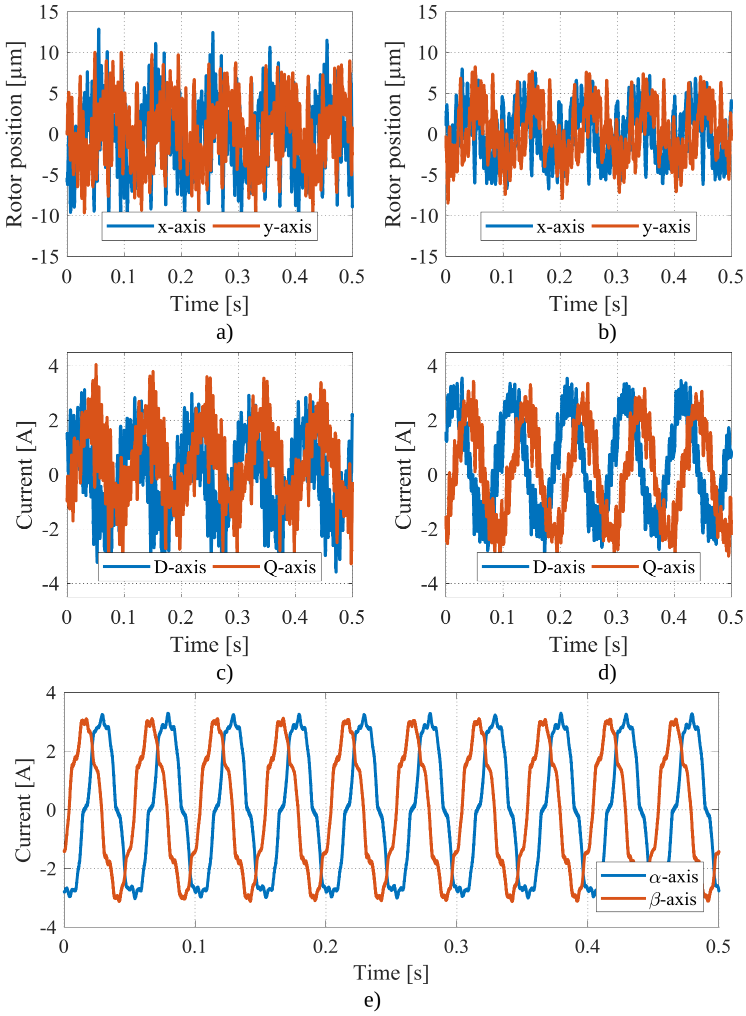

Figure 4.15. Initial rotation test at 300 r/min; a) rotor position at the D-end motor, b) rotor position at the ND-end motor, c) levitation winding current at the D-end motor, d) levitation winding current at the ND-end motor, and e) rotating current in the stator reference frame at the D-end motor.

to the radial position regulation of the rotor system. In this experiment, the rotor is rotated up to 1500 r/min. The operating speed is bound to this value owing to limitations in the control system. A rotating electrical field is synchronously applied to both motors by using the scalar control method presented in Fig. 4.10. The current waveforms of the levitation and torque windings are depicted in Fig. 4.16 during operation at 1500 r/min. The results show that the harmonic content of the levitation winding is increased compared with the measurement in Fig. 4.15. In other words, the rotor vibration is increasing as a function of rotational speed caused by an unbalance and run-out in the measurement

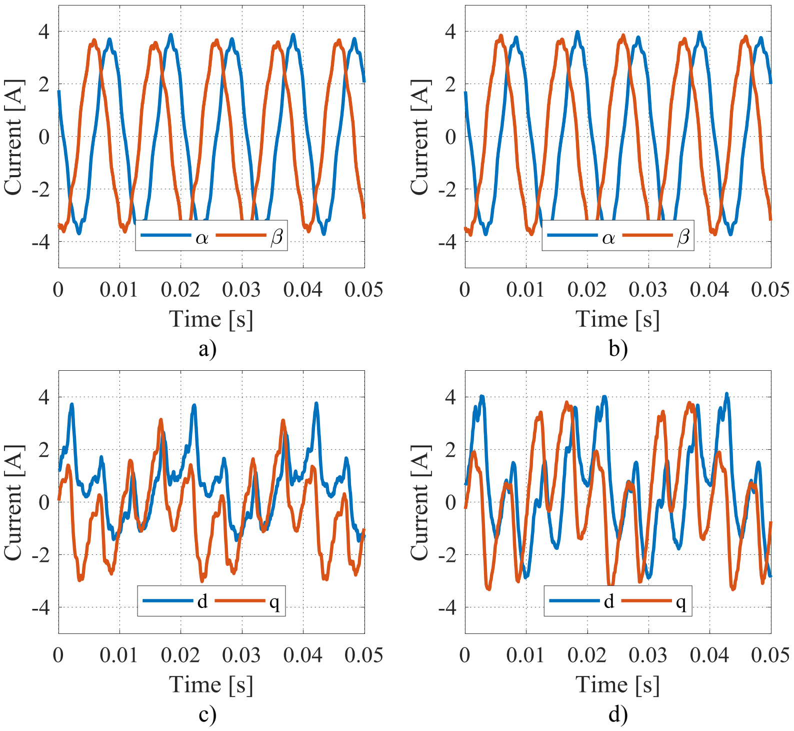

a) b) c) d)

Figure 4.16. Motor and levitation currents at 1500 r/min

surfaces. The rotor position during the rotation experiment is presented in Fig. 4.17, where the orbits of both ends are shown.

Moreover, the acceptable vibration level is indicated in the figure. From the orbits it can be seen that the vibration is mainly caused by the harmonics. The frequency spectrum of the rotor vibration in the speed range of 150 and 1500 r/min is presented in Fig. 4.18 and 4.19. The frequency spectrum shows the amplitude of the rotor unbalance, which is synchronous with the rotational speed. It is steadily increasing as a function of speed. However, the main reason for the vibration is seen in the 3rd harmonic content. This part is mainly caused by the run-out effect caused by the uneven measurement plane surfaces (Kim and Lee, 1997). Based on the achieved results, it can be concluded that the levitation system is behaving acceptably during the rotation. Nevertheless, the vibration levels must be observed at higher operating speeds.

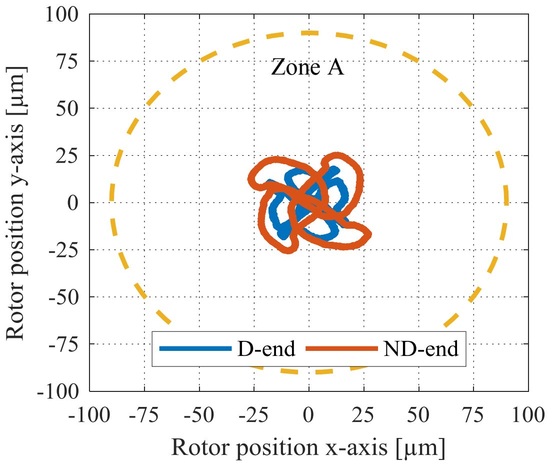

Figure 4.17. Rotor orbits at 1500 r/min.

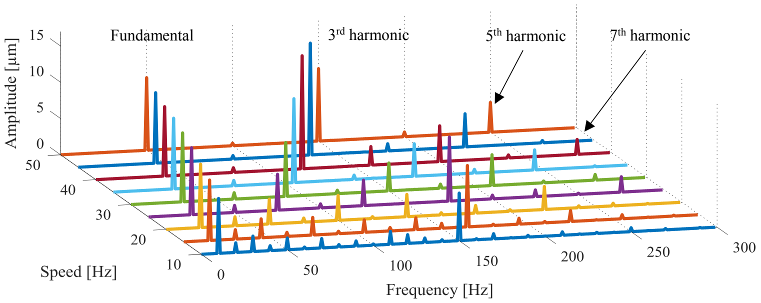

Figure 4.18. Frequency spectrum of the rotor position at the D-end motor from 150 r/min to 1500 r/min.

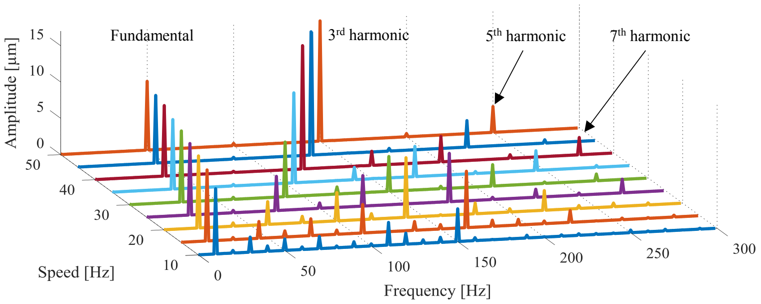

Figure 4.19. Frequency spectrum of the rotor position at the ND-end motor from 150 r/min to 1500 r/min.

5 Conclusions and future study

In this doctoral dissertation, an IPM bearingless machine was analyzed from the design and control perspectives. The work was divided into three parts focusing on the design, modeling, and control of the IPM bearingless machine. A significant part of the optimization of the bearingless machine design was performed with the help of FEM tools where the initial parameters were obtained from an analytical method. The motor optimization aimed at ensuring the controllability of the designed machine. The FEM-based design of the machine was verified by experimental results. Moreover, the design scalability for a higher power region was analyzed. As the design problem contains multiple variables, genetic algorithm methods were applied to further automate the design process. For the model-based control approach, MIMO modeling of the bearingless system was presented. Several controllers were synthesized based on the MIMO model including pole placement, LQR, and H_∞ methods. Experimental tests were conducted to verify the presented modeling and control approaches for the bearingless machine.

Publications I–IV concentrated on problems related to bearingless machine design. In **Publication I**, the force error angle was optimized for an IPM bearingless machine by varying the pole angle of the permanent magnets. The proposed design was scaled up to tenfold, and the performance was analyzed in **Publication II**. Further minimization of the force error angle was achieved by applying stator skew. In **Publication III**, a bearingless motor with tooth-coil windings was considered. Different stator and rotor skew constructions were analyzed to minimize the additional harmonics caused by the selected winding arrangement. A design procedure that applies a genetic algorithm was proposed in **Publication IV**. As the overall design problem is multivariable, a genetic algorithm can be used to automate the process. A genetic algorithm can be applied in the predesign phase when initial parameters are determined with an analytical approach.

In **Publications V–VII**, the model-based control of the IPM bearingless machine was studied. A model-based control approach based on a rigid rotor model was introduced for the IPM bearingless machine in **Publication V**. Pole placement and LQR controllers were applied to the radial position control. The controllers were experimentally verified by lift-up and rotation tests. In **Publication VI**, the rotor vibration levels were measured and compared with an ISO standard. In this case, the LQR controller with a disturbance estimator was used. Finally, in **Publication VII**, the loop-shaping H_∞ robust controller method was employed and the performance was compared with the SISO PID control approach. A system identification method was used to experimentally determine the output sensitivity of the controllers. The results were compared with the ISO standard that defines the limits for acceptable sensitivity peaks. Furthermore, the identified plant model was compared with the analytical model. It was found that the cross-coupling between the same axes at different motor units is not fully described by the analytical model.

5.1 Future study

The scope of the presented doctoral dissertation is wide, and thus, potential approaches to future research are manifold. The focus of the future study can be divided into design- and control-related problems. Considering the design issues of bearingless motors, as presented in the literature, many motor types can be equipped with the bearingless function. However, for high-speed applications, the selection of suitable motor types is more limited. For high-speed applications, the most convenient types are permanent magnet and induction motors. Permanent magnet motors have a higher efficiency; however, the mechanical design calls for specific attention. An induction motor is an attractive choice for a high-speed application as the rotor can be very rigid when using a solid rotor structure and the produced radial force is higher than with other motor types. On the other hand, the induction motor cannot compete in efficiency, and its controllability is uncertain. However, in applications where the rotor is exposed to high temperatures, a permanent magnet construction is not the best solution. An interesting question is: what are the limitations for high-speed and high-power industrial bearingless machines in terms of mechanical, thermal, electromagnetic, and control analysis?

Furthermore, magnetic levitation systems typically involve displacement sensors, which are used to observe the rotor movement and are needed in the closed-loop control. A synthesized controller is implemented in a control system that usually has high calculation power. This spare calculation power with position sensor information can be used for system diagnostics. This kind of measurement setup can be employed to estimate possible faults in the system. Secondly, the calculation power can be used to automate the control tuning for example by applying an adaptive control. In general, the control platform available can be used to provide additional information about the system state and help the user adapt to changes if necessary.

References

Amati, N., Bonfitto, A., Suarez, L.D., and Tonoli, A. (2016). Turbomolecular pumps on conical active magnetic bearings. In: *15th International Symposium on Magnetic Bearings (ISMB)*, Kitakyushu, Japan, pp. 323–330.

Amemiya, J., Chiba, A., Dorrell, D.G., and Fukao, T. (2005). Basic characteristics of a consequent-pole-type bearingless motor. *IEEE Transactions on Magnetics*, 41(1), pp. 82–89. ISSN 0018-9464, doi:10.1109/TMAG.2004.840179.

Bryson, A.E. and Ho, Y.C. (1975). *Applied optimal control*. New York: Routledge. ISBN 9781315137667.

Cheng, M., Han, P., Buja, G., and Jovanović, M.G. (2018). Emerging multiport electrical machines and systems: past developments, current challenges, and future prospects. *IEEE Transactions on Industrial Electronics*, 65(7), pp. 5422–5435. ISSN 0278-0046, doi:10.1109/TIE.2017.2777388.

Chiba, A. and Fukao, T. (1998). Optimal design of rotor circuits in induction type bearingless motors. *IEEE Transactions on Magnetics*, 34(4), pp. 2108–2110. ISSN 0018-9464, doi:10.1109/20.706817.

Chiba, A., Power, D.T., and Rahman, M.A. (1991a). Characteristics of a bearingless induction motor. *IEEE Transactions on Magnetics*, 27(6), pp. 5199–5201. ISSN 0018-9464, doi:10.1109/20.278786.

Chiba, A., Power, D.T., and Rahman, M.A. (1991b). No load characteristics of a bearingless induction motor. In: *Conference Record of the 1991 IEEE Industry Applications Society Annual Meeting*, vol. vol.1, Dearborn, MI, USA, pp. 126–132.

Chiba, A., Rahman, M.A., and Fukao, T. (1991c). Radial force in a bearingless reluctance motor. *IEEE Transactions on Magnetics*, 27(2), pp. 786–790. ISSN 0018-9464, doi: 10.1109/20.133292.

Chiba, A., Sotome, K., Iiyama, Y., and Rahman, M.A. (2011). A novel middle-point-current-injection-type bearingless PM synchronous motor for vibration suppression. *IEEE Transactions on Industry Applications*, 47(4), pp. 1700–1706. ISSN 0093-9994, doi:10.1109/TIA.2011.2155611.

Chiba, A., et al. (2005). *Magnetic bearings and bearingless drives*, pp. 1–15. Amsterdam, The Netherlands: Elsevier. ISBN 978-0-7506-5727-3.

Earnshaw, S. (1842). On the nature of the molecular forces which regulate the Constitution of Luminiferous Ether. *Transaction of the Cambridge Philosophical Society*, 7, pp. 97–112.

Franklin, G.F., Powell, J., and Workman, M.L. (2010). *Digital control of dynamic systems*, pp. 364, 400–401. 1200 Pilarcitos Ave. Halfmoon Bay, CA 94019: Ellis-Kagle Press. ISBN 978-0-9791226-1-3.

Genta, G. (2005). *Dynamics of rotating systems*, p. 5. Springer-Verlag London. ISBN 0-387-20936-0.

Gruber, W., Amrhein, W., and Haslmayr, M. (2009). Bearingless segment motor with five stator elements – Design and optimization. *IEEE Transactions on Industry Applications*, 45(4), pp. 1301–1308. doi:10.1109/TIA.2009.2023560.

Gruber, W., Rothböck, M., and Schöb, R.T. (2015). Design of a novel homopolar bearingless slice motor with reluctance rotor. *IEEE Transactions on Industry Applications*, 51(2), pp. 1456–1464. doi:10.1109/TIA.2014.2341739.

Halkosaari, T. (2006). Optimal U/f-control of high speed permanent magnet motors. In: *IEEE International Symposium on Industrial Electronics*, vol. 3, Montreal, Canada, pp. 2303–2308. ISSN 2163-5137.

Holmes, F.T. (1937). Axial magnetic suspension. *Review of Scientific Instruments*, 8, pp. 444–447. doi:doi.org/10.1063/1.1752213.

Huang, J., Li, B., Jiang, H., and Kang, M. (2014). Analysis and control of multiphase permanent-magnet bearingless motor with a single set of half-coiled winding. *IEEE Transaction on Industrial Electronics*, 61(7), pp. 3137–3145. ISSN 0278-0046, doi:10.1109/TIE.2013.2279371.

Ichikawa, O., Chiba, A., and Fukao, T. (2001). Inherently decoupled magnetic suspension in homopolar-type bearingless motors. *IEEE Transactions on Industry Applications*, 37(6), pp. 1668–1674. ISSN 0093-9994, doi:10.1109/28.968177.

ISO 14839-2:2004(E) (2004). *Mechanical vibration – Vibration of rotating machinery equipped with active magnetic bearings – Part 2: Evaluation of vibration*. Standard. Geneva, CH: International Organization for Standardization.

ISO 14839-3:2004(E) (2004). *Mechanical vibration – Vibration of rotating machinery equipped with active magnetic bearings – Part 3: Evaluation of stability margin*. Standard. Geneva, CH: International Organization for Standardization.

ISO 1940-1:2003(E) (2003). *Mechanical vibration – Balance quality requirements for rotors in a constant (rigid) state – Part 1: Specification and verification of balance tolerances*. Standard. Geneva, CH: International Organization for Standardization.

Jaatinen, P., et al. (2016). Automated parameter identification platform for magnetic levitation systems: case bearingless machine. In: *15th International Symposium on Magnetic Bearings (ISMB)*, Kitakyushu, Japan, pp. 275–281.

Jastrzebski, R., Jaatinen, P., and Pyrhönen, O. (2016). Efficiency of buried permanent magnet type 5kW and 50kW high-speed bearingless motors with 4-pole motor windings and 2-pole suspension windings. In: *15th International Symposium on Magnetic Bearings (ISMB)*, Kitakyushu, Japan, pp. 172–179.

Khoo, W.K.S. (2005). Bridge configured winding for polyphase self-bearing machines. *IEEE Transactions on Magnetics*, 41(4), pp. 1289–1295. ISSN 0018-9464, doi: 10.1109/TMAG.2005.845837.

Kim, C.S. and Lee, C.W. (1997). In situ runout identification in active magnetic bearing system by extended influence coefficient method. *IEEE/ASME Transactions on Mechatronics*, 2(1), pp. 51–57. ISSN 1083-4435, doi:10.1109/3516.558858.

Kultere, K. and Presch, D. (2018). *Energy audit guide for motor drive systems – Recommended steps and tools*. Technical report. IEA 4E Electric Systems Annex.

Matsuzaki, T., et al. (2012). Rotor structure suppressing suspension force ripple in an IPM type bearingless motor with 2-pole motor windings and 4-pole suspension windings. In: *2012 XXth International Conference on Electrical Machines*, Marseille, France, pp. 744–750.

Michioka, C., et al. (1996). EEJ Proceedings of Meeting of Rotating Machinery. In: *Radial force of homopolar-type bearingless motors in no load condition*, pp. 91–100 (in Japanese).

Miller, J.M. (2010). *Propulsion systems for hybrid vehicles (2nd Edition)*, p. 172. Institution of Engineering and Technology. ISBN 978-1-84919-147-0.

Oishi, R., Horima, S., Sugimoto, H., and Chiba, A. (2013). A novel parallel motor winding structure for bearingless motors. *IEEE Transactions on Magnetics*, 49(5), pp. 2287–2290. ISSN 0018-9464, doi:10.1109/TMAG.2013.2240279.

Okada, Y., Miyamoto, S., and Ohishi, T. (1996). Levitation and torque control of internal permanent magnet type bearingless motor. *IEEE Transactions on Control Systems Technology*, 4(5), pp. 565–571. ISSN 1063-6536, doi:10.1109/87.531922.

Ooshima, M., Chiba, A., Rahman, A., and Fukao, T. (2004). An improved control method of buried-type IPM bearingless motors considering magnetic saturation and magnetic pull variation. *IEEE Transactions on Energy Conversion*, 19(3), pp. 569–575. ISSN 0885-8969, doi:10.1109/TEC.2004.832065.

Ooshima, M., Kobayashi, A., and Narita, T. (2015). Stabilized suspension control strategy at failure of a motor section in a d-q axis current control bearingless motor. In: *IEEE Industry Applications Society Annual Meeting*, Addison, TX, USA, pp. 1–7.

Ooshima, M., et al. (1994). Characteristics of a permanent magnet type bearingless motor. In: *Proceedings of 1994 IEEE Industry Applications Society Annual Meeting*, vol. 1, Denver, CO, USA, pp. 196–202.

Pyrhönen, J. (1991). The high-speed induction motor: calculating the effects of solid-rotor material on machine characteristics. *Acta polytechnica scandinavica*, Electrical Engineering Series no. 68. Doctoral dissertation.

Pyrhönen, J., Jokinen, T., and Hrabovcová, V. (2013). *Design of rotating electrical machines*, 2nd edn. Chichester: John Wiley Sons, Ltd. ISBN 978-1-118-58157-5.

Schweitzer, G. and Maslen, E.H. (2009). *Magnetic bearings*, pp. 1–82. Springer-Verlag Berlin Heidelberg. ISBN 978-3-642-00496-4.

Sikora, B. and Pilat, A.K. (2018). Hybrid axial active magnetic bearing design, modelling and prototype. In: *16th International Symposium on Magnetic Bearings (ISMB)*, Beijing, China, pp. 1–8.

Skogestad, S. and Postlethwaite, I. (2001). *Multivariable feedback control analysis and design*, pp. 372–376. John Wiley Sons. ISBN 0-13-525833-2.

Smirnov, A. (2012). *AMB system for high-speed motors using automatic commissioning*. Doctoral dissertation. Lappeenranta University of Technology, Lappeenranta, Finland.

Sun, X., Shi, Z., Chen, L., and Yang, Z. (2016a). Internal model control for a bearingless permanent magnet synchronous motor based on inverse System Method. *IEEE Transactions on Energy Conversion*, 31(4), pp. 1539–1548. ISSN 0885-8969, doi: 10.1109/TEC.2016.2591925.

Sun, X., et al. (2016b). High-performance control for a bearingless permanent-magnet synchronous motor using neural network inverse scheme plus internal model controllers. *IEEE Transactions on Industrial Electronics*, 63(6), pp. 3479–3488. ISSN 0278-0046, doi:10.1109/TIE.2016.2530040.

Tetsuo Ohishi, Y.O. and Dejima, K. (1994). No load characteristics of a bearingless induction motor. In: *Fourth International Symposium on Magnetic Bearings*, Zurich, Switzerland, pp. 201–206.

van der Geest, M., Polinder, H., Ferreira, J.A., and Christmann, M. (2015). Power density limits and design trends of high-speed permanent magnet synchronous machines. *IEEE Transactions on Transportation Electrification*, 1(3), pp. 266–276. ISSN 2332-7782, doi:10.1109/TTE.2015.2475751.

Wang, H., Bao, J., Xue, B., and Liu, J. (2015). Control of suspending force in novel permanent-magnet-biased bearingless switched reluctance motor. *IEEE Transactions on Industrial Electronics*, 62(7), pp. 4298–4306. ISSN 0278-0046, doi: 10.1109/TIE.2014.2387799.

Webster, J.E. and Eren, H.E., eds, (2014). *Measurement, Instrumentation, and Sensors Handbook*. CRC Press.

Yang, Y., et al. (2010). A control strategy for bearingless switched-reluctance motors. *IEEE Transactions on Power Electronics*, 25(11), pp. 2807–2819. ISSN 0885-8993, doi:10.1109/TPEL.2010.2051684.

Appendix A

Table A.1. System parameters of the 5 kW bearingless motor

Parameter	Symbol	Value	Unit
Rated speed	Ω	30 000	r/min
Rated power per motor unit	P	5	kW
Resistance	R	0.27	Ω
Inductance	L_d	0.91	mH
Inductance	L_d	0.93	mH
Rated voltage (Y)	u	400	V
Rated current	i	8.4	A
Coil turns per phase	n	5	
Pole pairs	p	2	
Levitation			
Resistance	R	0.27	Ω
Inductance	$L_\mathrm{d,q}$	3.27	mH
Current stiffness	K_i	29	N/A
Position stiffness	K_x	672	N/mm
Rated voltage (Y)	u	400	V
Rated maximum current	i	8	A
Coil turns per phase	n	10	
Pole pairs	p	1	
Controller parameters			
Distance to sensor location	c, d	211	mm
Distance to bearingless motor	a, b	107.5	mm
Sampling time	T_s	50	μs
Proportional gain	K_P	42000	A/m
Integrator gain	K_I	$8.2\cdot10^5$	As/m
Derivative gain	K_D	103	A/ms
Filter coefficient	T_f	100	
Prefilter parameter	w_a1	150	
Prefilter parameter	w_a2	0.1	
Prefilter parameter	w_b	600	
Prefilter parameter	w_c	800	
Reference model bandwidth	ω_ref	370	rad/s
Scalar gain	ρ	1	
Current controller bandwidth	ω_cc	5654.9	rad/s
Position controller bandwidth (H_∞)	ω_pc	351.8	rad/s
Position controller bandwidth (PID)	ω_pc	333	rad/s

Table A.1. (Continued)

Parameter	Symbol	Value	Unit
	Dimensions		
Rotor mass	m	11.65	kg
Rotor inertia	J	0.232	kgm^2
Stator outer diameter		150	mm
Stator inner diameter		70	mm
Rotor diameter		68.8	mm
Shaft diameter		33	mm
Shaft length		507	mm
Tooth width		5.9	mm
Air gap length	s_0	0.6	mm
Magnet thickness		2.5	mm
Gap width around the magnet		0.05	mm
Stack length		59	mm
	Materials		
Bakker/Nd-Fe-B Magnet		N38SH	
Lamination material		SURA NO20	

Appendix B

Table B.1. Parameters of the 100 kW bearingless motor

Parameter	Symbol	Value	Unit
Rated speed	Ω	22 000	r/min
Rated power per motor unit	P	50	kW
Resistance	R	0.03	Ω
Rater voltage (Y)	u	690	V
Rated current	i	51	A
Power factor	$cos\phi$	0.95	Ω
Coil turns per phase	n	32	
Pole pairs	p	2	
Levitation			
Resistance	R	0.09	Ω
Current stiffness	K_i	57	N/A
Position stiffness	K_x	954	N/mm
Rated voltage (Y)	u	400	V
Rated maximum current	i	8	A
Coil turns per phase	n	32	
Pole pairs	p	1	
Dimensions			
Rotor mass	m	21.5	kg
Rotor inertia	J	0.52	kgm^2
Stator outer diameter		220	mm
Stator inner diameter		84.8	mm
Rotor diameter		83	mm
Shaft diameter		35	mm
Shaft length		649	mm
Tooth width		10	mm
Air gap length	s_0	0.9	mm
Magnet thickness		3.6	mm
Gap width around the magnet		0.05	mm
Stack length		72.5	mm
Materials			
Hitachi/Nd-Fe-B Magnet		NMX-S41EH	
Lamination material		SURA NO20	
Slot wedge material		MAGNOCAL 2067	

Appendix C

The force measurement platform to determine the radial forces acting on the rotor is presented in Fig. C.1. Rotor position can be controlled in the air gap with stepper motors. The smallest step size is 1.4 μm. Forces can be measured in the xyz axis. In the xy axis, the maximum measured force is ± 1900 N with a resolution of 0.32 N. The maximum force that can be measured in the z-axis is ± 3800 N with a resolution of 0.43 N.

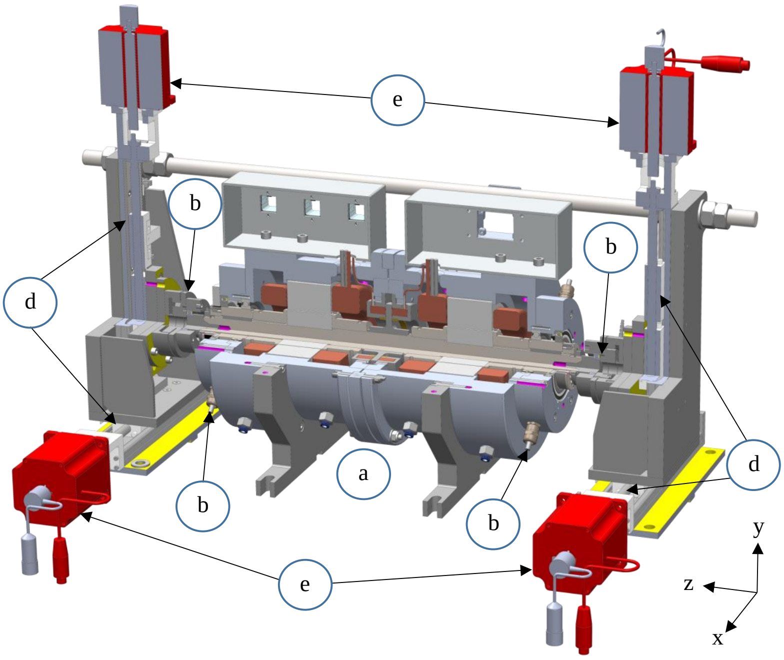

Figure C.1. Custom-made force measurement platform comprises the following components: a) bearingless machine under investigation, b) eddy-current position measurement sensors in the bearingless machine, c) three-axis force measurement sensor, d) linear track where the rotor can be positioned in the xy plane, and e) stepper motors that control the rotor position (Jaatinen et al., 2016).

Table C.1. Force measurement platform

Component	Manufacturer
Industrial PC	Beckhoff C6930
Analog-to-digital convecter	Beckhoff EL3702
Stepper motor	Beckhoff AS1060
Linear track	Hiwin KK60
Force sensor	ATI Industrial Automation Mini85

Appendix D

The rotor vibration level zones and sensitivity limits are based on the ISO standard. The zones are described as follows; Zone A is for newly commissioned system for continuous operation, Zone B is acceptable when operating for unrestricted long time periods, Zone C is acceptable for short time periods and when operating in Zone D may cause a damage to the system.

Table D.1. Recommended criteria of zone limits (ISO 14839-2:2004(E), 2004).

Limit	Rotor displacement D_{max}
Zone A	$< 0.3\ C_{min}$
Zone B	$< 0.4\ C_{min}$
Zone C	$< 0.5\ C_{min}$
Zone D	$> 0.5\ C_{min}$

Table D.2. Recommended criteria of zone limits (ISO 14839-3:2004(E), 2004).

Limit	Peak output sensitivity
Zone A/B	9.5 dB
Zone B/C	12 dB
Zone C/D	14 dB

Publication I

Jaatinen, P., Jastrzebski, R. P., Sugimoto, H., Pyrhönen, O., and Chiba, A.
Optimization of the rotor geometry of a high-speed permanent magnet bearingless motor with segmented magnets

Reprinted with permission from
Proceedings of the 18th International Conference on Electrical Machines and Systems (ICEMS), Pattaya, Thailand
pp. 962–967, 2015
©2015, IEEE

2015 18th International Conference on Electrical Machines and Systems (ICEMS), Oct. 25-28, 2015, Pattaya City, Thailand

Optimization of the rotor geometry of a high-speed interior permanent magnet bearingless motor with segmented magnets

P. Jaatinen[1*], R.P. Jastrzebski[1], H. Sugimoto[2], O. Pyrhönen[1], A. Chiba[2]
[1] Lappeenranta University of Technology, Finland
[2] Tokyo Institute of Technology, Japan
E-mail: pekko.jaatinen@lut.fi

Abstract — Bearingless motors combine the torque generation of electrical motors and the radial suspension force capabilities of traditional magnetic bearings. The magnetomotive force (MMF) distribution in the motor generates radial force interference. The interference force affects the angle between the actual and desired radial force. This angle is called the force error angle. For stable levitation of the rotor of the bearingless motor the force error angle must be minimized in the design phase of the machine. This paper presents an optimal rotor structure for minimization of the error angle in a high-speed interior permanent magnet bearingless motor with magnets embedded in the rotor surface.

I. INTRODUCTION

Active magnetic bearing (AMB) technology has evolved in the past decades to become a feasible solution for high-speed motor applications. Features of the AMBs are superior compared to traditional ball or roller bearings and other bearing technologies. AMBs use a magnetic field to suspend the rotor without any mechanical contact. This feature overcomes the mechanical restrictions of traditional bearings. Because a motor with AMBs does not need any lubrication, such motors are suitable for oil-free environments. Diagnostic and operational supervision functions can be integrated into the AMB system by taking advantage of the built-in position measurement sensors and magnetic actuators. For these reasons AMBs are used in many high-speed motor applications such as compressors, pumps and flywheel energy storage systems [1].

When a rotor is equipped with AMBs the rotor length is increased due to the space needed for the radial and axial magnetic bearings. The increased rotor length lowers the rotor bending mode frequencies, which can cause problems if the bending mode frequency decreases to close to or into the operation region.

Bearingless motors or self-bearing motors offer a viable replacement to more traditional AMB-rotor systems [2]. This technology combines the electrical motor and radial AMB properties into a one-stator structure. An additional benefit from using a bearingless motor construction is that standard three-phase inverters can be used, which leads to a reduced number of switching components [2].

Traditional motor types that can be equipped with a bearingless function include induction, permanent magnet, synchronous reluctance and switched reluctance type motors [2]. Induction type bearingless motor can produce higher radial force than surface permanent magnet bearingless motors. However, squirrel-cage type induction bearingless motors need a special type of rotor to improve the efficiency and radial force production capabilities [2]. The achieved radial force in interior permanent magnet (IPM) type bearingless motors is close to that of induction type motors [3]. No special rotor arrangements are needed with IPM motors. Permanent magnet type bearingless motor have a high power factor than in induction and reluctance motors.

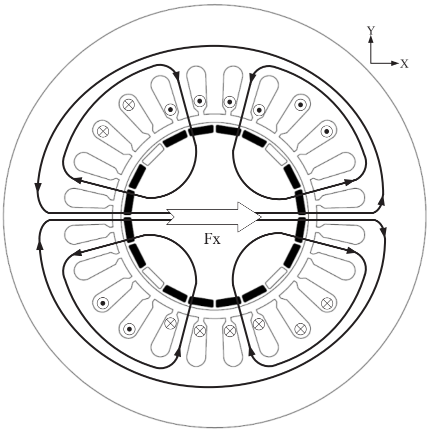

Fig. 1. Working principle of the bearingless motor.

II. MOTOR STRUCTURE

The motor under study is an interior permanent magnet type bearingless motor with magnets embedded close to the rotor surface. This type of motor provides better radial force, mechanical strength, and demagnetization and thermal properties than its surface mounted magnet counterpart [4]. The designed bearingless motor is equipped with four non-salient magnetic poles. Machine rated power is 5 kW and rated rotation speed is 30 000 r/min. The magnet poles are segmented into smaller pieces to gain higher mechanical strength against the centrifugal force and to reduce eddy current losses in the magnets.

In the bearingless motor, two three-phase winding sets are wound on the one-stator core. The winding sets are called the torque and the suspension windings. To achieve the required levitation force, a configuration of 2-pole suspension windings and 4-pole motor windings was chosen.

Figure 1 presents the working principle of the bearingless motor. The figure shows the flux paths of the 4-pole motor windings and the 2-pole suspension windings. The 2-pole flux produced by the suspension windings decreases the air-gap flux on the left-hand side of the air-gap and increases that on the right-hand side. This asymmetry generates a radial force in a positive *x*-direction. Switching the polarity of the suspension winding current results in a change in the force direction. For simplicity, only U-phases are illustrated.

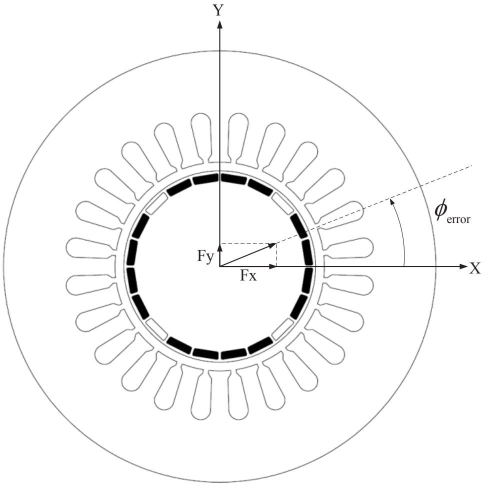

Fig. 2 Error angle definition.

III. FORCE ERROR ANGLE

The rotor radial position is controlled in the *xy*-coordinate system, where the origin of the coordinate is placed at the geometrical center of the rotor. When controlling the rotor in a certain direction, for example along the x-axis, a smaller force is generally present also along the y-axis. This force depends on the rotation angle. Angle deviation between the desired and actual force is called the force error angle [5]. Fig. 2 illustrates this angle, which is presented mathematically:

$$\phi_{error} = \tan^{-1}\frac{F_y}{F_x}. \tag{1}$$

Misalignment between the *x*- and *y*- force components can be caused by eddy currents, gyroscopic effects, or permeance distribution and spatial space harmonics of the magnetomotive force (MMF) [2]. Measurement delay of the rotor position and calculation delay of the force command also affect the error angle. For this reason, the interference between the force components must be carefully assessed in the design phase of a bearingless motor. An additional benefit from minimization of the error angle is reduced power consumption in the suspension windings [6].

An error angle larger than 15 degrees reduces the damping of the rotor such that levitation is no longer possible due to high rotor vibration [2].

In this work to guarantee enough damping for the rotor, the highest acceptable error angle was chosen in the design phase as five degrees.

IV. MAGNET CONFIGURATION OPTIMIZATION

As presented in papers [5] and [6] the radial force can be derived from the motor MMF components using the following assumptions:

1. The rotor is postitioned at the magnetic center point of the stator
2. The radial force is generated only under the iron poles
3. The magnetic material is linear
4. The flux flows only in the radial direction

The motor MMF components are air-gap MMF caused by the permanent magnets, MMF caused by the suspension windings and MMF due to the motor windings. In this study the motor current is not considered so the MMF equation can be simplified to:

$$A(\phi_m) = A_{PM} + A_s\,, \tag{2}$$

where A_{PM} is MMF caused by air-gap flux and A_s is MMF caused by the suspension windings.

In paper [6] magnet pole pitch was varied to minimize the effect of the MMF harmonic components of the suspension windings. It was noticed that smaller rotor pole pitch produced smaller error angle. In [6], the analysis was, however, based on the consequent pole rotor where the salient iron pole is between the magnets. Assumptions 2 and 3 are not valid in the case of IPM motors. In the prototype design there is only a small iron bridge because of the non-salient and segmented magnet rotor structure. These small bridges between the magnets and in the rotor surface will saturate easily.

Due the magnetic saturation it is more challenging to derive accurate analytical equations for IPM motors. The analysis in this paper is based only on FEM-results.

Eight different segmented rotor structures, from 16 magnets to 44 magnets were used to find the most suitable magnet configuration. Fig. 3 illustrates the studied rotor structures. Using less than 16 segmented magnets is not feasible because of the mechanical strength requirements of the rotor at the nominal speed. Upper limit was determined the manufacturability and assembly of the magnets.

The presented rotor structures were studied with finite element analysis software to determine the optimal magnet configuration, segmentation and pole pitch. Only radial force production capability and quality were considered in the optimization. Maximum suspension current was used in the FEM simulation.

In earlier work related to IPM bearingless motors the total number of magnets was 44 magnets, embedded in the rotor surface [8]. The initial number of magnets was chosen as 20 in the machine presented in this paper. The reason for this selection was to gain higher air-gap flux density compared to the machine presented in literature. Higher air-gap flux is gained from the larger amount of magnet material. However, with 20 embedded magnets, as Fig. 4 shows, the archived error angle was outside the design requirements and fluctuated considerably.

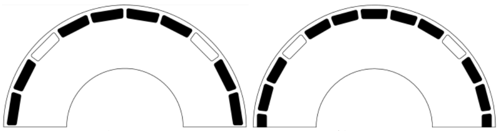

a) 16 magnets b) 20 magnets

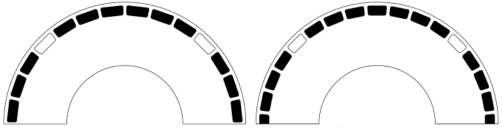

c) 24 magnets d) 28 magnets

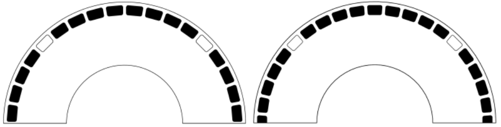

e) 32 magnets f) 36 magnets

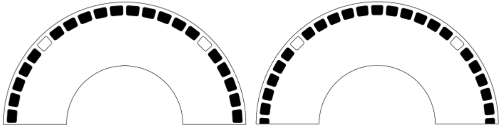

e) 40 magnets f) 44 magnets

Fig. 3. Different magnet configurations.

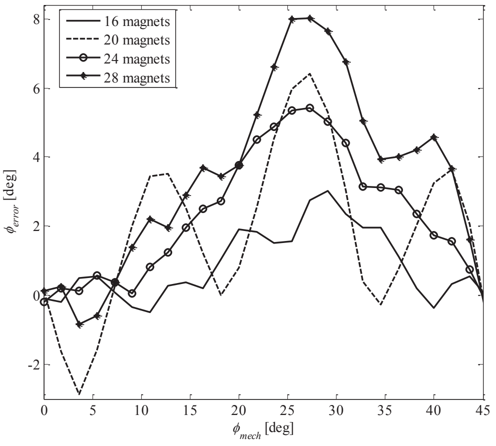

Fig. 4. Error angle comparison between the first four rotor configurations.

Fig. 4 presents error angle waveforms of the first four rotor configurations, namely, 16, 20, 24 and 28 magnets. Only suspension currents are supplied for force generation in *x*-axis. It can be seen that the effect of the magnet configurations on the error angle is significant. The error angle is small in case of 16 magnets. The difference between the 16 and 28 magnet configurations is greater than 50 percent. These results correspond with those presented in paper [7]. Smaller magnet pole pitch results in smaller harmonic content in the suspension winding MMF.

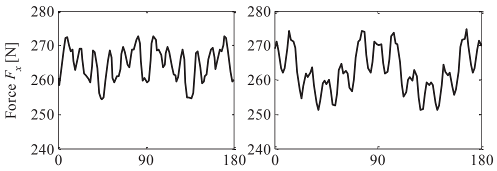

(a) 16 magnets (b) 20 magnets

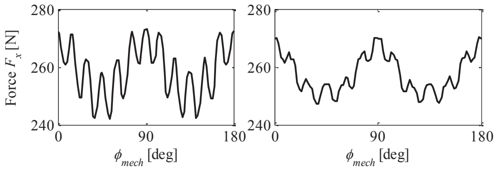

(c) 24 magnets (d) 28 magnets

Fig. 5. Radial force waveform in *x*-direction

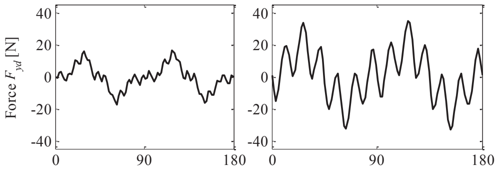

(a) 16 magnets (b) 20 magnets

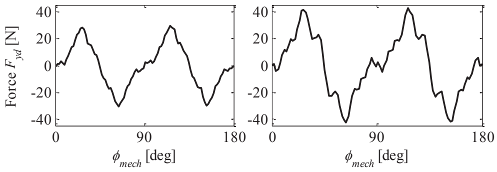

(c) 24 magnets (d) 28 magnets

Fig. 6. Radial disturbance force waveform in y-axis

Fig. 5 and 6 show the force amplitude waveforms in the *x*- and *y*-directions, respectively. It is noteworthy that the force ripple in the *x*-direction is smallest in the case of 16 magnets in the rotor. The disturbance force magnitude in the *y*-axis is smallest with 16 magnets. Harmonics analyses were done for the *x*- and *y*-axis force components, which are presented in Fig. 7 and 8. The main harmonic components are the 2nd and 4th harmonics. The slot openings cause the 12th harmonic. These components cause the radial force fluctation and are responsible for the magnitude of the disturbance force. Further error angle minimization is possible if special winding arrangements are used to compensate the highest harmonic components [7].

Fig. 9 compares the error angle and the force ripple of all rotor structures considered. It can be noted that the error angle starts to decrease after 32 magnets. However, the force ripple increases. The effect for 32 or more magnets is not congruent with the results presented in [7]. This effect needs further investigation. It can be noted that the slot ripple harmonic is reduced. It is also understood that 44 magnets in [8] has reasonable low force error angle and ripple, however 16 magnets provide better performance.

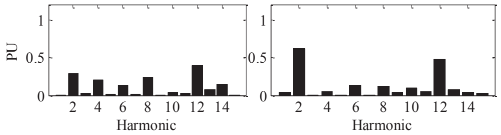

(a) 16 magnets (b) 20 magnets

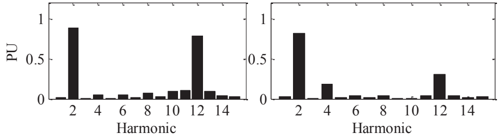

(c) 24 magnets (d) 28 magnets

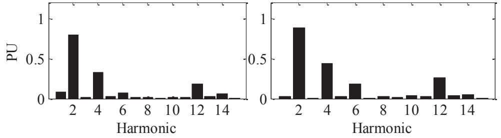

(e) 32 magnets (f) 36 magnets

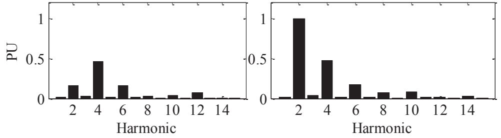

(g) 40 magnets (h) 44 magnets

Fig 7. Harmonic order of the radial force x-component.

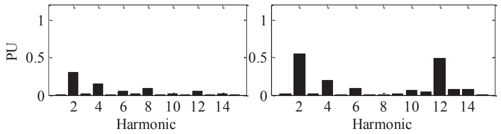

(a) 16 magnets (b) 20 magnets

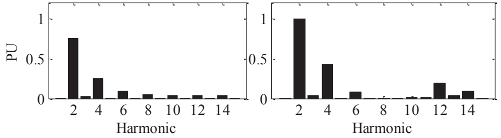

(c) 24 magnets (d) 28 magnets

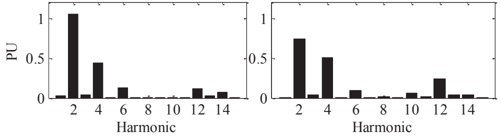

(e) 32 magnets (f) 36 magnets

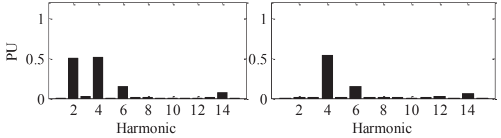

(g) 40 magnets (h) 44 magnets

Fig. 8. Harmonic order of the radial force y-component.

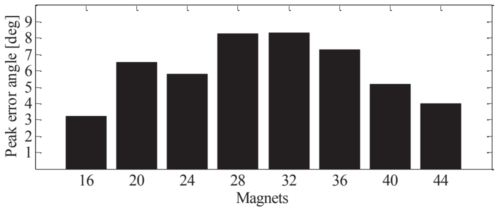

(a) Maximum error angle

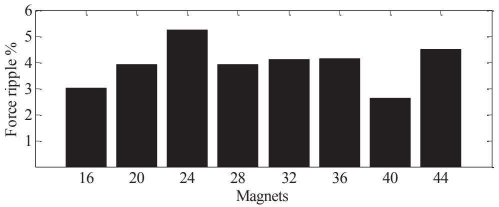

(b) Mean force ripple

Fig. 9. a) Peak error angle between *x*- and *y*- axis force b) Maximum radial force ripple.

V. SUSPENSION FORCE PERFORMANCE ANALYSIS

As the FEM analysis result showed the rotor structure with 16 magnets caused smallest error angle due to smallest harmonic content. Further suspension force performance analysis is done using this rotor structure. Motor radial force production was analyzed at rated torque with varied suspension current between 0-8A. Motor parameters are presented in Table I. Fig. 10 presents a comparison of the error angle where maximum suspension current is applied with no torque and at rated torque. Error angle magnitude is not notably affected by the torque producing current.

Force-current linearity was analyzed for nominal torque and no torque. It can be noticed in Fig. 11 that the slope changes as a function of the torque. This change must be taken into account in the controller. The force needed to lift-up the rotor from the back-up bearings is 215 N, including forces caused by gravity and the unbalance magnet pull.

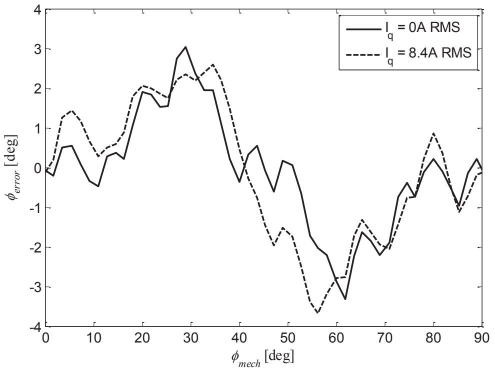

Fig. 10. Error angle comparison between load and no load condition.

This force corresponds to a 6.5A current in the suspension windings in the no load condition. These result shows that it is possible to lift up the rotor with additional 500g weight of the impeller wheel without over current. Different suspension current values from 1 to 8 A were analyzed at rated torque, shown in Fig. 12. When the rotor is operating ± 50 µm from the magnetic center point the required suspension current is below 2A. The radial force produced in this situation is close to constant. Higher forces are only needed in the lift-up phase, to levitate the rotor, or in the case of external disturbance.

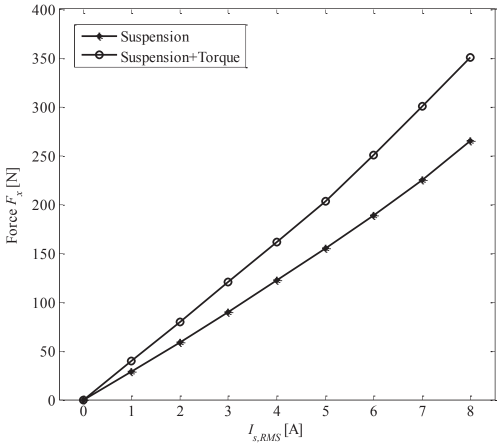

Fig. 11. Force-current linearity at no motor current and rated operation point.

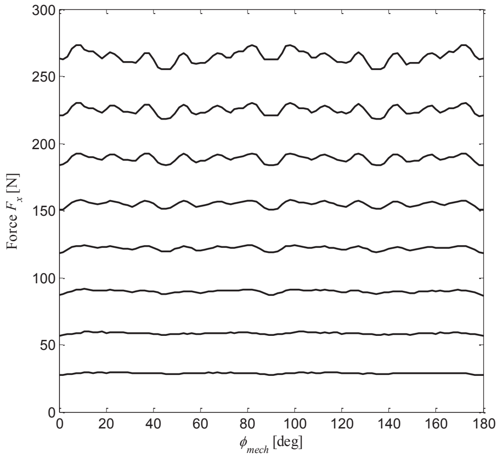

Fig. 12. Radial force in the positive x-direction at rated operation point.

Fig. 13 presents torque and motor current linearity with different suspension currents. It can be seen that the produced torque is not significantly affected by the suspension current.

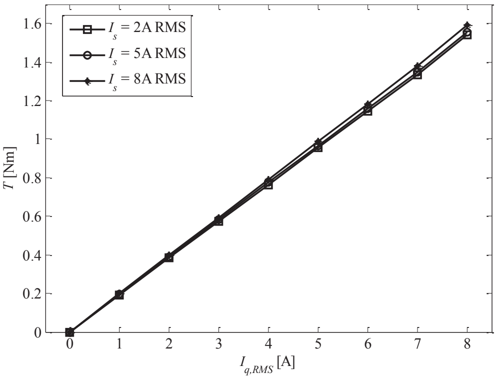

Fig. 13. Torque linearity with respect of the motor and the suspension current.

TABLE I
Motor parameters

Motor type	IPM 4-pole 3-phase
Motor output power	5 kW
Rated speed	30000 r/min
Rated torque	1.59 Nm
Voltage	400 V
Current	8.4 A
Power factor	0.88
Suspension windings	2-pole 3-phase
Voltage	250 V
Current	8 A
Magnetic air gap	0.6 mm
Mechanical air gap	0.25 mm
Rotor outer diameter	68.8 mm
Stator inner diameter	70 mm
Stator outer diameter	150 mm
Stack length	59 mm
Magnet height	2.5 mm
Magnet type	NdFeB
Rotor weight	5,5 kg
Needed radial force	215 N

VI. CONCLUSION

Different rotor magnet configurations were analyzed using finite element analysis software. The results are plotted in Fig. 9. The rotor structure with 16 magnets provided the best outcome. It can be concluded that the error angle and radial force ripple can be reduced by selecting the optimal number of segmented magnets. It was noted that special winding schemes are not needed to attain acceptable error angle. It was shown that designed bearingless motor can provided enough lift-up force to levitate the rotor without any problems.

Based on the achieved results it can be concluded that it is important to consider the rotor structure of IPM bearingless motor to improve overall performance of the force production of the suspension windings.

Future study will require confirmation of the FEM results with a prototype machine.

ACKNOWLEDGMENT

The authors would like to express their gratitude to the Academy of Finland, grant No. 270012 and No. 273489, for financial support. The mechanical design was partially sponsored by the LUT School of Technology investment project: Reconfigurable Laboratory Rig for Testing Various Strategic Components of High-speed Applications. The work was carried out during the research visit of Pekko Jaatinen and Rafal Jastrzebski to the Tokyo Institute of Technology. The visit was co-funded by an International Mobility Grant from LUT School of Technology.

VII. REFERENCES

[1] E. E. Swanson, E. H. Maslen, G. Li, and C. H. Cloud, "Rotordynamic design audits of AMB supported machinery," in Proc. 37th Turbomachinery Symposium, College Station, TX, USA, 2008, pp.133-158

[2] A. Chiba, T. Fukao, O. Ichikawa, M. Oshima, M. Takemo, and D.G. Dorrell, "Magnetic bearings and bearingless drive", Amsterdam, The Netherlands: Elsevier, 2005.

[3] Y. Okada, S. Miyamoto, T. Ohishi, "Levitation and torque control of internal permanent magnet type bearingless motor", IEEE Transactions on Control System Technology, vol.4, no.5, Sep 1996, pp. 565-571

[4] M. Ooshima, A. Chiba, A. Rahman, T. Fukao, "An improved control method of buried-type IPM bearingless motor considering magnetic saturation and magnetic pull variation", Energy conversion, IEEE Transaction on, vol.19, no.3, Sept. 2004, pp. 569-575

[5] J. Asama, R. Natsume, H. Fukuhara, T. Oiwa, A. Chiba, "Optimal suspension winding configuration in a homo-polar bearingless motor", IEEE Transaction on Magnetics, vol.48, no. 11. Nov. 2012, pp. 2973-297

[6] J. Amemiya, A. Chiba, D.G. Dorrell, T. Fukao, "Basic characteristics of a consequent-pole-type bearingless motor" IEEE Transaction on Magnetics, vol.41, no. 1, Jan. 2005, pp. 82-89

[7] J. Asama, R. Kawata, T. Tamura, T. Oiwa, A. Chiba, "Reduction of force interference and performance improvement of a consequent-pole bearingless motor", Precision Engineering, vol.36, issue 1, Jan. 2012, pp. 10-18.

[8] M. Ooshima, K. Yamashita, A. Chiba, M. A. Rahman, T. Fukao, "An improved control method of buried-type IPM bearingless motors Considering Magnetic Saturation and Magnetic Pull Variation", IEEE International Electrical Machines and Drives Conference (IEMDC), vol.2, June 2003, pp. 1055-1060

Publication II

Jastrzebski, R. P., Jaatinen, P., Sugimoto, H., Pyrhönen, O., and Chiba, A.
Design of a bearingless 100 kW electric motor for high-speed applications

Reprinted with permission from
Proceedings of the 18th International Conference on Electrical Machines and Systems (ICEMS), Pattaya, Thailand
pp. 2008–2014, 2015
©2015, IEEE

2015 18th International Conference on Electrical Machines and Systems (ICEMS), Oct. 25-28, 2015, Pattaya City, Thailand

Design of a bearingless 100 kW electric motor for high-speed applications

R. P. Jastrzebski[1], P. Jaatinen[1], H. Sugimoto[2], O. Pyrhönen[1], A. Chiba[2]
[1] Lappeenranta University of Technology, Finland
[2] Tokyo Institute of Technology, Japan
E-mail: rafal.jastrzebski@lut.fi

Abstract — In this work a design optimization of the high-speed buried-type interior permanent magnet bearingless motor with significant power for such machines is presented. The geometry, windings arrangement and magnets are adjusted from the non-levitated motor design to avoid the significant magnetic saturation and achieve the performance target without oversizing the machine. The analytical design is optimized in finite element method analysis. The effect of stator skew on machine performance is thoroughly investigated.

Keywords: High-speed electrical machines, bearingless motor, permanent magnet motor, magnetic bearing, magnetic levitation, stator skew.

I. INTRODUCTION

For high-speed demanding applications the traditional mechanical bearings have to be replaced by either fluid bearings or magnetically levitated rotors. A typical industrial solution of 5-degrees of freedom (5-DOF) magnetically levitated rotor system comprises two radial active magnetic bearings (AMBs) and separate axial thrust AMB installed on the same shaft as the electrical motor or generator. AMBs provide frictionless, clean oil-free and low-maintenance operation with built-in monitoring and rotor position control capabilities. The advantages come in expense of added space, cost and complexity. The better system integration can be achieved by combining motor and bearings into one electromagnetic actuator.

Until recently, all the investigated bearingless motors have been designed for very low power up to a few kW, whereas AMB rotor systems have been long present also in high-power applications (e.g. SKF pipeline compressors). Notably in [1] a caned pump application of 30 kW 3000 r/min induction bearingless motor has been described. In [2] and [3] a 40 kW surface mounted permanent magnet (PM) bearingless motor with carbon fiber composite bandage have been reported and its loss has been measured up to 30000 r/min. For bearingless motors the higher power levels and high-speed operation demand careful design optimization to ensure mechanical integrity, minimize the error angle, maximize control stability at different loading conditions and to minimize losses.

This work reports the design of a twin unit 3-phase bearingless motor with combined 100 kW power. Employment of bearingless motors and standard 3-phase converters leads to shorter rotor with higher bending frequencies, symmetrical rotor control structure and better system robustness. Machine footprint, number of components and cost can be reduced when compared to the equivalent AMB-rotor system with independent AMBs and motor. The optimized interior permanent magnet (IPM) rotor geometry, 4-layer winding and skew stator allow to add suspension without oversizing the motor design, as described in Chapter II, or without compromising motor efficiency. The axial suspension is realized by a thrust bearing located between 2 motor-radial bearing units. Being a standard component the axial AMB is only considered in mechanical system considerations in Chapter III. Performance results, some interactions between motoring and a radial levitation system and effects of a stator skew are presented in Chapters IV and V. Loss calculation results are given in Chapter VI.

II. DESIGN OPTIMIZATION

First, the standard motor design parameters are derived by the analytical methods [4], [5]. Second, the bearingless rotor and stator geometries are optimized according to theory presented in [6] and refined using finite element method (FEM) electromagnetic and stress analysis in JMAG-Designer. The resulting bearingless motor is of similar length as the starting point PM motor. In order to accommodate the suspension windings and increased flux densities the stator slot area, tooth width and stator and rotor yokes thicknesses have been enlarged. However, iron volume in bearingless design is not significantly greater than the iron volume in the analytical design of the standard motor. For example, a stator outer diameter is increased by 16.4 % (31 mm) and the tooth width is increased by 50.4 % (3.35 mm). The parameters of a single bearingless motor unit having 50 kW output are listed in Table I. With two units, output power of 100 kW is achieved. The rated rotational speed is 30,000 r/min. One unit has two sets of three-phase windings, one is for motor function and another is for radial suspension force generation. In the stator slot, there are motor conductors and suspension conductors. A suspension to motor windings ratio is selected 1:3 in terms of slot area.

Fig. 1 shows motor geometry. The IPM rotor comprises the segmented PMs with 0.9 mm thick laminated steel bridges between 4 PM segments per pole. Between the 4 poles there are flux barrier gaps without magnet, which prevent significant variations in permeance distribution between d-axis and q-axis. The magnets are embedded 0.9 mm under the rotor surface. A winding step shortening [4] is employed with 4/6 pitched motoring winding and 5/6 pitched suspension winding. The design stator current density rms value is 5 A/mm^2.

978-1-4799-8805-1/15/$31.00 ©2015 IEEE

III. Stress Analysis and Rotor Dynamics

The rotor geometry is limited by the yield strength of the laminations that is 400 MPa. Beyond that stress point the thin lamination bridges at the rotor circumference deform plastically and will not return to its original shape. In general, the thinner bridges result in smaller flux leakage, lower losses and decreased suspension force error angle. The minimization of direction angle error [6] that is angle difference between the desired and the actual force is the major challenge in the design of the bearingless motor geometry.

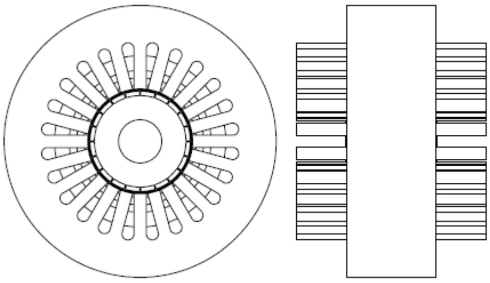

Fig. 1 Geometry outline of IPM single bearingless motor unit.

TABLE I
Main Parameters of Single Bearingless Motor Unit

Parameter	**Value**
Operating data of 3-phase 4-pole motor	
Rated mechanical power	50 kW
Rated speed	30000 r/min
Rated rms stator current Y	51 A
Rated rms line-to-line voltage Y	690 V
Power factor cosφ at rated op. point	0.95
Resistance of motor winding	0.03 Ω
Coil turns per phase	32
Operating data of 3-phase 2-pole suspension	
Rated rms stator current Y	17 A
Resistance of suspension winding	0.09 Ω
Coil turns per phase	32
Main geometry parameters and materials	
Stator outer diameter	220 mm
Stator inner diameter	84.8 mm
Rotor diameter	83 mm
Shaft diameter	35 mm
Tooth width	10 mm
Airgap length	0.9 mm
Magnet thickness	3.6 mm
Gap width around the magnet	0.05 mm
Stack length	72.5 mm
Rotor mass	2.58 kg
Hitachi/Nd-Fe-B Magnet	NMX-S41EH
Lamination material	SURA® NO20
Semi magnetic slot wedge material	MAGNOVAL® 2067

Fig. 2 (a) and (b) show the structural static study for 0.9 mm thickness of bridges and flux barriers around the segmented magnets in the laminated rotor and for 50 µm space around the magnets. This simulation neglects the glue between the iron and the magnets. In the simulated worst case the magnets are pushed to the outside. The magnets' middle outside section is in the contact with the iron leaving 50 µm free space at the sides and 100 µm free space next to their inner middle section. The shapes of the magnets and bridges affect the maximum stress, displacement and performance. For the simulated configuration the maximum stress determined in FEM is in the corner of the lamination bridge. The maximum displacement is at the rotor circumference in the middle of the bridge over the magnet. For the speeds of 20000, 30000 and 40000 r/min the maximum stress values are 172, 387 and 669 MPa. The maximum displacements are 4, 9 and 16 µm.

For the overall configuration the beam rotor model is constructed and the frequencies and shapes of the rotor bending modes are computed as listed in Fig. 3. The high frequency of the first bending mode of the rotor, that is 1029 Hz (61740 r/min), will alleviate the levitation control design for the subcritical system. The resulting rotor model can be used for model-based control design and veriffication.

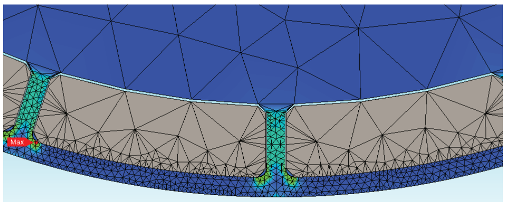

(a) Maximum stress apperaes next to the corner of the inner magnets in the rotor iron core.

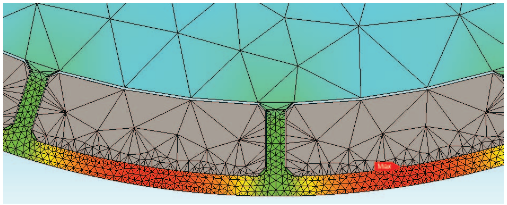

(b) Maximum displacement apperaes in the middle of the bridge over the magnets in the rotor iron core.

Fig. 2 Crosssections of the rotor and mesh in a structural static analysis.

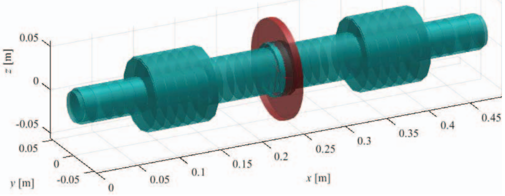

Fig. 3 Beam rotor model of twin-unit bearingless motor of combined 100 kW power. The first three bending modes of the exemplary configuration are at 1029 Hz, 2675 Hz and 4359 Hz. The total rotor mass is 11.2 kg.

IV. ELECTROMAGNETIC CALCULATION

The distributed winding and winding step shortening of the 4-pole winding result in the more sinusoidal phase-induced voltages as shown in Fig. 4. Three-phase voltages are drawn as a result of FEM analysis at terminals open. As a result the flux harmonic content is reduced. The similar effect is provided by the application of interior PMs and semi magnetic slot wedges.

Fig. 5 presents the unbalance magnetic pull force of single motor unit at no load and at nominal torque conditions. The permanent magnets in rotor generate radial force when the rotor is displaced from the center position. The strength of the magnet pull limits the mechanical clearence.

Fig. 6 shows the radial forces and the force direction angle errors at different suspension current amplitudes, at different motor loading and at nominal speed. Sinusoidal three-phase currents are fed in both motor and suspension windings. Force amplitude and direction have variations caused by space harmonics. The maximum radial force must be higher than the unbalance magnetic pull force. Based on the authors experience with the levitated rotor systems the clearance of 0.25 mm provides sufficient force capacity for an initial lift up with the model based controllers. Additionally, an overcurrent for the initial lift up can be applied in the suspension windings if required.

Fig. 7 shows shaft output torque with respect to the rotor rotational position at several motor currents with no suspension current. The torque variation is rather high at this stage without skew.

Fig. 8 shows mean force amplitude, mean force angle, peak force amplitude error, peak force angle error and peak torque ripple with respect to suspension current for several motor current values. The force production is linear as seen in Fig. 8(a). However, the current stiffness, that is the force as a function of suspension current and the mean force angle depend on the motor current as shown in Fig. 8 (a) and (b).

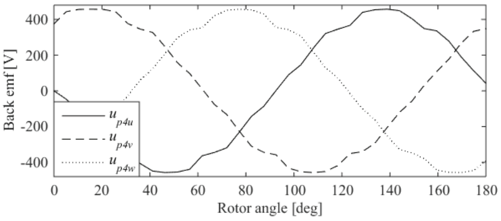

Fig. 4 FEM simulated phase induced voltages at 30000 r/min.

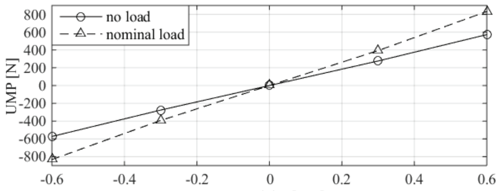

Fig. 5 Unbalance magnetic pull at no load and at nominal torque.

These characteristics have to be taken into account in the controller development. In Figs. 8 (c) to (e) the worst case force direction angle errors, force amplitude errors and torque ripple are observed at the maximum motor current amplitudes i_m=72 A and at the small suspension current amplitudes, e.g. i_s=6 A.

Fig. 9 shows flux density distribution at these currents. The peak flux density values in the motor teeth start to approach the saturation as observed. Series of FEM analysis is carried out at some current conditions. Table II lists the flux density in the airgap, middle of tooth, middle of stator yoke at some motor and suspension current conditions. The maximum flux density occurs at stator tooth at the maximum motor and suspension current. But the peak flux density is limited to 1.59 T.

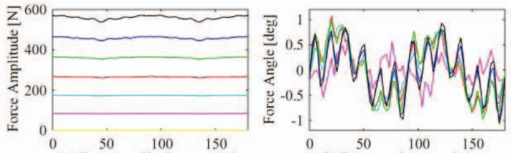

(a) Force amplitude at i_m=0 A (b) Force angle at i_m=0 A

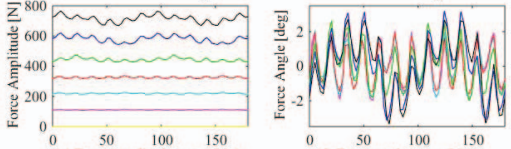

(c) Force amplitude at i_m=36 A (d) Force angle at i_m=36 A

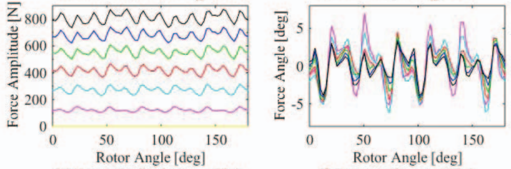

(e) Force amplitude at i_m=72 A (f) Force angle at i_m=72 A

Fig. 6 Suspension characteristics for the suspension current amplitude i_s from 0 to 24 A, Ω=30000 r/min, no skew and for some motor current amplitudes.

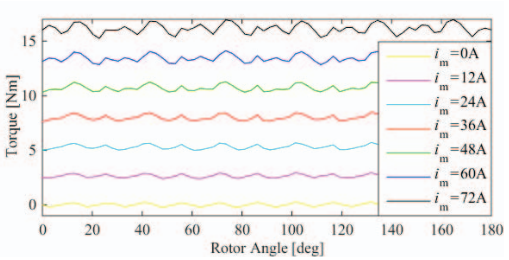

Fig. 7 Torque when i_s=0 A, Ω=30000 r/min and no skew.

Such a brief close to saturation condition of the teeth does not seem to obscure significantly the high-speed motor performance if the rotor operates without some eccentricity. Nevertheless, for the levitation performance the imbalance and close to saturation flux densities in the opposite teeth generate the aforementioned errors in the force direction angle and force amplitude. One solution would be to further increase the teeth width, yokes thicknesses and decrease the PM thickness up to the point were flux levels drop well below saturation point. This would require increasing rotor and stator diameters, which in turn would limit the performance, for example, maximum speed. An alternative solution is to introduce the skew in the rotor or in the stator.

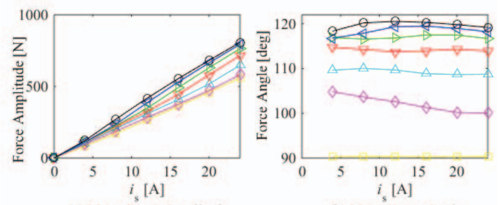

(a) Mean Force Amplitude (b) Mean Force Angle

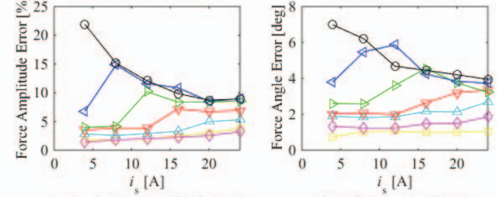

(c) Peak Force Amplitude Error (d) Peak Force Angle Error

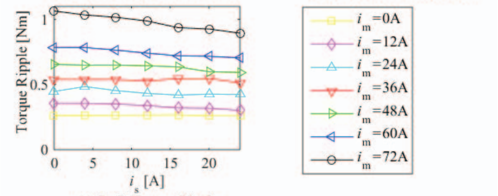

(e) Peak Torque Ripple

Fig. 8 Bearing and motor characteristics as a function of suspension and motor currents at Ω=30000 r/min and without skew.

TABLE II
FLUX DENSITIES IN BEARINGLESS MOTOR

Peak flux at different current amplitudes in the	**Value**
middle of airgap for i_m=0 A, i_s=0 A	0.77 T
middle of tooth for i_m=0 A, i_s=0 A	0.83 T
middle of tooth for i_m=0 A, i_s=24 A	1.18 T
middle of tooth for i_m=72 A, i_s=0 A	1.46 T
middle of tooth for i_m=72 A, i_s=24 A	1.59 T
middle of stator yoke for i_m=72 A, i_s=24 A	1.1 T
middle of rotor yoke for i_m=72 A, i_s=24 A	1.4 T

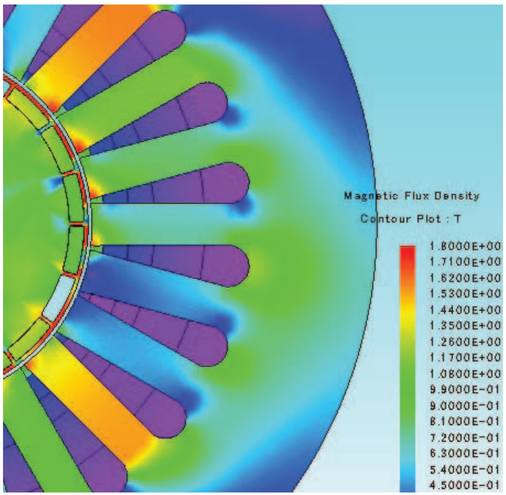

Fig. 9 Flux density in the rotor obtained by the transient simulation for i_m=72 A and i_s=6 A at the moment of worst case direction angle error. The imbalance flux densities (close to saturation) of 4 out of 24 rotor teeth, which are passing over the first segment of the magnet of each pole (for the counter clock rototing rotor) occures 12 times per revolution (in every second tooth) for a brief moment.

V. EFFECT OF STATOR SKEW

In order to further decrease the error angle and torque ripple the effect of the stator skew has been studied. The series of 2D simulations of machine sections every 0.5° have been performed for effective emulation of the skew from 0 to 16°. Fig. 10 shows mean torque, peak torque ripple, peak force angle and peak force amplitude errors. From (a), it can be observed that mean torque does not decrease with the skew. In (b) to (c), it is seen that the skew is very effective in eliminating high frequency torque ripple and force errors. In particular 24th harmonic is significantly decreased in force direction angle error, force amplitude error and in torque ripple (cogging torque).

Fig. 11 shows force amplitude and force angle waveforms with and without skew for three different current conditions. Without skew, 12 peaks are seen, however, the 12 peaks are cancelled with the 15° skew, and that corresponds one slot pitch. Effectiveness of the skew is seen.

Fig. 12 shows spectrum of force error angle $|\Phi_e|$ for three current conditions. The 24th component is quite high without skew, however, this component is significantly decreased with the 15° skew. Interestingly the 4th harmonic can slightly increase in the force direction angle error.

Fig. 13 shows spectrum of force error amplitude $|F_e|$ for three current conditions. With motor current 24th component is high, but this can be eliminated by the skew.

Fig. 14 shows spectrum of torque ripple $|T_e|$ for three current conditions. The 24th component is also decreased by the skew. The 4th harmonic appears in the torque ripple when high suspension currents are present. From Fig. 12 to 14, the 12th harmonic of the torque ripple is decreased more when compared with the decrease of the force errors. The 12th harmonic also appears in all studied error signals only when the motor current is present.

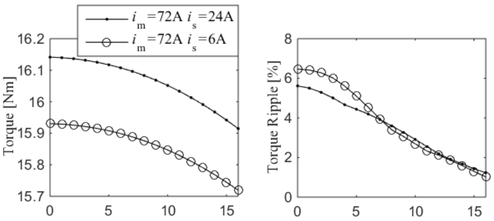

(a) Mean Torque (b) Peak Torque Ripple

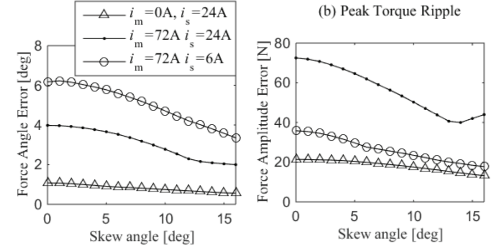

(c) Peak Force Angle Error (d) Peak Force Amplitude Error

Fig. 10 Effect of stator skew at Ω=30000 r/min.

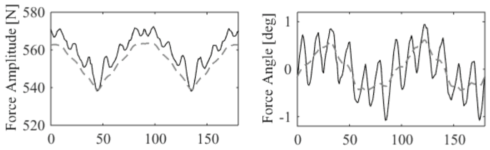

(a) For amplitudes i_m=0 A, i_s=24 A (b) For amplitudes i_m=0 A, i_s=24 A

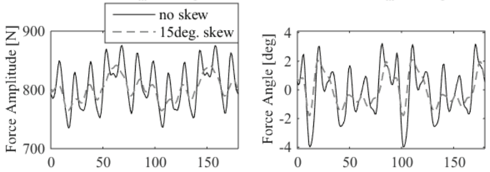

(c) For amplitudes i_m=72 A, i_s=24 A (d) For amplitudes i_m=72 A, i_s=24 A

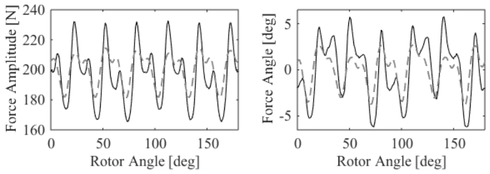

(e) For amplitudes i_m=72 A, i_s=6 A (f) For amplitudes i_m=72 A, i_s=6 A

Fig. 11 Effect of 15° stator skew at Ω=30000 r/min.

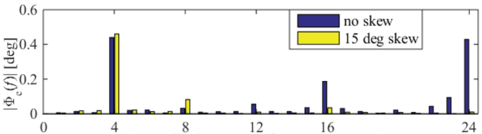

(a) Amplitude spectrum for i_m=0 A, i_s=24 A

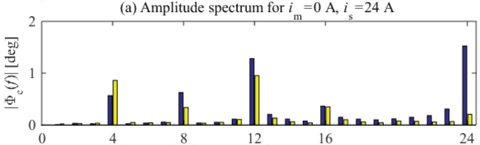

(b) Amplitude spectrum for i_m=72 A, i_s=24 A

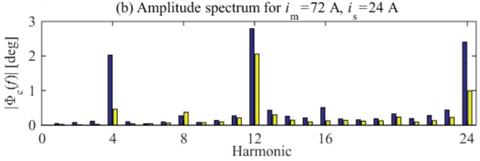

(c) Amplitude spectrum for i_m=72 A, i_s=6 A

Fig. 12 Amplitude spectrum of force error angle at Ω=30000 r/min.

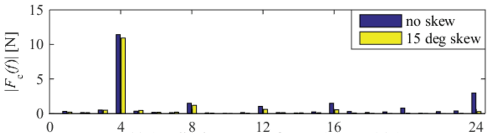

(a) Amplitude spectrum for i_m=0 A, i_s=24 A

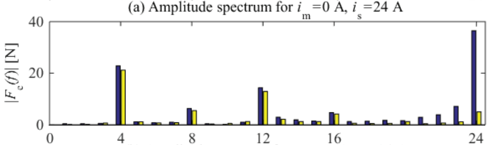

(b) Amplitude spectrum for i_m=72 A, i_s=24 A

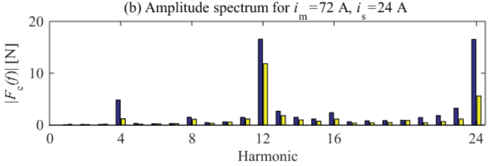

(c) Amplitude spectrum for i_m=72 A, i_s=6 A

Fig. 13 Amplitude spectrum of force error amplitude at Ω=30000 r/min.

VI. ESTIMATION OF LOSSES

The total iron loss calculation results, for the cases (b) and (d) according to Fig. 14, have been listed in Table III. The computations have been carried out for only quadrature current present for first 127 harmonics. The nominal torque conditions and accurate 2D geometry have been investigated. The rotor losses increase for the maximum suspension load and nominal torque when compared to the case with only nominal torque production.

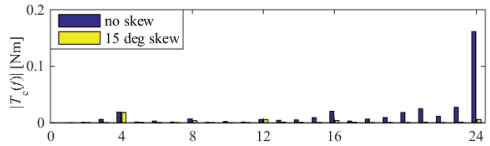

(a) Amplitude spectrum for i_m=0 A, i_s=24 A

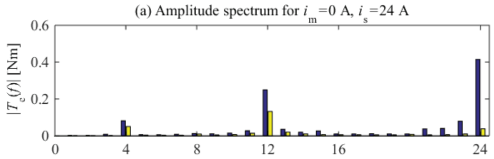

(b) Amplitude spectrum for i_m=72 A, i_s=24 A

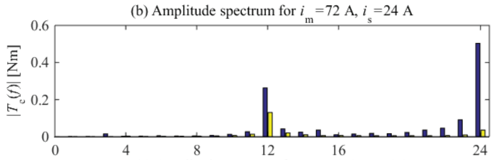

(c) Amplitude spectrum for i_m=72 A, i_s=6 A

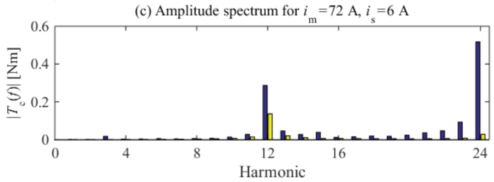

(d) Amplitude spectrum for i_m=72 A, i_s=0 A

Fig. 14 Amplitude spectrum of torque ripple at Ω=30000 r/min.

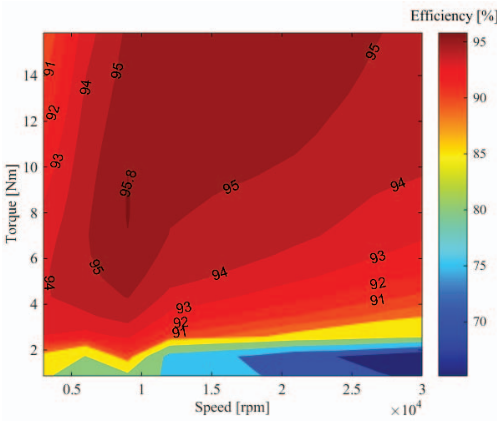

Fig. 15 Efficiency map of the bearingles 50kW unit without the suspension current. The loss calculation included windage losses, resistive losses, additional losses, and iron losses computed based on accurate geometry 2D model and using 32 harmonics.

In normal operation only the fraction of the suspension capacity is needed to overcome the gravity and the suspension losses are insignificant in a static steady state situation without eccentricity.

For the skew present in the stator the total calculated iron losses increase by 18 W and 6 W in the case (d) and (b) as presented in Table III, respectively.

For the sinusoidal currents the stator phase winding resistive losses are in the case (d) 234 W and in the case (b) 312 W. The losses caused by PWM have been neglected in this computation.

For high-speed machines additional windage losses can be estimated by summing losses associated with a resistive drag of the rotating cylinders of different diameters with corresponding airgaps as given by Saari [6] and by Pyrhonen et al. [4]. For example, we use the ICAO's ISA or ISO 13443 reference conditions at 288.15 K (15 °C) and absolute pressure 101.325 kPa in the relative humidity 0 % of air. The windage loss of one 50 kW bearingless motor unit is 73 W at 30000 r/min. The total windage loss of the exemplary configuration at nominal speed as in Fig. 2 is 185 W.

The losses in the segmented and embedded magnets are neglected in this study. Instead we assume additional losses equal to 0.3 % of the output power.

The sum of estimated losses in the machine comprises total iron losses, the stator resistive losses in all the phases, windage losses and additional losses. When including all these loss components the estimated efficiencies for the case (d) and (b) from Table III are 93.88 % and 90.75 %. In the actual operations, high radial force is not necessary, thus, efficiency may be close to the case (d).

In order to obtain a complete efficiency map of the single 50 kW unit multiple FEM iron loss calculations are performed for first 32 harmonics where rotor makes one full revolution at different speed and torque values. The resulting iron losses, windage losses, resistive losses and additional losses are summed up and the efficiency map presented in Fig. 15 is built.

The efficiencies of the studied design could be further improved (without increasing the stator outer diameter) by incorporating an efficient water or oil cooling, increasing the design stator current density, decreasing the slot area, increasing the tooth width and increasing height of the stator yoke. In [3] the comprehensive discussion on loss computation in the surface PM bearingless motor with a carbon fiber composite bandage and a stator water cooling can be found.

TABLE III
LOSS CALCULATION OF BURIED-TYPE IPM SINGLE BEARINGLESS UNIT FOR FIRST 127 HARMONICS

Power factor	0.95
Case (d): Losses for nominal torque and no suspension force	
- Joule loss: rotor, stator	66 W, 1012 W
- Iron loss: rotor, stator	70 W, 1332 W
- Hysteresis loss: rotor, stator	4 W, 321 W
Total calculated iron loss	2805 W
Case (b): Losses for nominal torque and nominal (max) force	
- Joule loss: rotor, stator	720 W, 1202 W
- Iron loss: rotor, stator	733 W, 1548 W
- Hysteresis loss: rotor, stator	14 W, 346 W
Total calculated iron loss	4562 W

VII. CONCLUSIONS AND FUTURE WORK

In this paper, a bearingless motor with an output power as high as 100kW, which is the highest power in the authors' best knowledge, has been designed and analyzed in computer analysis.

The force direction angle error and force amplitude error increase with the increase of the motor current, irregular flux densities close to the saturation in some teeth and absolute torque ripple. In the contrary, the presence of the high suspension current slightly decreases the observed torque ripple 24th harmonic. The biggest error angle appears for small amplitude of the suspension currents and high motor currents when 4th, 12th and 24th harmonics become dominant. The 12th harmonic in the suspension force error angle and amplitude appears only in the presence of the motor currents. It should be noted that for the maximum motor current amplitudes the peak flux densities close to the saturation appear only momentarily in some of the teeth.

In general the harmonic content in the direction angle error significantly depends on the amplitude of the motor currents. This requires some design tradeoffs, which is different from motors with lower tangential stress and lower peak flux densities. In the bearingless motors with the more relaxed magnetic circuit designs and lower peak flux densities the stator and rotor diameters, iron volume and rotor weight would considerably increase. The total iron loss would increase because of longer flux paths and the maximum speed would be more limited by the increased stress in the lamination bridges over the magnets.

In the future work, a rotor geometry, bridge structure and magnet shape would need further consideration.

The experimental investigation and the design of the machines with higher airgaps will be conducted.

ACKNOWLEDGMENT

The work has been carried out during the research visit of P.J. and R.P.J. at the Tokyo Institute of Technology. The visit has been co-funded by International Mobility Grant from LUT School of Technology and Academy of Finland No. 270012 and No. 273489. R.P.J and P.J would like to express their thanks to PhD K. Kiyota for sharing his expertise in finite element analysis tools and to Professor J. Pyrhonen for his valuable motor design suggestions.

REFERENCES

[1] Redemann, Ch., et al. "30 kW Bearingless Canned Motor Pump on the Test Bed," 7th Int. Symp. on Magnetic Bearings, Zurich, Switzerland, pp. 189–194, 2000.

[2] Munteanu, G., et al. "Development and test of high-speed bearingless PM synchronous machines," *Elektrotechnik & Informationstechnik*, 128/3: 75–80, 2011.

[3] Munteanu, G., et al. "Loss measurement of a 40 kW high-speed bearingless PM synchronous motor," IEEE Energy Conversion Congress and Exposition (ECCE), 2011.

[4] J. Pyrhonen, T. Jokinen, V. Hrabovcova, *Design of rotating electrical machines*, John Wiley & Sons, 2nd ed., Chichester, U.K., 2014.

[5] J.R. Hendershot and T.J.E. Miller, *Design of Brushless Permanent-Magnet Machines*, Motor Design Books LLC, 2nd ed., 2010.

[6] A. Chiba, T. Fukao, O. Ichikawa, M. Oshima, M. Takemoto, and D.G. Dorrell, "Magnetic Bearings and Bearingless Drives", Amsterdam, The Netherlands: Elesevier, 2005.

[7] Saari, J., *Thermal Modelling of High-Speed Induction Machines*, Electrical Engineering Series No. 82. Acta Polytechnica Scandinavica, Helsinki University of Technology, Finland, 1995.

Publication III

Jaatinen, P., Jastrzebski, R. P., Pyrhönen, O., and Chiba, A.
Improving of bearingless 6-slot IPM motor radial force characteristics using rotor skew

Reprinted with permission from
Proceedings of the IEEE International Electric Machines and Drives Conference (IEMDC), Miami, FL, USA
pp. 1–7, 2017
©2017, IEEE

Improving of bearingless 6-slot IPM motor radial force characteristics using rotor skew

Pekko Jaatinen[1], Rafal P. Jastrzebski[1], Olli Pyrhönen[1], Akira Chiba[2]
[1]Lappeenranta University of Technology; LUT Electrical Engineering, Lappeenranta, Finland
[2]Tokyo Institute of Technology; Electrical and Electronic Engineering, Tokyo, Japan

***Abstract*—Bearingless machine technology is well-suited for high-speed applications as it removes the mechanical friction by supporting the rotor with electromagnetic force. For electrical machine, which is operating in high-speed region, a short rotor length is beneficial to avoid the rotor vibration caused by structural properties of long rotor. A 6-slot tooth-coil wound bearingless machine is well suited for high-speed applications as it shortens the rotor length compared to more traditional distributed winding configuration. Drawback of the tooth-coil wound machine is the higher space harmonic content which decrease the radial force performance characteristics including ripple and disturbance forces. In this paper, the rotor skew is introduced to improve the radial force characteristics of IPM bearingless machine.**

Keywords— bearingless motor*; *skew*; *tooth-coil; PM motor; magnetic levitation

I. INTRODUCTION

Bearingless motor construction is very attractive for a high-speed applications as it reduces the overall length of the machine compared to traditional magnetic bearing configurations [1]. High operational speeds can be achieved as mechanical bearings are not used, hence the rotor is levitated with magnetic force produced by the additional stator windings. Applications which are oil-free such a pressurized air compressors will benefit from bearing technology where oil-based lubricants are not needed. For example, purity classes of the pressurized air are described in ISO 8573 standard. In this standard, the amount of the oil in pressurized air is divided to different classes by how much oil is concentrated in air mg/mm^3 [2].

In high-speed applications i.e. air compressors, a small axial length to rotor diameter ratio (LD ratio) is beneficial as the rigid rotor is less sensitive to vibrations. It is preferable to stay in subcritical rotational speed as it eases the control design and operation in the working speed. Motor winding arrangement has a significant part to LD ratio. Previously, tooth-coil winding arrangement have been compared to more traditional distributed winding configuration [3]. Bearingless machine with distributed and tooth-coil windings are compared in Fig. 1. It is very evident that tooth-coil structure reduced the LD ratio significantly. Additionally shorter rotor structure reduces weight of the rotor and the foot print of the overall machine. Drawback of the tooth-coil winding structure is the higher space harmonic content which reduces radial force characteristics by increasing the radial force ripple and force error angle [1]. Applying skew in the motor is well known method to improve torque ripple in surface and interior permanent magnet machine by reducing the effect of the harmonics [6]-[8]. This far, the skew has been used in bearingless machine to reduce the torque ripple [5]. In this paper, the feasibility of applying skew in the interior permanent magnet (IPM) bearingless machine to improve radial force characteristics is evaluated. Rotor skew is considered as the most suitable choice as the magnets will be segmented also axially to reduce the eddy current losses. It also helps the winding work as the stator is not skewed. Continuous skew is used as a reference in analysis. Using rotor skew to improve radial force characteristics is proposed and analyzed.

II. RESEARCH PROBLEM

A. Descripion of machine under investigation

Bearingless motor under investigation is constructed with two separated winding layers for producing torque and radial force. Bearingless machine consist of two motor units to produce torque and radial force together with axial bearing to create force in axial direction. With this configuration rotor position can be controlled in 5-degrees of freedom. Fig. 1a shows a rotor structure of laboratory prototype machine with distributed windings. Machine under analysis with tooth-coil windings is shown in Fig. 1b. Cross-sectional view of the rotor and stator is illustrated in Fig. 2 Same IPM rotor structure is used in both machines. Machine parameters can be found in Table 1. Minimum winding construction to reduced iron losses for high-speed bearingless machine is 2-pole and 4-pole windings [3]. In this case the motor windings are 4-pole and the levitation windings are 2-pole. This structure was chosen to have the smaller radial force ripple compared to the case where levitation winding is 4-pole [9].

B. Reduction of machine axial length

Cross-sectional view of the both machines and stator stacks can be found in Fig. 1-2. Using distributed winding construction increases the total machine length hence the end windings are long compared to the stator stack. Long machine structure lowers the bending mode frequencies of the rotor. This sets extra demands to control the machine when compared to the rigid rotor. By using the tooth-coil winding construction, axial length can be reduced significantly, which can be seen in Fig. 1. The LD ratio of distributed wound machine is 7.369 and for the tooth-coil wound machine it is 5.392. By using the

---

The authors would like to express their gratitude to the Academy of Finland, grant No. 270012 and No. 304071, for financial support.

978-1-5090-4281-4/17/$31.00 ©2017 IEEE

tooth-coil wound machine the LD ratio is reduced 26.8 percent. Reduced axial length also decreases the weight of the rotor. This reduction of mass from the rotor decreases the power needed to levitate the rotor in a steady-state situation.

C. *Error angle of radial force*

In the ideal case, the radial force produced by levitation windings would be ripple free with no external disturbances. However, in reality the produced force is affected by the space harmonics caused by windings together with shape of stator and rotor dimensions. The harmonic content generates ripple to the radial force. Additionally, unwanted disturbance force vector is appearing from ±90 degrees from target force vector. Effect of the harmonics can be seen in Fig. 3a, where radial force is generated in x-direction. There is also a y-axis disturbance force vector present. Angle between the target and the disturbance force vector is called the force error angle. This error angle and related force vectors are illustrated in Fig. 3b. If the error angle is greater than 17 degrees the phase margin of the closed-loop system is reaching to -180 dB which leads to unstable system [1]. From the same analysis, we can find that less than 5-degree error angle is not significantly affecting to the phase margin.

The error angle should be minimized in the machine design phase. After manufacturing, the force error angle can get worse because the delays in the system. Harmonic content in the air-gap can be optimized for example by rotor design [3], where

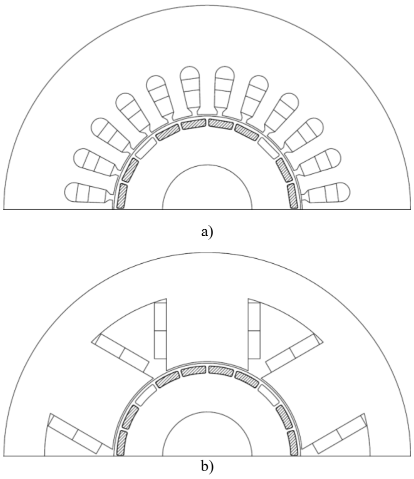
a)

b)

Fig. 2. Cross-section view of the rotor and stator from the end point of the rotor. Upper drawing (a), shows a distibuted wound machine. Torque producing windings are two-layers short pitched. Lower drawing (b), shows a tooth-coil wound machine. Both machines uses the same rotor stucture with embedded magnets.

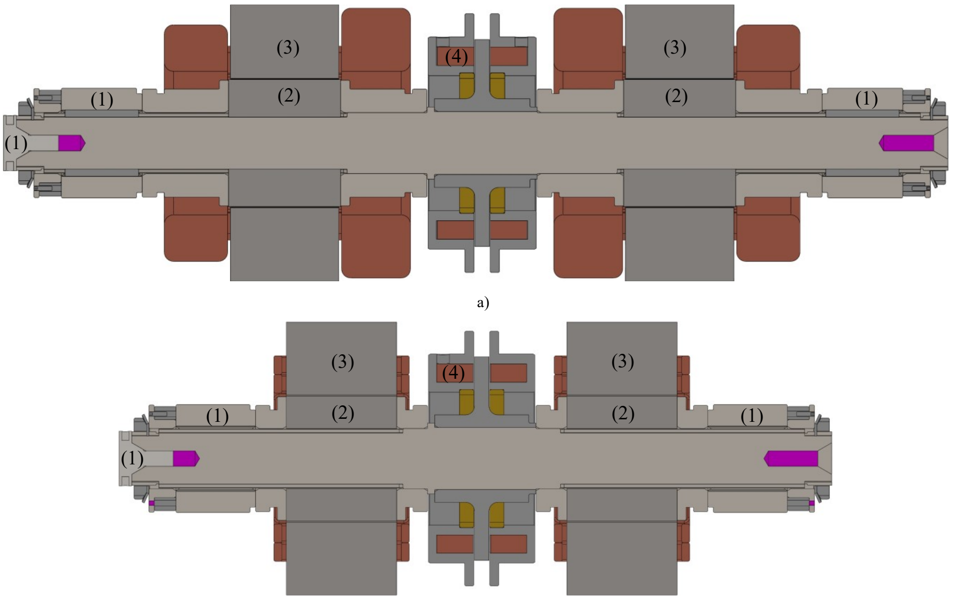

1. Cross-section view of the distibuted a) and tooth-coil b) wound bearingless machine. Componets in the rotor system are; (1) rotor position measurement surface in radial and axial, (2) rotor active part with embedded magnets, (3) stator of the motor unit and (4) axial bearing to control the rotor position in axial direction.

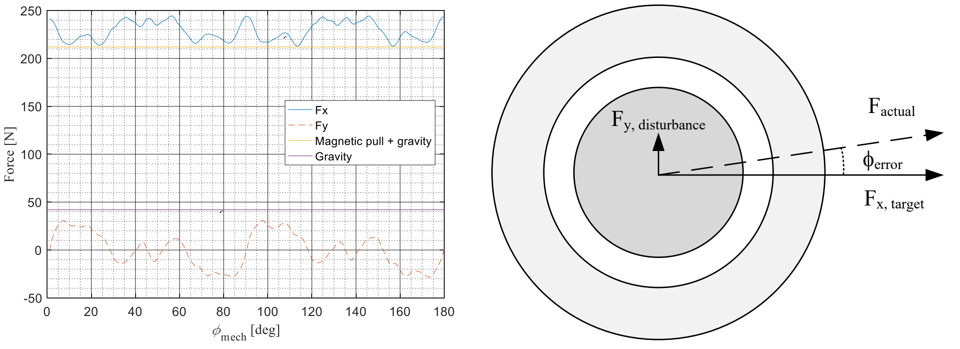

a) b)

Fig. 3. Produced radial force in *x*-direction with unwanted force in *y*-dircetion, $I_{\mathrm{levitation}} = 8$ A rms (a). Illustration of force error angle (b).

by varying the angle of magnets the minimum point is searched. Same method is used in the test case. Maximum error angle between the forces is presented in Fig. 3a for the tooth-coil configuration. Value of the error angle is 7.8 degrees. This means that further optimization is necessary to guarantee the controllability of bearingless motor.

III. STEP SKEW

To improve the radial force characteristics of the tooth-coil wound machine, several step skew configurations in function of skew angle are compared. Step skew means the rotor skew is axially divided to steps. These steps are positioned in different angles so that they create a discrete skew. Fig. 4 shows a practical implementation of 3 and 5 step rotor skew. Similar structure has been used in [6], [7]. Step skew from 2 to 5 steps and continuous skew are compared how they affect to torque and force characteristics of the machine. Continuous skew is used as a reference and it is practically implemented as a stator skew.

A. Calculating the skew

Effect of the skew were simulated by 2-dimensional FEM using a commercial software JMAG 2015.1. Rotor initial angle were changed from 0 to ± 30 degrees for generating cut-planes to calculate the effect of the skew. Rotor initial angle were changed with 0.5 degree steps (Fig. 5). In every simulation rotor were rotated 180 degrees to get torque and force curve in current operation point. Effect of the continuous skew were calculated taking an average value from torque or force vector in range of skew angle. For example, vector *f* as in (1), is describing force during simulation when rotor is rotated 0 to 180 mechanical degrees,

$$f = \left[f_1 \quad f_2 \quad \cdots \quad f_{j-1} \quad f_j \right], \tag{1}$$

where *j* is the rotated rotor angle. Continuous skew is calculated by

$$\frac{1}{2n+1}\sum_{k=-n}^{n}\left(f\right)_k, \tag{2}$$

where *n* is the rotor initial angle from zero degrees to describe the skew and *f* is the force or torque vector. The effect of the step skews was calculated with (3-6). These average equations are applied to calculate every even skew angle *n,* from 0 to +-30 degrees.

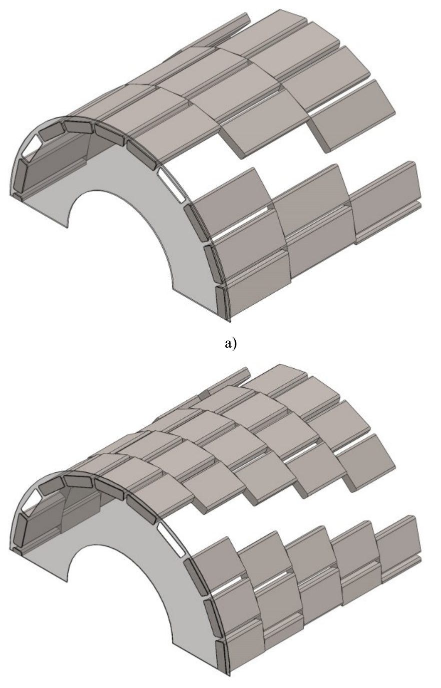

a)

b)

Fig. 4. Step skew in IPM type rotor. To simplify the figure rotor lamination material is only shown in front of the active part. (a-b) Shows a rotor active part with 3 and 5 step skew, respecitvely.

$$\frac{1}{2}\left(f_{-n}+f_{n}\right) \tag{3}$$

$$\frac{1}{3}\left(f_{-n}+f_{0}+f_{n}\right) \tag{4}$$

$$\frac{1}{4}\left(f_{-n}+f_{-\frac{n}{2}}+f_{\frac{n}{2}}+f_{n}\right) \tag{5}$$

$$\frac{1}{5}\left(f_{-n}+f_{-\frac{n}{2}}+f_{0}+f_{\frac{n}{2}}+f_{n}\right) \tag{6}$$

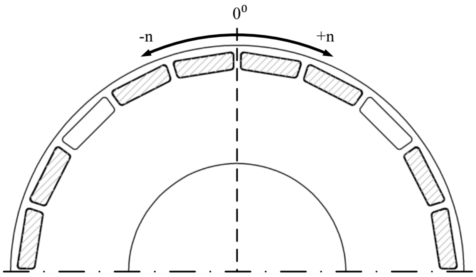

Fig. 5. In 2d FEM analysis, the initial angle of the rotor is changed from -30 to 30 degrees with 0.5 degree steps.

IV. SIMULATION RESULTS

Effect of the skew is presented based on the results obtained from 2D-FEM and analytical equations. Five different cases are plotted with two different conditions. These cases will plot torque ripple, reduction of average torque, force ripple, reduction of average force and force error angle in function of skew angle. Each of five cases is studied for two different conditions: (a) and (b), which are presented in figures. Condition (a) shows only generated torque or force. Condition (b) shows a rated torque together with the maximum force at the same time. Condition (b) can be considered as a worst-case scenario where full radial force is applied under full load of the motor. Skew angle is plotted till 60 degrees, which is the slot pitch angle in the tooth-coil machine.

A. Results of torque production

Torque ripple is presented in Fig. 6 and it can be seen that continuous skew provides the best reduction in function of skew angle. As motor is more saturated in full-load condition torque ripple is increased which is seen in Fig. 6b. The step skew is effective to reduce torque ripple only till a certain point. As an example, in the case of 2-step skew after 26-degree skew angle the torque ripple is amplified. It is clear that this is the limiting factor of small step skew. Applying continuous skew provides smallest reduction of average torque and average force as a function of skew angle (Fig. 7).

B. Results of force production

Force ripple is presented in Fig. 8a with only force generating condition and it can be noted that the skew is not very effective until 22 degrees. With full-load condition, force ripple reduction is in the same range but due to saturation effects, average force ripple have been increased eight percent (Fig. 8b). Reduction of the average force is following the same pattern as torque curve as seen in Fig 9. However, it seems that less force is lost during the full-load condition. In full-load condition the produced average force is also increased which is the reason of smaller force reduction.

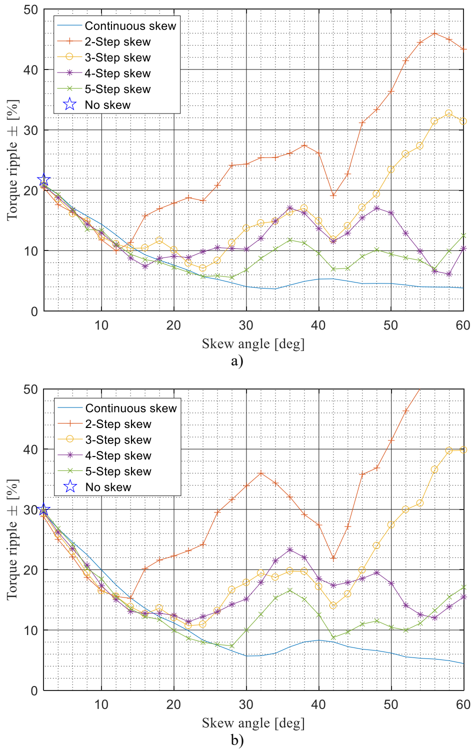

a)

b)

Fig. 6. Torque ripple at the nominal point as a function of skew angle with rated I_{motor} = 8.4 A rms in motor windings and $I_{levitation}$ = 0 A rms in suspension windings (a). Torque ripple with rated I_{motor} = 8.4 A rms in motor winding and maximum $I_{levitation}$ = 8 A rms in suspension windings (b).

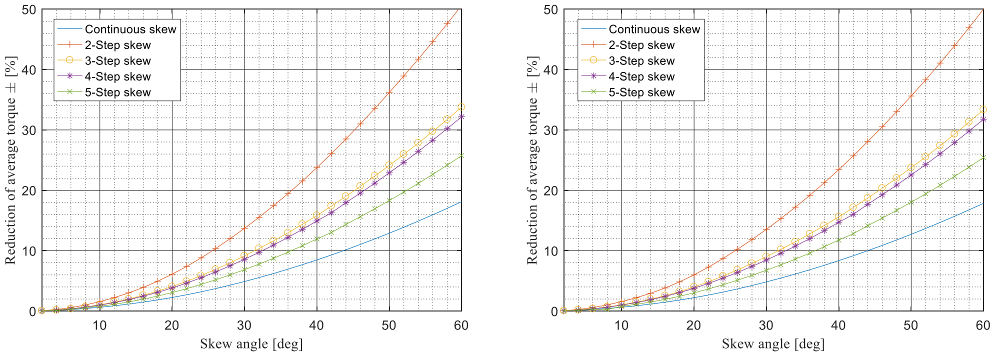

a) b)

Fig. 7. Torque reduction at nominal point I_{motor} = 8.4 A rms as a function of skew angle with no current in suspension windings $I_{levitaion}$ = 0 A rms (a) and maximum current $I_{levitaition}$ = 8 A rms in suspension windings (b).

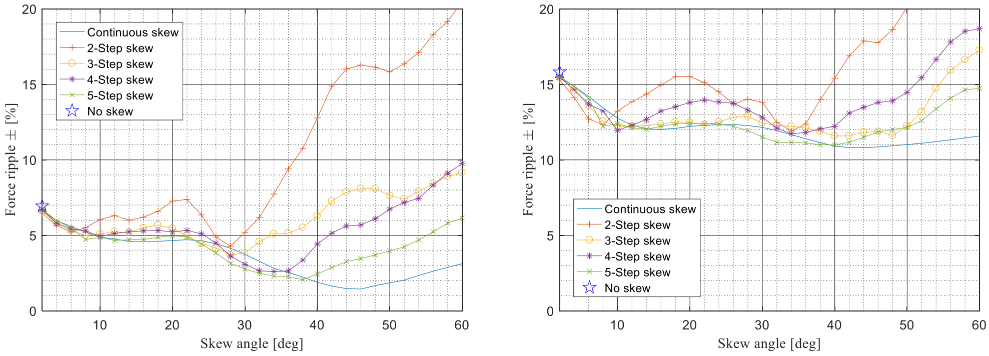

a) b)

Fig. 8. Maximum force ripple $I_{levitaion}$ = 8 A rms as a function of skew angle with no current I_{motor} = 0 A in motor windings (a) and nominal current I_{motor} = 8.4 A rms in motor windings (b).

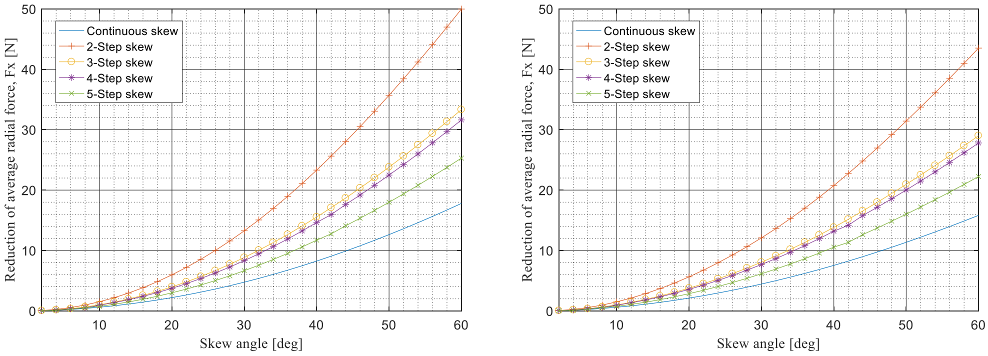

a) b)

Fig. 9. Radial force reduction at maximum force $I_{levitation}$ = 8 A as a function of skew angle with no current I_{motor} = 0 A in motor windings (a) and nominal current I_{motor} = 8.4 A in motor windings (b).

C. *Results of force error angle*

Force error angle is analyzed by generating radial force in *x*-direction and determining the angle between *x*-axis force and disturbance force in *y*-axis. Condition where only suspension current is present is shown in Fig. 10a. The skew angle is starting to be effective not until 24 degrees. In full-load condition the force error angle is over targeted maximum of 5 degrees. Error angle is still acceptable for the worst-case situation, i.e. it is still far from unstable point when 30-degree skew angle is applied. Applying 30-degree skew is a half of the one slot pitch.

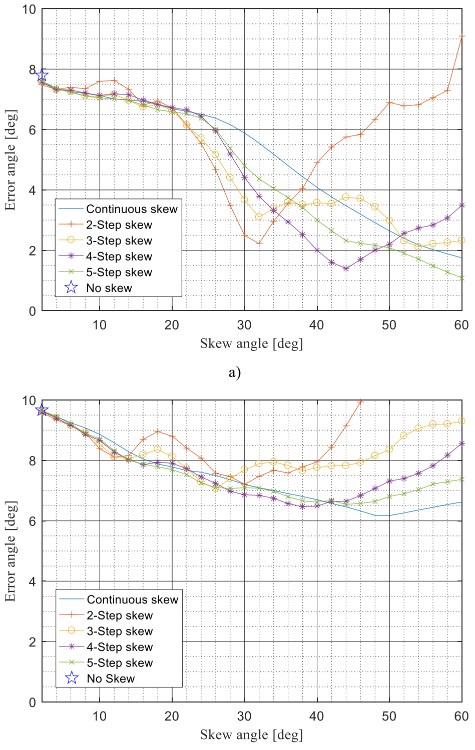

a)

b)

Fig. 10. Force error angle at maximum radial force $I_{levitaion}$ = 8 A as a function of skew angle with no current I_{motor} = 0 A in motor windings (a) and nominal current I_{motor} = 8 A in motor windings (b).

TABLE I. MOTOR PARAMETERS

Symbol	Parameters		
	Parameter	***Distributed***	***Tooth-coil***
P	Output power per motor unit, kw	5 kW	5 kW
n_n	Rated speed, r/min	30000	30000
T_n	Rated torque, Nm	1.59	1.59
Q_s	Number of stator slots	24	6
p	Number of poles	4	4
U_m	Voltage in motor widings, V	400	400
U_l	Voltage in levitation winding, V	400	400
I_m	Current in motor windings, A	8.4	8.4
I_l	Maximum current in levitation winding, A	8	8
D_s	Stator outer diameter, mm	150	150
D_r	Rotor outer diamteer, mm	70	70
δ	Air gap length, mm	0.6	0.6
l	Stator stack length, mm	60	61
B_r	Permanent magnet remanence, T	1.24	1.24
	Lamination material	NO20	NO20

V. CONCLUSIONS

In this paper, aspects of tooth-coil wound bearingless machine for high-speed applications are considered. Short rotor structure permits to operate in high-speed region with subcritical rotor. However, due to higher space harmonic content in the tooth-coil wound machine, the radial force production performance is decreased when considering radial force ripple and force error angle. To improve radial force production performance, stator and rotor skew have been analyzed. Results shows that by applying skew angle of 30 to 32 degrees the error angle can be decrease in acceptable level when using 2 or 3-step skew. In the worst-case scenario when the full radial force is provided under nominal loading of the motor, force error angle is over target value but still in the acceptable region. Rotor skew divided in 3-steps provides better overall performance thus it reduces also the torque ripple when 30 degrees skew angle is applied. Naturally the application dictates the need of torque ripple reduction. In the case of air-compressor application the torque ripple reduction is not as important because it is filtered by the inertia of rotor system. It can be concluded that skew can be used to improve torque and radial force ripple with force error angle. However, the average torque and force production is reduced in function of the skew angle. Applying rotor skew in tooth-coil wound machine will permit to use this kind of machine structure in high-speed applications.

REFERENCES

[1] A. Chiba, T. Fukao, O. Ichikawa, M. Oshima, M. Takemo, and D.G. Dorrell, “Magnetic bearings and bearingless drive”, Amsterdam, The Netherlands: Elsevier, 2005

[2] Compressed air – Part 1: Contaminants and purity classes, ISO 8573-1, 2010, pp.

[3] P. Jaatinen, R. P. Jastrzebski, O. Pyrhönen, "Comparison of winding arrangements of a high-speed interior permanent magnet bearingless machine," 2016 19th International Conference on Electrical Machines and Systems, Chiba, Japan, 2016, pp. 962-967.

[4] P. Ponomarev, Y. Alexandrova, I. Petrov, P. Lindh, E. Lomonova and J. Pyrhönen, "Inductance calculation of tooth-coil permanent-magnet synchronous machines," in IEEE Transactions on Industrial Electronics, vol. 61, no. 11, pp. 5966-5973, Nov. 2014.

[5] Y. Koshi, M. Ooshima, M. Nasir Uddin and H. Kitada, "Improvement of rotational torque and suspension force by winding arrangement in a bearingless motor drive for a solid-liquid separator," IEEE International Electric Machines & Drives Conference, Niagara Falls, ON, 2011, pp. 1415-1420.

[6] W. Zhao, T. A. Lipo and B. I. Kwon, "Material-efficient permanent-magnet shape for torque pulsation minimization in SPM motors for automotive applications," in IEEE Transactions on Industrial Electronics, vol. 61, no. 10, pp. 5779-5787, Oct. 2014

[7] X. Ge, Z. Q. Zhu, G. Kemp, D. Moule and C. Williams, "Optimal step-skew methods for cogging torque reduction accounting for three-dimensional effect of interior permanent magnet machines," in IEEE Transactions on Energy Conversion, vol. 32, no. 1, pp. 222-232, March 2017.

[8] G. Ombach and J. Junak, "Torque ripple optimization of skewed IPM motor for field weakening operation," International Conference on Electrical Machines and Systems, Beijing, 2011, pp. 1-7.

[9] T. Matsuzaki, M. Takemoto, S. Ogasawara, S. Ota, K. Oi and D. Matsuhashi, "Operational characteristics of an IPM-type bearingless motor with 2-pole motor windings and 4-pole suspension windings," IEEE Energy Conversion Congress and Exposition, Montreal, QC, 2015, pp. 3886-3894.

Publication IV

Jastrzebski, R. P., Jaatinen, P., Chiba, A., and Pyrhönen, O.

Design optimization of permanent magnet bearingless motor using differential evolution

Reprinted with permission from
Proceedings the of IEEE Energy Conversion Congress and Expo (ECCE), Portland, OR, USA
pp. 2327–2334, 2018
©2018, IEEE

Design Optimization of Permanent Magnet Bearingless Motor Using Differential Evolution

Rafal P. Jastrzebski
LUT Electrical Engineering
Lappeenranta University of Technology
Lappeenranta, Finland
Rafal.Jastrzebski@lut.fi

Pekko Jaatinen
LUT Electrical Engineering
Lappeenranta University of Technology
Lappeenranta, Finland
Pekko.Jaatinen@lut.fi

Olli Pyrhönen
LUT Electrical Engineering
Lappeenranta University of Technology
Lappeenranta, Finland
Olli.Pyrhönen @lut.fi

Akira Chiba
Electrical and Electronic Engineering
Tokyo Institute of Technology
Tokyo, Japan
chiba@ee.e.titech.ac.jp

Abstract— **Bearingless motors combine torque generation and suspension force capabilities into one electromagnetic actuator. However, design optimization of bearingless motors is more complex than with traditional motor structures. The combined levitation and motoring performance cannot be quickly evaluated by using Computer Aided Design (CAD) tools applied in traditional motor designs. This work proposes a bearingless motor design chain. The initial dimensions of the test case motor are iteratively derived. The levitation performance is verified by using a lumped parameter model. The fine tuning of the rotor geometry is carried out by using the Finite Element Method (FEM). The objectives for the FEM optimization are a minimum torque ripple, minimum levitation force variations, and maximum torque and force capacities. Finally, experimental force angle measurements of a manufactured test case machine with a unique method are provided. Application of differential evolution is presented and discussed in both analytical and in FEM design steps.**

Keywords — genetic algorithm, differential evolution, bearingless motor, electromagnetic design, magnetic levitation, design optimization, force measurement.

I. INTRODUCTION

Magnetically levitated rotors have been applied for very demanding and special applications in place of traditional mechanical and oil-film bearing solutions. In such applications as pumps, fans, turbines, and compressors, high-speed magnetically levitated rotors have commonly employed active magnetic bearings (AMBs). The AMBs allow very low friction without oil, but the system suffers from increased overall complexity, additional cost, and a longer rotor. The bearingless motors combine the motor/generator and the magnetic levitation functionality into a single actuator. This reduces component count, machine footprint, rotor length, and cost. Additionally, all benefits of active control and measurement system inherent in AMBs, such as active vibration damping, monitoring, and diagnostics capabilities, are available. Admittedly, the machine design becomes more challenging than for separate motor and AMBs. This, in particular, has been limiting the applications to lower power machines.

Analytical CAD software tools for motor/generator optimization have been assisting engineers in initial sizing of the machines and in preliminary optimization of the design features for a few decades already [1]. The examples include a variety of academic and open code design methods, such as Mathcad®-based programs [2] and complex commercial tools, for example, SPEED™ software [3], [2]. Similarly, the AMB design can be facilitated with analytical design automation tools [4]. However, an increase in the popularity of bearingless motors is impeded by the fact that their levitation performance [5] cannot be evaluated straightforwardly in the design phase by using the tools currently available. Nowadays, finite element method (FEM) tools allow accurate prediction of torque ripple, efficiency, and effective fine-tuning of the motor design in different conditions. Nevertheless, the FEM-based design is time consuming. The optimization process requires experience and appropriate initial sizing and initial geometry of the machine. For bearingless motors, the optimization objectives are different than in the case of regular motor designs. For a radial bearingless motor, the design feasibility is determined by how well the magnetic force vector can be controlled in the *x*- and *y*-directions. For example, when controlling the force acting on the rotor in the *x*-direction, also a smaller unwanted force is generated in the *y*-direction. Minimization of variations in the force angle with the angular rotor position, referred to as force error angle, is the major design objective. Other objectives include force capacity and amplitude variations. Different optimization tools can alleviate the time-consuming design process. Genetic algorithms (GA) provide a proven framework for the electromagnetic design of active magnetic bearings [6], [7], control tuning for magnetically levitated systems [8], and permanent magnet (PM) motor designs [9], [10], [11], [12].

This paper presents a design chain for PM type bearingless motors. Custom analytical predesign tools and FEM GA optimization are evaluated. The feasibility of various methods is discussed. Surface PM (SPM) motors and interior PM motors (IPM) with multilayer short-pitch coils are considered. The constrained problem of minimizing magnetic force errors (angle and amplitude variations), maximizing torque and absolute force amplitude, maximizing efficiency, and minimizing torque variations in a PM bearingless motor design is addressed. The proposed design chain comprises an analytical motor predesign part, a levitation verification part, which focuses on the prediction of force variations, and the FEM optimization. The bearingless machine under design consists of two motor/levitation units together with an axial magnetic bearing [13]. With this setup, the rotor position can be controlled in the air gap in 5-degrees-of freedom. Torque is produced with both motor units. A unique force measurement rig is used for the evaluation of the FEM- and analytical-estimated force error angles in the test case IPM bearingless machine.

978-1-4799-7312-5/18/$31.00 ©2018 IEEE

II. ANALYTICAL OPTIMIZATION OF THE MOTOR

The initial dimensioning of the machine can be performed analytically. This significantly reduces the computation and design times of the FEM-based optimization, which is only used for the fine-tuning and final verification of the design performance. The overall flowchart of the proposed optimization chain is shown in Fig. 1. Differential evolution (DE) is applied in the analytical predesign stage and in the FEM optimization.

A. *DE algorithm*

The initial steps in the analytical bearingless machine design are similar to those available for standard electrical machines. Here, the analytical method as in [2] is transcribed into MATLAB® and executed using a differential evolution-based GA framework [14].

First, we select the preliminary design constrains, such as materials, nominal torque, nominal speed, number of slots and poles, and geometry type. The algorithm amends the motor windings with the levitation windings according to the required force capacity. Second, the genetic optimization solves the motor dimensions for optimal efficiency and constrained material volumes.

A DE/best/1/bin DE algorithm is applied as the optimization tool. Das and Suganthan [15] in the survey of different methods point to DE/best/1/bin algorithm (using always the best solution to find search directions and binomial crossover) as the most competitive scheme, regardless the characteristics of the problems. This algorithm reduces the convergence time compared to classical DE scheme. The framework applies the population $\vec{X}_{j,i,g}$ that contains parameter vectors under optimization. Index *j*, refers to amount of the parameters. Index *i*, indicates population length; and *g* refers to number of generation. Initially, parameters of the first generation are randomly created with upper and lower bounds. The mutant vector $\vec{V}_{i,g}$ is created from combination of three different vectors. First, the best suitable vector $\vec{X}_{\mathrm{best},g}$ is selected based on the objective function *f*. Two randomly selected vectors $\vec{X}_{\mathrm{r},g}$ are subtracted and scaled by the scale factor F_j. Traditional DE algorithm uses the scalar scale factor *F*. This method uses the random uniformly distributed scale factor F_j for every parameter.

$$\vec{\mathrm{V}}_{\mathrm{i,g}} = \vec{\mathrm{X}}_{\mathrm{best,g}} + \mathrm{F_j}\big(\vec{\mathrm{X}}_{\mathrm{r1,g}}\text{-}\vec{\mathrm{X}}_{\mathrm{r2,g}}\big) \tag{1}$$

$$F_j = F + 0.001 * (rand(0,1) - 0.5) \tag{2}$$

The trial vector $\vec{U}$ is selected using the cross over (CR) term, which controls DE and a probability to inherit mutant vector properties to the trial vector.

$$\vec{U}_{i,g} = \begin{cases} \vec{V}_{j,i,g} \; if\,(rand(0,1) \leq CR \; or \; j = j_{rand}) \\ \vec{X}_{j,i,g} \; \text{otherwise} \end{cases} \tag{3}$$

$$\vec{X}_{i,g+1} = \vec{U}_{i,g} \quad if \quad f\big(\vec{U}_{i,g}\big) \leq f\big(\vec{X}_{i,g}\big) \quad = \quad \vec{X}_{i,g} \quad if \quad f\big(\vec{U}_{i,g}\big) > f\big(\vec{X}_{i,g}\big) \tag{4}$$

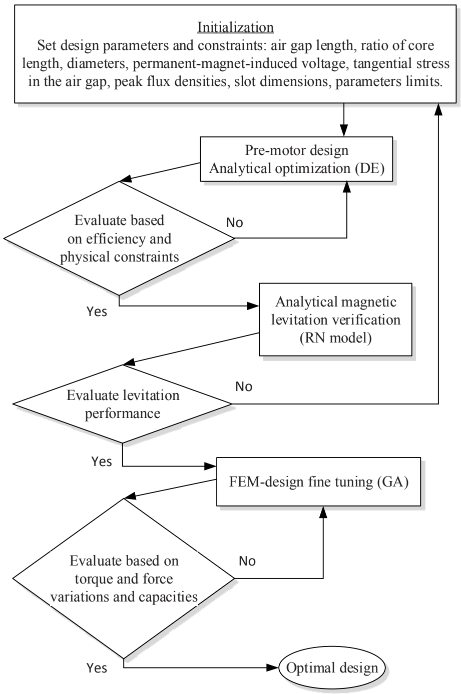
Initialization
Set design parameters and constraints: air gap length, ratio of core length, diameters, permanent-magnet-induced voltage, tangential stress in the air gap, peak flux densities, slot dimensions, parameters limits.
Pre-motor design
Analytical optimization (DE)
Evaluate based on efficiency and physical constraints
No
Yes
Analytical magnetic levitation verification (RN model)
Evaluate levitation performance
No
Yes
FEM-design fine tuning (GA)
Evaluate based on torque and force variations and capacities
No
Yes
Optimal design

Fig. 1. Flowchart of the motor and levitation function optimization chain. Differential evolution (DE) is applied in the preliminary analytical motor design, in analytical magnetic levitation verification using reluctance network (RN) and in the FEM fine-tuning of the rotor geometry.

In the last phase the algorithm selects suitable vector determining whether the trial vector survives to the next generation (or if the target is retained in the population) based on objective function. Objective function uses the mean square error to evaluate the fitness of parameter vectors under optimization.

B. *Evolutionary optimization of motoring function*

The set of design parameters is constrained by the upper and lower limits. The optimized analytical design parameters include air-gap length, ratio of equivalent core (machine) length and air-gap diameter, permanent-magnet-induced voltage, tangential stress in the air gap, peak flux densities in the iron stator (rotor) yokes, peak flux density in the tooth, and slot dimensions. Additionally, the maximum stator and rotor diameters are limited by the mechanical constrains. The motor efficiency without turned-on levitation is directly taken as an objective function. Fig. 2 shows results of optimization of 4-pole 5kW SPM motor. The maximum efficiency is reached by individuals with the permanent-magnet-induced voltage of about 222 V. The red stars in different figures represent the result of the best parameter vector. The optimum cases are for the lowest peak flux densities in the stator yoke but for a wide range of peak flux density values in the rotor yoke (Fig. 3ab). The optimal range of flux densities in the tooth is between 1 T and 1.2 T (Fig. 4).

With maximum efficiency, the maximum values of tangential stresses are reached (Fig. 5). The analytical script can very quickly iterate on hundreds of motor designs for the specified parameter ranges and roughly estimate their efficiency.

The evolutionary optimization speeds up the process of achieving optimal initial dimensions of the potentially most efficient motor for the required torque, speed, and air gap.

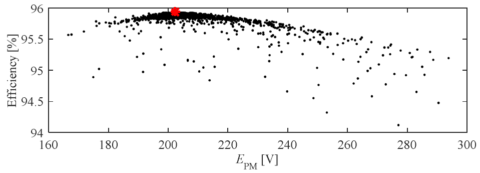

Fig. 2. Analytically estimated efficiency for different design cases as a function of permanent-magnet-induced voltage. The red star indicates the optimal design case from the last generation.

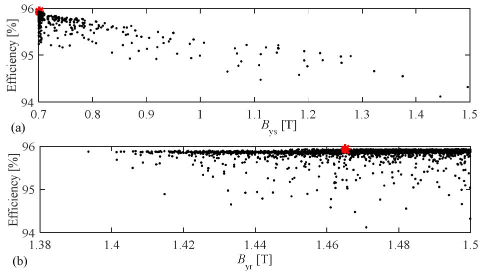

Fig. 3. Analytically estimated efficiency for different design cases as a function of peak flux densities in the stator yoke (a) B_{ys} and the rotor yoke (b) B_{yr}. The red star indicates the optimal design case from the last generation.

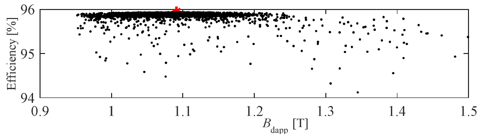

Fig. 4. Analytically estimated efficiency for different design cases as a function of peak flux density in the tooth B_{dapp}. The red star indicates the optimal design.

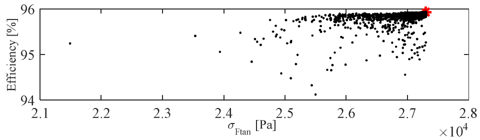

Fig. 5. Analytically estimated efficiency for different design cases as a function of assumed tangential stress σ_{Ftan}. The red star indicates the optimal design case.

III. ANALYTICAL VERIFICATION OF LEVITATION

The motor geometry has to be optimized not only from the torque production and efficiency perspective but also from the viewpoint of magnetic levitation. The required force capacity has to be ensured. The most important objective with respect to the feasibility of controlling the levitation forces is minimization of the force error angle.

A. Force error angle

A single unit of the bearingless motor is assumed to control the rotor radial position in the *xy* coordinate system. The origin of the coordinate is placed at the geometrical center of the rotor. The angle deviation between the desired and the actual force can be computed from the force *x* and *y* vector components

$$\phi_{\text{error}} = \tan^{-1}\frac{f_y}{f_x}. \tag{5}$$

For the rotor rotating about its principal axis of inertia, the force error angle is caused by permeance distribution and the spatial space harmonics of the (magnets and coils) magnetomotive force (MMF) [5], [16], [17]. In practice, force variations and their measurements are also affected by eddy currents, gyroscopic effects, delay of rotor position, and calculation delay of the force command. Minimization of the error angle results in reduced power consumption in the levitation windings [17]. For error angles larger than 15 degrees, damping of the rotor vibrations and levitation are no longer feasible [5].

B. Analytical verification of levitation forces

In this work, the performance characteristic, such as force capacity and force variations, are computed using a simple lumped parameter reluctance network (RN) model. The basic RN is similar to a distributed network [5]. It comprises reluctances of the stator and rotor branches dependent on the geometry, and air gap. The reluctances vary with angular positions. No leakage fluxes are assumed. The reluctances $\Re_j$ of the air gaps and the initial volume reluctances of the iron are

$$\Re_j = \frac{l_j}{\mu_0 \mu_j S_j}, \tag{6}$$

where l_j, μ_j, and S_j are the length, relative permeability, and area of the *j*th element. The air-gap relative permeability is assumed to be one. μ_0 is the relative permeability of vacuum. The generalized equation set for the loop fluxes $\boldsymbol{\Phi}_{\text{ml}}$ and the branch fluxes $\boldsymbol{\Phi}_{\text{m}}$ can be expressed as

$$\boldsymbol{T}\boldsymbol{\Re}(\boldsymbol{\Phi}_{\text{m}})\boldsymbol{T}^{T}\boldsymbol{\Phi}_{\text{ml}} = \boldsymbol{N}\mathbf{i}, \tag{7}$$

where $\boldsymbol{\Re}$, $\boldsymbol{T}$, $\boldsymbol{N}$, and $\mathbf{i}$ are the diagonal reluctance matrix, the loop set matrix that relates the branch fluxes to the loop fluxes, the linkage matrix, and the vector of coil currents, respectively. The force vector acting on the rotor is computed using the principles of virtual work with respect to the virtual displacement vector $\mathbf{x}$

$$\mathbf{f} = -\frac{1}{2}\boldsymbol{\Phi}_{\text{m}}^{\text{T}}\frac{\partial\boldsymbol{\Re}}{\partial\mathbf{x}}\boldsymbol{\Phi}_{\text{m}}. \tag{8}$$

Based on the idealized flux distribution, the force amplitude, ripple, and angle can be predicted for various rotor and stator geometries, winding skew and distribution, and different motor and levitation currents. On one hand, in Matlab sript, a considerably greater flexibility can be achieved for example in testing of the effects of current ripple or when using the model for control verification purposes. On the other hand, compared with the FEM, the accuracy is significantly limited especially for IPM rotor geometries with thin iron bridges, which experience local strong saturation points [13], [18].

In Figs. 6 and 8 the RN obtained flux densities are presented for stand-still rotor at initial position. When rotating, the MMFs and reluctances are updated in time. This changes flux distribution and causes force variations. In Figs. 7 and 9 the corresponding average forces are shown during one rotor revolution. The closest RN results to the FEM ones are achieved for the SPM rotor (Fig. 6–9).

For the IPM rotor, the force amplitudes computed with the basic RN model presented here differ considerably from the FEM obtained values (Fig. 11).

Apart from the force capacity verification, the RN can also be applied for prediction of errors in the generated levitation force vector as well as tuning of pole pitch and height, segmentation of PMs, and skew in terms of conductors in a slot in multilayer windings (similarly to FEM). Both the motor and levitation windings can have a step shortening [2]. The RN script copies the initial parameters from the motor design part to form stator and rotor reluctance maps, the rotor PM magneto-motive force (MMF), the torque-producing winding MMF, and the force-producing winding MMF.

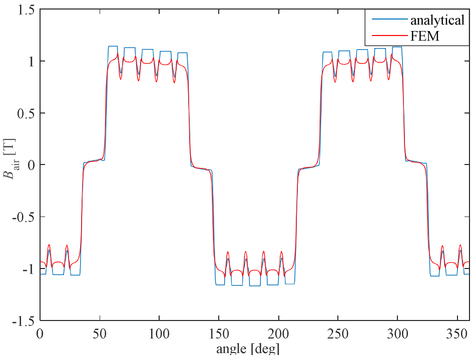

Fig. 6. Magnetic flux density B as a function of angle in the air gap of the 4-pole 5 kW SPM test case bearingless motor for the motor current peak amplitude i_{m}= 0.667 A and the levitation current peak amplitude i_{s}= 3 A.

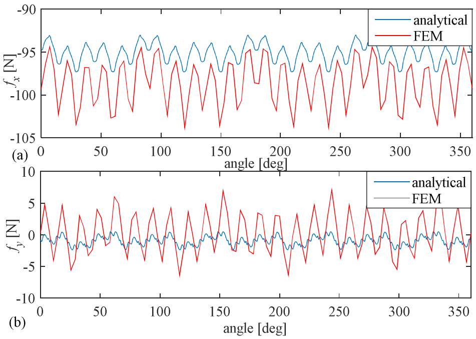

Fig. 7. Magnetic forces (a) f_x (b) f_y, for the motor current peak amplitude i_{m} = 0.667 A and the levitation current peak amplitude i_{s} = 3 A in the 4-pole 5 kW SPM test case motor.

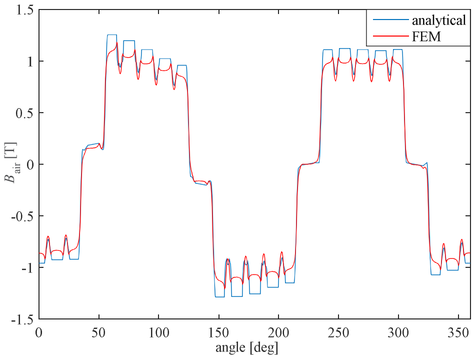

Fig. 8. Magnetic flux density in the air gap B_{air} of the 4-pole 5 kW SPM test case bearingless motor for the motor current amplitude i_{m}= 12 A and the levitation current amplitude i_{s} = 8 A.

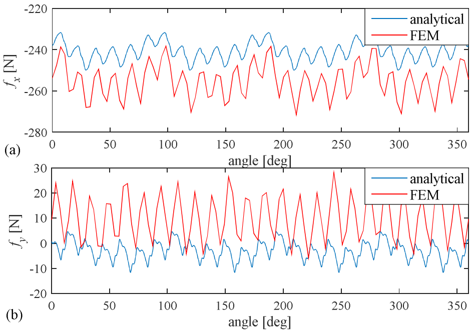

Fig. 9. Magnetic forces (a) f_x (b) f_y, for the motor current peak amplitude i_{m} = 12 A and the levitation current peak amplitude i_{s} = 8 A in the 4-pole 5 kW SPM test case motor.

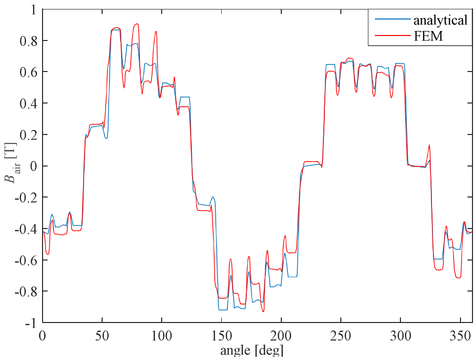

Fig. 10. Magnetic flux density in the air gap B_{air} of the 4-pole 5kW IPM test case bearingless motor for the motor current peak amplitude i_{m} = 12 A and the levitation current peak amplitude i_{s} = 8 A.

After solving for the magnetic flux density in the air gap, the script estimates the magnetic forces and their variations with respect to rotor position and time.

Fig. 6, Fig. 8, and Fig. 10 present a comparison of the magnetic flux density in the middle of the air gap of the test case machine of 5 kW at 30000 r/min in selected working conditions. The results are equivalent in terms of accuracy with respect to the FEM for the upscale 50 kW machine [18].

The predicted forces and their variations are different from the FEM results, particularly for the IPM rotor geometry. The errors increase for the higher flux values. The more dense and complex RN should be implemented where slot leakage would be modelled. Fig. 12 and Fig. 13 compare the force error angle and force amplitude variations for the FEM and the RN depending on the magnet angle. The magnet angle defines the width of the surface-mounted or inner-mounted PMs.

A correlation is seen between the minima and graph shapes; however, in general, the levitation performance indices predicted by the basic RN are different from the ones obtained by the FEM. Fig. 13 shows the RN limitation as there is no difference for the performance indices of the loaded and the unloaded machine computed by the RN, which is not the case in the FEM.

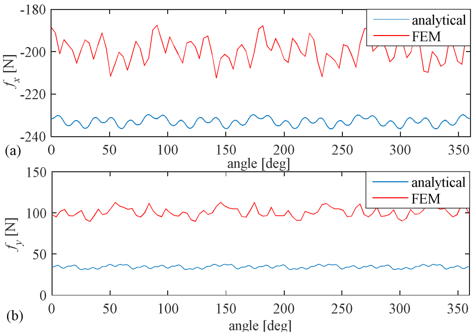

Fig. 11. Magnetic forces (a) f_x (b) f_y, for the motor current amplitude i_m = 12 A and the levitation current amplitude i_s = 8 A in the 4-pole 5 kW IPM test case motor.

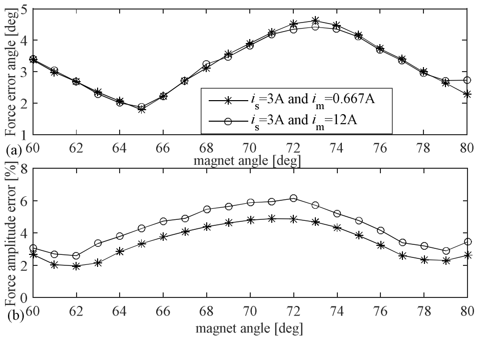

Fig. 12. FEM results for SPM motor for different motor currents and levitation currents: (a) Maximum levitation force error angle as a function of magnet angle for a fixed initial magnet thickness. (b) Maximum levitation force amplitude error as a function of magnet angle.

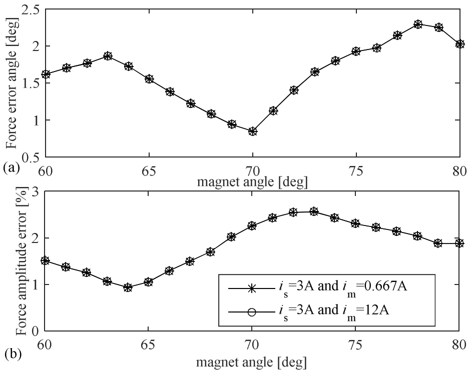

Fig. 13. RN results for SPM motor for different motor currents and levitation currents: (a) Maximum levitation force error angle as a function of magnet angle for a fixed magnet thickness. (b) Maximum levitation force amplitude error as a function of magnet angle.

IV. FEM DESIGN OF THE TEST MACHINE

The analytically designed SPM and IPM bearingless motors are evaluated in the FEM. The 5 kW machine is considered as a test case, but upscaling to 50 kW is also possible [18].

Fig. 14 and Fig. 15 show the geometries and flux distributions of the SPM and IPM machines, respectively. The IPM machine has been fine-tuned in the FEM by manually iterating the initial dimensions obtained from the analytical method. Different numbers of equally dimensioned magnet fragments have been studied with respect to minimizing the force error angle [13]. In the case of the SPM, the geometry parametrization is significantly easier, and therefore, the GA optimization has been applied.

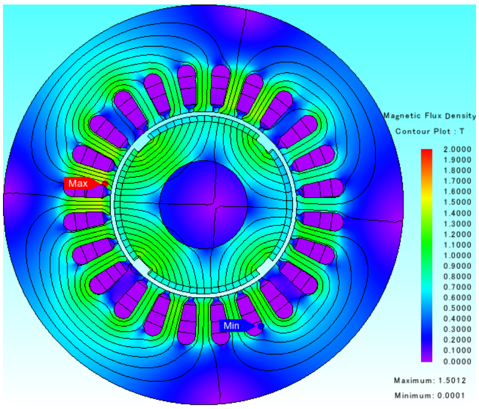

Fig. 14. Magnetic flux density contour and flux lines for the motor current amplitude i_m = 12 A and the levitation current amplitude i_s = 8 A in the 4-pole 5 kW SPM test case motor. The carbon band of 2.5 mm (not shown) retains the magnets and a magnetic air gap of 0.6 mm.

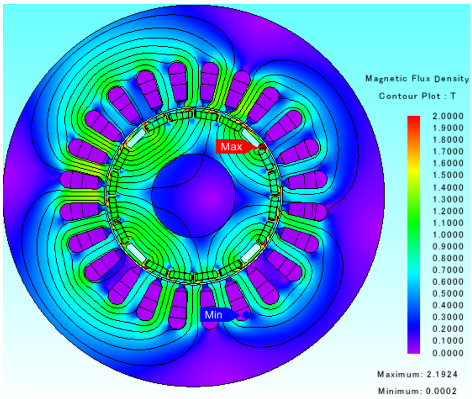

Fig. 15. Magnetic flux density contour and flux lines for the motor current amplitude $i_m = 12$ A and the levitation current amplitude $i_s = 8$ A in the 4-pole 5 kW IPM test case motor.

In the FEM optimization, a single-objective GA is applied similarly to the analytical optimization in the predesign of the motor. A single fitness function η that maps the chromosomes into the fitness values comprises three subfunctions η_n each multiplied by the predefined weight w_n

$$\eta = \sum_{n=1}^{N} w_n \eta_n, \tag{9}$$

where N equals the number of objective subfunctions. The design objectives are: the force amplitude ripple df_y scaled by the average absolute force (corresponding to error angle for small y-force variations as verified in Fig. 12 and Fig. 16), the force amplitude error df_x scaled by the average absolute force, and the torque ripple scaled by the average torque. By demanding the force vector in the x-direction the computation of the objective subfunctions is simplified. The importance of the error angle is stressed with the five times as high weight as for the other subfunctions. Additionally, the mean nominal force amplitude and the average nominal torque should be greater than or equal to the force and torque obtained from the initial case. For fast computation, only the magnet thickness and the magnet angle are varied in the optimization with the rest of the geometry remaining fixed. The optimization uses nominal speed, torque, and maximum force command in the x-direction. Fig. 17 shows the evolution of the performance objective subfunctions during ten generations of cases. The optimized geometry is shown in Fig. 14.

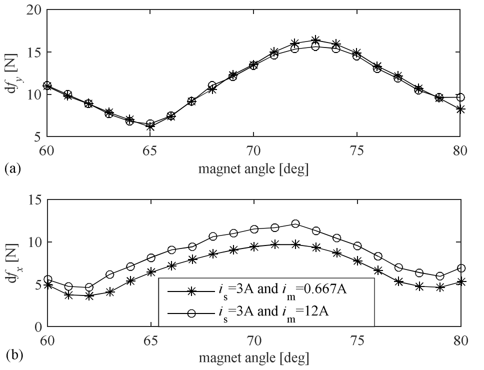

Fig. 16. FEM results for the SPM motor for different motor currents and levitation currents for a scenario where the force command in the x-direction is executed. The force amplitude is ≥100 N during the test.
(a) Range of change of f_y (corresponding to the force error angle from Fig. 11a as a function of magnet angle. (b) Range of change of f_x (corresponding to the force amplitude error from Fig. 11b as a function of magnet angle.

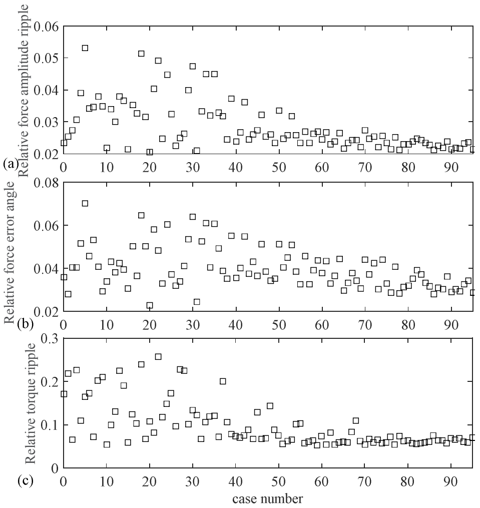

Fig. 17. Response graphs from the FEM optimization of SPM 5 kW 30000 r/min motor. (a) Force amplitude ripple df_x scaled by the absolute force value. (b) Force amplitude ripple df_y scaled by the absolute force value. (c) Torque ripple dT scaled by the absolute torque value.

V. Experimental Results

A. Custom-built force measurement rig

The radial force production capabilities of the designed IPM bearingless motor are validated by a special custom-built measurement rig presented in Fig. 18. This identification rig consists of two xy-axis linear tracks. The linear track mover position is controlled with Beckhoff stepper motors. Both sides are equipped with a force sensor. The rotor ends of the machine under identification are connected to the measurement sensors so that the force applied to the rotor can be measured for different positions in the air gap.

The main components of the identification rig are listed in Table I. The rotor can be moved inside the air gap with the

TABLE I COMPONENTS OF IDENTIFICATION RIG

Component	Type	Manufacturer
Stepper motor	AS1060	Beckhoff
Linear track	KK60	Hiwin
Force sensor	Mini85	ATI Industrial Automation

smallest discrete step of 1.3 µm when micro stepping is applied in the stepper motors. The sensors measure force and torque on the *xyz* axes. The resolution of the force measurement on the *xy* axes is 0.32 N in the range of ±1900 N. The measurement bandwidth is 5 kHz. The force sensor self-resonance is 2400 Hz on the *xy* axes and 3100 Hz on the *z*-axis.

The mechanical bearings are placed between the force sensors and the rotor enabling rotation during an identification process.

B. Measurement results

The prototype machine consists of two identical bearingless motors, which enable control of the rotor movement in the *xy* directions and tilting about the *xy* axes. The *z*-direction movement is controlled by a classical axial AMB. The force capacity and force variations of the bearingless motors are validated against the FEM model. The right-hand side of the prototype machine unit, which is shown in Fig. 18, is referred here as the drive end (D-end) because of the assumed connection to the driving/driven turbine/compressor wheel, and the other side is referred as the non-drive end (ND-end).

The capability of measuring the radial force can be used to verify the unbalance magnetic pull caused by the magnets embedded in the rotor, the radial force-producing capacity as a function of supplied levitation current, and the force error angle as a function of rotor mechanical angle. In order to be able to measure these parameters, the rotor must be moved to a reference position where the magnetic field caused by the PMs is uniform. This point is referred to as a magnetic center. The magnetic center is identified by the force feedback from the sensors so that the force on the *xy* axes is zero when the gravity effect is taken into account.

The unbalance magnetic pull caused by the magnets is measured by moving the rotor on the *x*-axis and measuring the corresponding force. This parameter is required in the control synthesis; it is also called ‘position stiffness’ in AMB applications, abbreviated generally as k_x. Fig. 19 shows that there is a slight variation between the FEM result and the measurement from the D-end of the machine.

The radial force-producing capacity as a function of supplying current in the levitation windings is the second parameter needed in the control synthesis. This parameter is also called ‘current stiffness,’ generally denoted by k_i. The measurement is carried out by supplying a *q*-axis current into the levitation windings. The rotor is positioned so that the *d*-axis of the magnets is aligned with the *x*-axis of the stator. In this position, the *d*-axis current with a zero current vector angle in the levitation windings provides force on the *y*-axis, and thus, a *q*-axis current provides force in the *x*-axis direction. Fig. 20 depicts the measured force as a function of levitation current. Both the D-end and the ND-end are compared with the FEM simulation results. There are only small variations between the lines.

One of the most important aspects in the bearingless motor design is the minimization of the force error angle. Force error angle is measured by providing current in the levitation windings and changing the angle of the rotor. At the same time, a current vector angle in the levitation windings must be changed in relation to the rotor angular position to keep the constant force direction relative to the stator. A mechanical bearing between the rotor and the force measurement sensor causes displacement error in the *xy* plane when the rotor angle is changed. For this reason, the magnetic center must be searched every time the rotor angle is changed. The measured force error angle from the both ends of the machine is shown in Fig. 21. It is clear that there is a difference between the FEM and the measured error angle. However, the measured error angle curves are following the FEM curve pattern.

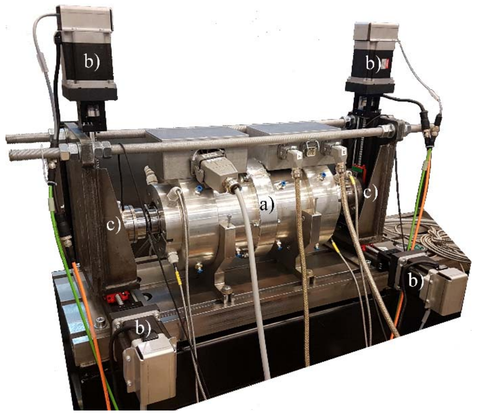

Fig. 18. Photograph of the experimental measurement setup. It consists of a bearingless machine and an external identification rig (a) Bearingless machine under force identification test. (b) Beckhoff stepper motor connected to a linear track. (c) Three degrees-of-freedom force measurement sensor

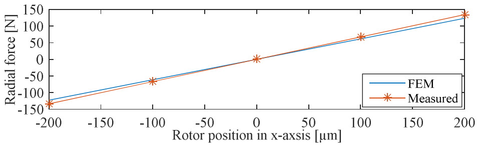

Fig. 19. Unbalance magnetic pull caused by the magnets embedded in the rotor. The measured force is compared with the FEM simulation result.

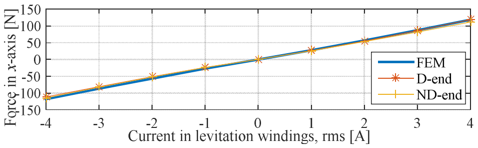

Fig. 20. Produced radial force on the *x*-axis as a function of current in the levitation windings. The motor windings are not under load.

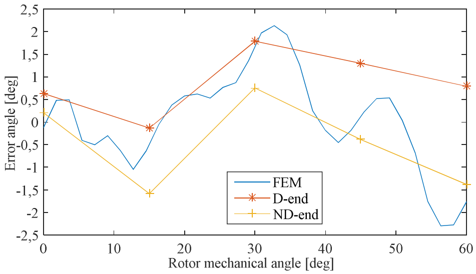

Fig. 21. Unbalance magnetic pull caused by magnets embedded in the rotor. The measured force is compared with the FEM results.

Reasons behind these discrepancies can be manufacturing nonidealities, differences in the magnet segments, and errors in the searched magnetic centers.

VI. CONCLUSION

This paper addresses the bearingless PM motor design optimization when applying custom DE-assisted CAD methods for preliminary fast machine sizing and for accurate performance tuning. For initial machine sizing an analytical method is applied. The featured RN numerical solution is very simple compared with the FEM approach. However, the computation time is a tiny fraction of that of a FEM solution, allowing fast iterative design optimization and control simulation capabilities. The GA-optimized motor design provides initial dimensions for further fine-tuning. However, the accuracy of the RN-predicted force error angle is not satisfactory. Accuracy of the results in comparison with FEM are geometry sensitive. The applied RN solution has to be refined in the future work. However, the extensively increased complexity of the RN could result in computation times comparable with the FEM while the code preparation effort for each new geometry would be greater than for the FEM. The FEM simulations combined with the GA optimization provide a very good method for final rotor geometry tuning. A compromise between the minimization of the force error angle, the force amplitude error, and the torque ripple relative to the levitation force amplitude can be achieved. The final design of the test case IPM bearingless motor is implemented in the FEM, and the manufactured machine is tested in the laboratory conditions. The force capability, control coefficient identification, and error angle measurements are carried out using a unique custom-built identification rig. The measured results correspond well to the FEM-predicted values. The presented methodology and results are extendable to other bearingless machine types.

ACKNOWLEDGMENT

The authors would like to express their gratitude to the Academy of Finland, grant No. 270012, No. 304071, and No. 304784 and to Business Finland (Dnro 1170/31/2016) for their financial support.

REFERENCES

[1] J.R. Hendershot and T.J.E. Miller, *Design of brushless permanent-magnet machines*, 2nd ed., USA: Motor Design Books LLC, 2010.

[2] J. Pyrhonen, T. Jokinen and V. Hrabovcova, *Design of rotating electrical machines*, John Wiley & Sons, 2nd ed., Chichester, U.K., pp. 314, 2014.

[3] T.J.E. Miller, M. McGilp and A. Wearing, "Motor design optimisation using SPEED CAD software," *IEE Seminar on Practical Electromagnetic Design Synthesis*, pp. 2/1–2/5, 1999.

[4] R.P. Jastrzebski, T. Sillanpaa, P. Jaatinen, A. Smirnov, J. Vuojolainen, T. Lindh, A. Laiho and O. Pyrhönen, "Automated design of AMB rotor systems with standard drive control software and hardware technologies," in *International Symposium on Magnetic Bearings*, 2016.

[5] A. Chiba, T. Fukao, O. Ichikawa, M. Oshima, M. Takemoto, and D.G. Dorrell, *Magnetic bearings and bearingless drives*, Amsterdam, The Netherlands: Elesevier, 2005.

[6] G. Stumberger, D. Dolinar, U. Pahner and K. Hameyer, "Optimization of radial active magnetic bearings using the finite element technique and the differential evolution algorithm," in *IEEE Transactions on Magnetics*, vol. 36, no. 4, pp. 1004–1008, 2000.

[7] H. Chang and S. Chung, "Integrated design of radial active magnetic bearing systems using genetic algorithms," in *Mechatronics*, vol. 12, pp. 19–36, 2002.

[8] R.P. Jastrzebski, K.M. Hynynen and A. Smirnov (2010). "H_∞ control of active magnetic suspension," in *Mechanical Systems and Signal Processing*, no. 24, vol. 4, pp. 995–1006, 2010.

[9] G.Y. Sizov, P. Zhang, D.M. Ionel, N.A.O. Demerdash, M. Rosu, "Automated multi-objective design optimization of pm ac machines using computationally efficient FEA and differential evolution," in *IEEE Trans. on Industry Applications*, vol. 49, no. 5, pp. 2086–2096, 2013.

[10] M.E. Beniakar, A.G. Sarigiannidis, P.E. Kakosimos, A. G. Kladas, "Multiobjective evolutionary optimization of a surface mounted pm actuator with fractional slot winding for aerospace applications," in *IEEE Trans. on Magnetics*, vol. 50, no. 2, pp. 2–5, 2014.

[11] A. Wang, Y. Wen, W.L. Soong and H.Li, "Application of a hybrid genetic algorithm for optimal design of interior permanent magnet synchronous machines," in *IEEE Conference on Electromagnetic Field Computation*, pp. 1–1, 2016.

[12] J. Baek, S.S.R. Bonthu, S. Choi, "Design of five-phase permanent magnet assisted synchronous reluctance motor for low output torque ripple applications," in *Trans. on IET Electric Power Applications*, vol. 10, no. 5, pp. 339–346, 2016.

[13] P. Jaatinen, R.P. Jastrzebski, H. Sugimoto, O. Pyrhönen and A. Chiba, "Optimization of the rotor geometry of a high-speed interior permanent magnet bearingless motor with segmented magnets," in *International Conference on Electrical Machines and Systems*, ICEMS, pp. 962–967, 2015.

[14] K.V. Price, R.M. Storn and J.A. Lampinen, "Differential Evolution A Practical Approach to Global Optimization," Berlin: Springer-Verlag, pp. 37–130, 2005.

[15] S. Das, P. Nagaratnam Suganthan, "Differential Evolution: A Survey of the State-of-the-Art, in IEEE Transactions on Evolutionary Computation," vol. 15, no. 1, pp. 4–31, 2011.

[16] J. Asama, R. Natsume, H. Fukuhara, T. Oiwa and A. Chiba, "Optimal suspension winding configuration in a homo-polar bearingless motor," in *IEEE Transaction on Magnetics*, vol. 48, no. 11, pp. 2973–2297, 2012.

[17] J. Amemiya, A. Chiba, D.G. Dorrell and T. Fukao, "Basic characteristics of a consequent-pole-type bearingless motor," in *IEEE Transaction on Magnetics*, vol. 41, no. 1, pp. 82–89, 2005.

[18] R.P. Jastrzebski, P. Jaatinen, H. Sugimoto, O. Pyrhönen and A. Chiba, "Design of a bearingless 100 kW electric motor for high-speed applications," in *International Conference on Electrical Machines and Systems*, ICEMS, pp. 2008–2014, 2015.

Publication V

Jaatinen, P., Vuojolainen, J., Nevaranta, N., Jastrzebski, R., and Pyrhönen, O.
Control system commissioning of fully levitated bearingless machine

Reprinted with permission from
Modeling, Identification and Control
vol. 40, no. 1, pp. 27–39, 2019
©2019, Norwegian Society of Automation Control

Modeling, Identification and Control, Vol. 40, No. 1, 2019, pp. 27–39, ISSN 1890–1328

Control System Commissioning of Fully Levitated Bearingless Machine

P. Jaatinen[1] J. Vuojolainen[1] N. Nevaranta[1] R. Jastrzebski[1] O. Pyrhönen[1]

[1]*Department of Electrical Engineering, Lappeenranta University of Technology, FI-53851 Lappeenranta, Finland*
E-mail: pekko.jaatinen@lut.fi, jouni.vuojolainen@lut.fi, niko.nevaranta@lut.fi, rafal.jastrzebski@lut.fi, olli.pyrhonen@lut.fi

Abstract

The bearingless permanent magnet synchronous motor (BPMSM) is a compact motor structure that combines the motoring and bearing functions based on well-designed integrated windings for generating both torque and magnetic suspension force. In order to achieve a successful high-performance control design for the BPMSM, an adequate model of the rotor dynamics is essential. This paper proposes simplified multiple-input and multiple-output (MIMO) control approaches, namely the pole placement and the linear-quadratic regulator (LQR), that allow to carry out identification experiments in full levitation. Additionally, the stability of the MIMO levitation controller is verified with the rotation tests. Compared with other recently published works, the novelty of this paper is to experimentally demonstrate that a stable fully levitated five-degrees-of-freedom (5-DOF) operation of a bearingless machine can be achieved by the proposed approach, and thereby, options for commissioning of such a system are obtained.

Keywords: Bearingless, magnetic levitation, MIMO control, self-levitating, system identification, 5-DOF

1 Introduction

Operation in the high-speed region is very beneficial especially in the field of compressor applications. The compressor pressure ratio and mass flow rate can be raised by increasing the rotational speed Yoon et al. (2013). In the speed range of 20 000 r/min and over, the electrical motor efficiency can be increased by achieving the minimum weight-power ratio. It is clear that operating in the high-speed region increases both the motor and compressor efficiency. Nowadays there is a growing interest in high-speed technology, where the traditional bearing solution is replaced by a more advanced solution, namely active magnetic bearings (AMBs) Gerhard Schweitzer (2009). The well-known benefits of AMBs are contact-free operation, active control of the rotor, and self diagnostic properties. As AMBs do not need oil lubrication because of the magnetic levitation of the rotor, they are the most suitable solution for oil-free compressor applications in the fields of pharmacy and food industry. However, one drawback of the AMBs is that they extend the total length of the rotor as the radial and axial magnetic bearings need a certain amount of space, which results in an increased axial length of the rotor shaft along with a larger and more complicated motor structure. Depending on the operational speed and rotor mechanical dimensions, this extra length can lower the flexible mode frequencies to the operating region. This is an unwanted feature as the operation close to the flexible mode is difficult. From the viewpoint of the overall system behavior, and especially with respect to controllability, it is advantageous that the rotor does not need to pass flexible modes.

Reducing the rotor length, simultaneously keeping the benefits of the traditional AMBs, a self-levitating or bearingless motor technology can be applied Chiba et al. (2009). In a bearingless motor, one stator pro-

doi:10.4173/mic.2019.1.3 © 2019 Norwegian Society of Automatic Control

duces both the levitation force to support the rotor and the torque for rotation. This can be achieved by the use of separate windings or by different common winding configurations in one stator unit Chiba et al. (2013). Because the windings are of a three-phase type for both generating torque and levitation force, commercial motor drives can be used, and thus, the amount of power electronics is decreased compared with the traditional AMB configuration.

Bearingless operation is possible also with single-stator disc-shape motors Mitterhofer and Amrhein (2012). Other applications that exploit the benefits of bearingless operation are artificial hearts Hoshi et al. (2006) and canned pump Warberger et al. (2010) applications, where a long air gap length is needed. However, in this paper, a standard horizontal-type machine equipped with two bearings is considered. The machine type with two or more supporting bearings can handle a higher loading force caused by the weight and mass flow of the impeller wheel.

In general, when dealing with high-speed machines, it is important to analyze the rotor behavior Swanson et al. (2008). As a result of the dynamic properties of the rotor structure, bending occurs when the rotation speed is increased. Without qualitative analysis of the rotor dynamics, the rotor operating point in nominal operation can be close to the rotor flexible mode. Thus, it is of great importance that in the machine commissioning phase, the rotor dynamics are identified in order to verify the flexible modes of the rotor Noh et al. (2017). A common method is to use an impulse hammer with vibration sensors to conduct the mode analysis. Naturally, as the AMB system is equipped with a displacement sensor and power electronics, the rotor identification can be made in the system without removing the rotor.

In recent years, a variety of different bearingless machine setups have been introduced in the literature, and their control has become a topic of significant interest. The five-degrees-of-freedom (5-DOF) control of a bearingless machine has been reported in Takemoto et al. (2009); Yamamoto et al. (2011); Severson et al. (2017), and other studies have considered the combination of a bearingless motor and a magnetic bearing in Cao et al. (2017); Schneider and Binder (2007). Here, the 5-DOF operation refers to two radial xy-planes and one axial z-plane of the control axes. Note, however, that many of the reported prototypes are laboratory versions, where all degrees of freedom (DOF) have not been evaluated. It is also worth emphasizing that in these examples the most common structure is a bearingless motor with a ball bearing supporting the other end of the rotor Chiba et al. (2013); Sun et al. (2016a); Ooshima et al. (2015); Yang et al. (2010); Huang et al. (2014). Although there are a few publications where the system has one bearingless motor, it is not shown or reported how the conical movement of the rotor is stabilized Qiu et al. (2015); Sun et al. (2016b); Xue et al. (2015); Yang and Chen (2009); Chen and Hofmann (2011); Cao et al. (2016); Zhang et al. (2016); Zhao and Zhu (2017). In addition, a common factor in all these publications is that they apply PID-based position controllers. To the authors' knowledge, only the model-based controller has been addressed in Messager and Binder (2016) for machines of the horizontal dual bearingless motor type. Another approach based on a linear-quadratic regulator (LQR) controller for a bearingless motor has been introduced in Kauss et al. (2008). However, the presented prototype is 2-DOF and the other end is supported by a ball bearing.

In order to conduct rotor identification, the rotor must be fully levitated. The aim of this paper is to study MIMO control approaches that provide a stable fully levitated operation of a bearingless machine. The novelty of this paper compared with the previously reported studies is that it provides experimental results that show the actual 5-DOF operation of a bearingless machine, and more importantly, introduces results of the full levitation. For this purpose, a 4-DOF MIMO controller is used for the radial position control. The axial position is controlled with an axial AMB, and it is separated from the radial controller. Rigid body is used as an initial rotor model. Pole placement and LQR radial position controllers are used, and the suitability of the controllers is discussed. The designed 4-DOF radial controllers are simulated and tested in a 10 kW dual motor interior permanent magnet bearingless machine. Additionally, the stability of the levitation control is verified with low-speed rotation tests. Finally, system identification experiments are carried out with the pole placement and the LQR controller by superposing a stepped sine excitation signal to the system.

2 Problem statement

To operate in a high-speed region, the dynamic properties of the rotor must be known. An initial analysis of the rotor dynamics is normally done with analytical tools, by which the natural frequencies of the rotor are found. However, experimental tests are mandatory to verify the model and detect possible defects of the rotor. One common method to carry out experimental modal analysis is to use an impulse hammer, which includes for example an integral piezoelectric accelerometer sensor to produce the excitation to the rotor and measure the applied force Kolondzovski et al. (2010). When the rotor system is equipped with AMBs, the same modal analysis can be done in the system. Similarly as in the impulse hammer test, the AMBs produce the excitation signal and displacement sensors are used to measure the vibration of the rotor. Based on the results, the natural frequencies of the rotor can be found. The obtained results can be used to improve the analytical model by updating the rigid and flexible modes, thereby resulting in a more accurate system model.

To simplify this procedure in a bearingless machine, the rotor can be levitated without a rotating field as the rotor identification is made at a standstill. In this case, the decoupling of the torque and levitation windings can be ignored. When knowing the rotor angle and transforming the three-phase windings into a 2-phase system, the control principles of traditional AMB systems can be adopted.

2.1 System description

The prototype machine consists of two identical interior permanent magnet (IPM) bearingless motors (BMs) together with an axial magnetic bearing. Fig. 1. depicts the prototype machine. The axial magnetic bearing is in the middle of the machine, and bearingless motors are placed on opposite sides of the machine. This provides a symmetrical rotor structure when the load is not considered. A block diagram of the full control system is shown in Fig. 2. The rotor position is measured with an eddy-current sensor differentially from the radial direction and single ended from the axial direction. A non-contact encoder is placed on the right side of the machine to sense the rotor angle. Moreover, five industrial motor drives are used to operate the machine: one is needed for the axial bearing and two for the torque and radial force production for each BM. Each motor drive includes a field programmable gate array (FPGA), where the inner loop current controller is implemented. A block diagram of the inner current control loop is illustrated in Fig. 3. The upper-level control is implemented in a Beckhoff industrial PC, and the communication between the industrial PC and the motor passes through an EtherCAT industrial fieldbus. The sampling time of the control system is 50 μs.

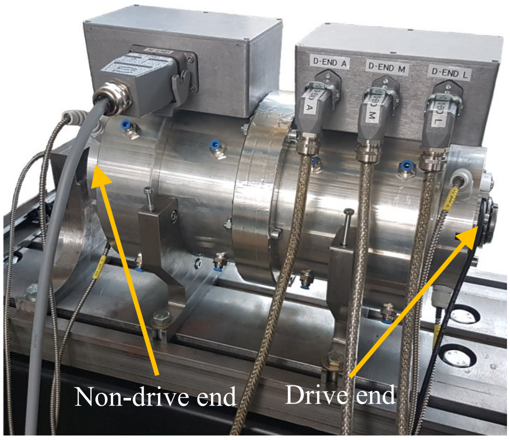

Figure 1: Photograph of the 10kW dual motor bearingless machine. The axial AMB is in the middle of the machine and bearingless motors are located on both ends.

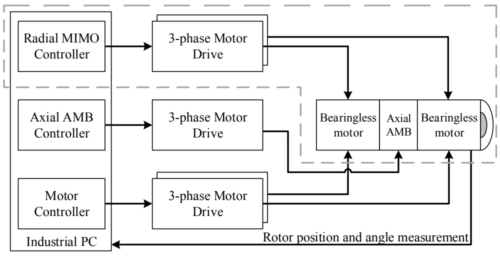

Figure 2: Block diagram describes the overview of the system configuration. All controllers are implemented on a Beckhoff industrial PC shown in far left. In total, five 3-phase motor drives are used to produce levitation force and torque. Three drives are allocated for the 5-DOF levitation purposes, and both motors are driven separately. The rotor position in 5-DOF is measured together with the rotor angular position.

3 Model of the system

In this paper, the rigid rotor model is used to tune the proposed control approaches. In general, a mathematical model of the system can be presented using a state-space representation

$$\begin{aligned}\dot{\mathbf{x}}(t) &= \mathbf{A}\mathbf{x}(t) + \mathbf{B}\mathbf{u}(t) \\ \mathbf{y}(t) &= \mathbf{C}\mathbf{x}(t)\end{aligned} \tag{1}$$

where $\mathbf{A}$ is the system matrix, $\mathbf{B}$ is the input matrix, and $\mathbf{C}$ is the output matrix. The vectors $\mathbf{x}$ and $\mathbf{u}$ are state and input vectors, respectively. In this paper, separate models for the axial and radial directions are used as the coupling is not strong. In the axial direction, the rotor is modeled as a point mass, whereas in the radial direction, a rigid body rotor model is used.

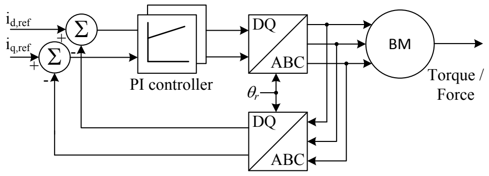

Figure 3: Block diagram of the PI current controller scheme applied to motor drives that produce the radial force. ABC: three-phase reference frame and DQ: rotor reference frame.

3.1 Rotor model

General form of the rotor model is presented in the following:

$$\mathbf{M}\ddot{\mathbf{q}}(t) + (\mathbf{D} + \Omega\mathbf{G})\dot{\mathbf{q}}(t) + \mathbf{K}\mathbf{q}(t) = \mathbf{F}(t), \tag{2}$$

where $\mathbf{M}$ is the mass matrix, $\mathbf{D}$ is the damping matrix, Ω is the rotational speed, $\mathbf{G}$ is the gyroscopic matrix, $\mathbf{K}$ is the stiffness matrix, $\mathbf{F}$ is the force applied to the rotor and $\mathbf{q}$ is the displacement vector of the rotor. This model can be simplified to a rigid rotor model, which describes the rotor movement with respect to the center of the rotor mass Smirnov (2012)

$$\mathbf{M}\ddot{\mathbf{q}}(t) + \Omega\mathbf{G}\dot{\mathbf{q}}(t) = \mathbf{F}(t), \tag{3}$$

where $\mathbf{M}$ is the diagonal matrix including rotor mass and inertia at the center of mass, $\mathbf{q} = \begin{bmatrix} x & y & \alpha_x & \alpha_y \end{bmatrix}^T$ is the vector that describes the rotor position in the xy-axis and the angle around the corresponding axis at the center of mass. As the displacement sensors and the magnetic bearings are not located at the center of mass, a coordinate transformation is needed for the control design and simulation purposes. To acquire the absolute location in the xy-axis of the sensors, $\mathbf{q_s} = \begin{bmatrix} x_{D,s} & y_{D,s} & x_{ND,s} & y_{ND,s} \end{bmatrix}^T$ and the magnetic bearing locations, $\mathbf{q_b} = \begin{bmatrix} x_{D,b} & y_{D,b} & x_{ND,b} & y_{ND,b} \end{bmatrix}^T$ at the drive and non-drive end of the machine, the following transformation matrices are applied

$$\mathbf{q}_b = \underbrace{\begin{pmatrix} 1 & 0 & 0 & -a \\ 0 & 1 & -a & 0 \\ 1 & 0 & 0 & b \\ 0 & 1 & b & 0 \end{pmatrix}}_{\mathbf{T}_b} \mathbf{q}, \quad \mathbf{q}_s = \underbrace{\begin{pmatrix} 1 & 0 & 0 & -c \\ 0 & 1 & -c & 0 \\ 1 & 0 & 0 & d \\ 0 & 1 & d & 0 \end{pmatrix}}_{\mathbf{T}_s} \mathbf{q}, \tag{4}$$

where a, b are the drive-end and non-drive-end bearing locations from the center of the rotor mass, respectively and c, d are the drive-end and non-drive-end sensor locations from the center of mass. Rotor cross-sectional view is illustrated in Fig. 4.

Radial forces produced by the bearingless machine can be presented by the following equation

$$\mathbf{F}(t) = \mathbf{K}_x\mathbf{q}_b + \mathbf{K}_i\mathbf{i}_c, \tag{5}$$

where $\mathbf{F}$ is the total linearized radial force generated by the bearingless machine, $\mathbf{q}_b$ is the rotor position at the bearing location, $\mathbf{i}_c$ is the control current to the levitation windings, $\mathbf{K}_x$ is the diagonal position stiffness matrix, and $\mathbf{K}_i$ is the diagonal current stiffness matrix. The total force depends on the rotor position and current in the levitation windings. The coefficients $\mathbf{K}_x$ and $\mathbf{K}_i$ can be determined experimentally by different tests and measurements. Parameters of the prototype machine are listed in Table 1.

In Fig. 5 a) the position stiffness value is determined by moving the rotor in the air gap, and the force caused by the unbalance pull of the permanent magnets is measured. From this measurement, the slope of the position stiffness can be calculated, $\mathbf{K}_x = \triangle f_x / \triangle P_x$. The current stiffness is measured by applying current in the levitation windings and measuring the corresponding radial force. Similarly, from the measured slope, the current stiffness can be calculated, $\mathbf{K}_i = \triangle f_x / \triangle i_L$. It can be seen that the measured values are closely matching the FEM simulations presented in Fig. 5. Measured values are used in the control design. The force measurement setup is described in more detail in Jaatinen et al. (2016).

The rigid rotor model presented in (3) can be further simplified by neglecting the gyroscopic matrix as the rotor is not rotating during the identification, that is, $\Omega = 0$. Furthermore, this simplification is also valid for the rotating system when axial length of the rotor is much greater than the rotor diameter thus the gyroscopic effect is then negligible Gerhard Schweitzer (2009). By substituting (4) and (5) into (3), a simplified rigid rotor model is achieved

$$\mathbf{M}_b\ddot{\mathbf{q}}_\mathbf{b} = \mathbf{K}_x\mathbf{q}_b + \mathbf{K}_i\mathbf{i}_c. \tag{6}$$

where $\mathbf{M}_b = (\mathbf{T}_b^{-1})^T\mathbf{M}\mathbf{T}_b^{-1}$ is the mass matrix in the bearing plane. In the state-space form, the simplified rotor model is written as

$$\begin{aligned} \mathbf{A}_r &= \begin{bmatrix} \mathbf{0} & \mathbf{I} \\ (\mathbf{M}_b)^{-1}\mathbf{K}_x & \mathbf{0} \end{bmatrix}, \\ \mathbf{B}_r &= \begin{bmatrix} \mathbf{0} \\ (\mathbf{M}_b)^{-1}\mathbf{K}_i \end{bmatrix}, \\ \mathbf{C}_r &= \begin{bmatrix} \mathbf{T_s}\mathbf{T_b^{-1}} & \mathbf{0} \end{bmatrix}. \end{aligned} \tag{7}$$

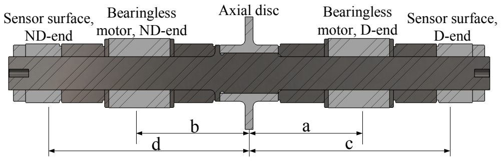

Figure 4: Cross-sectional view of the rotor in the prototype system. Locations of the bearingless motors and the sensor surfaces are measured respect of the center of mass.

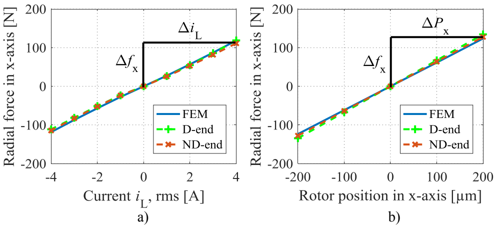

Figure 5: Simulated and measured current and position stiffnesses. The current stiffness can be calculated from the slope presented in a). In the same manner, the position stiffness can be calculated from the slope presented in b).

3.2 Actuator model

The actuator consists of the dynamics of the inner current control loop. A straightforward method to model the actuator dynamics is to use the bandwidth of the current controller

$$G_a = \frac{\omega_{bw}}{s + \omega_{bw}}, \tag{8}$$

where $\mathbf{G}_a$ is the approximate transfer function of the inner current loop and ω_{bw} is the bandwidth of the current controller.

In the simulation, the inner control loop consists of the PI controller, the motor drive model, and the bearingless motor model including the levitation windings. The motor drive is modeled as two-stage switching with a pulse width modulator. The bearingless motor is modeled in the dq reference frame as

$$\begin{aligned} u_d &= Ri_d + \frac{d}{dt}L_d i_d - \omega L_q i_q, \\ u_q &= Ri_q + \frac{d}{dt}L_q i_q + \omega L_d i_d, \end{aligned} \tag{9}$$

where u is the voltage over the levitation windings, R is the resistance of the levitation windings, L is the inductance of the levitation windings, i is the current of the levitation windings, and ω is the electrical angle.

3.3 Full model

A full model can be produced by combining the rotor model with the actuator model.

$$\begin{aligned} &\mathbf{A} = \begin{bmatrix} \mathbf{A}_a & \mathbf{0} \\ \mathbf{B}_r\mathbf{C}_a & \mathbf{A}_r \end{bmatrix}, \quad \mathbf{B} = \begin{bmatrix} \mathbf{B}_a \\ \mathbf{0} \end{bmatrix}, \\ &\mathbf{C} = \begin{bmatrix} \mathbf{0} & \mathbf{C}_r \end{bmatrix}, \end{aligned} \tag{10}$$

where $\mathbf{B}_a = -\mathbf{A}_a = diag\begin{bmatrix}\omega_{bw} & \omega_{bw} & \omega_{bw} & \omega_{bw}\end{bmatrix}$ is the current controller bandwidth, and the rigid rotor model matrices are denoted by the subscript r.

3.4 Axial AMB model

The axial direction of the rotor can be controlled separately as the coupling to the radial direction is negligible in the center of the air gap. As the axial AMB controls only 1-DOF, the model of the rotor can be simplified to a point mass model

$$m\ddot{q} = K_x q_a + K_i i_c, \tag{11}$$

where m is the rotor mass, q_a is the acceleration of the rotor, K_i is the current stiffness, and K_x is the position stiffness.

4 MIMO control of a bearingless machine

In the literature, there are many publications that address the issues of the MIMO control of traditional AMB systems equipped with two radial and one axial AMBs Yoon et al. (2013); Gerhard Schweitzer (2009). The same principles can be adopted to the bearingless machine control. However, there are two major differences compared with the traditional AMB system. Firstly, the rotating magnetic flux that generates the levitating force is synchronous with the rotor rotation. Secondly, decoupling of the motor control from the levitation control is required. If the decoupling parameters are correctly identified, the motor control does not affect the performance of the levitation controller Ooshima et al. (2004). It is emphasized that in this paper, the decoupling controller is not taken into consideration as the rotor identification is conducted with a nonrotating rotor. Moreover, a 4-DOF MIMO radial controller with a PID-type axial controller for commissioning and rotor identification purposes is tuned based on a rigid rotor model.

Table 1: Machine parameters

Parameter	Symbol	Value	Unit
Nominal speed	Ω_{nom}	30 000	r/min
Nominal power per motor unit	P_{nom}	5	kW
Rotor mass	m	11.65	kg
Rotor inertia	J	0.232	kgm^2
Resistance, levitation winding	R	0.27	Ω
Inductance, levitation winding	L	3.27	mH
BM location	a, b	107.5	mm
Position sensor location	c, d	211	mm
Air gap length	l_δ	0.6	mm
Rotor length	l_{r}	480	mm
BM lamination stack length	l_{rl}	61	mm
BM lamination diameter	d_{rl}	68.8	mm
BM stator outer diameter	d_{s}	150	mm
Axial disk thickness	l_{a}	8	mm
Axial disk diameter	d_{a}	112	mm
Rotor shaft diameter	d_{rs}	33	mm
Current stiffness, measured	K_{i}	29	N/A
Position stiffness, measured	K_{x}	672	N/mm
Current stiffness, FEM	$K_{\text{i,FEM}}$	29.6	N/A
Position stiffness, FEM	$K_{\text{x,FEM}}$	618	N/mm
Maximum input deviation	u_{nmax}	2	A
Maximum output deviation	m_{n}	25	µm

Furthermore, an additional coordinate transformation is needed when comparing the bearingless system with the traditional AMB system. In Fig. 6, the principle of the radial force generation both in the x and y directions is shown. Here, the three-phase winding is transformed into a two-phase presentation. When the rotor is in a certain angular position, for instance 0 deg, where the poles are parallel with the stationary xy-reference frame, the corresponding two-phase current produces force in that axis. By changing the polarity of the current, the force direction can be reversed. By taking into account the rotation of the rotor in the coordinate transformation, the force can be generated at any angle. A radial position control-loop block diagram is presented in Fig. 7. Note the coordinate transformation between the position controller and the inner current controller.

4.1 State-feedback control with pole placement

One common control method for handling state equations is state feedback with pole placement, in which the locations of the closed-loop poles are selected to obtain the desired performance. As all states are not measurable, a state estimator is also needed. To remove the steady-state error, an integral state is augmented to the state feedback controller. The full discrete-time state equation can be written Franklin et al. (2010)

$$\begin{bmatrix}\mathbf{x}(k+1)\\ \mathbf{x}_I(k+1)\end{bmatrix} = \begin{bmatrix}\mathbf{\Phi} & \mathbf{0}\\ \mathbf{C} & \mathbf{I}\end{bmatrix}\begin{bmatrix}\mathbf{x}(k)\\ \mathbf{x}_I(k)\end{bmatrix} + \begin{bmatrix}\mathbf{\Gamma}\\ \mathbf{0}\end{bmatrix}\mathbf{u}(k) - \begin{bmatrix}\mathbf{0}\\ \mathbf{I}\end{bmatrix}\mathbf{r}(k), \tag{12}$$

where $\mathbf{\Phi}$, $\mathbf{\Gamma}$ are discretized system state and input matrices, $\mathbf{C}$ is the output matrix, $\mathbf{I}$ is the identity matrix, $\mathbf{x}$ is the system state vector, $\mathbf{x}_I$ is the integral state vector, $\mathbf{u}$ is the system input vector, and $\mathbf{r}$ is the reference input vector. The feedback law is then written as

$$\mathbf{u}(k) = -\begin{bmatrix}\mathbf{K} & \mathbf{K_I}\end{bmatrix}\begin{bmatrix}\mathbf{x}(k)\\ \mathbf{x}_I(k)\end{bmatrix}, \tag{13}$$

where $\mathbf{K}$ is the state feedback gain and $\mathbf{K}_I$ is the integrator gain.

The state estimator uses the following presentation

$$\hat{\mathbf{x}}(k+1) = \mathbf{\Phi}\hat{\mathbf{x}}(k) + \mathbf{\Gamma}\mathbf{u}(k) + \mathbf{L}(\mathbf{y}(k) - \mathbf{C}\hat{\mathbf{x}}(k)), \tag{14}$$

where $\hat{\mathbf{x}}$ is the estimated state vector and $\mathbf{L}$ is the feedback gain of the state estimator. In this paper, the state feedback controller is designed by using the principles presented in Gerhard Schweitzer (2009).

The main drawback of the pole-placement-based tuning is that it is not very intuitive. Secondly, when the system degree increases, also the number of poles to be placed increases, resulting in a more complex tuning problem. This is an important factor to be acknowledged, especially when including flexible modes to the control model.

4.2 Linear-quadratic regulator

There are other control methods that facilitate controller tuning by providing more intuitive tools, which do not need direct manipulation of the poles. One of these optimal control methods is the linear-quadratic regulator (LQR). The controller tuning is based on minimization of the quadratic cost function

$$\mathcal{J} = \frac{1}{2}\sum_{k=0}^{N}[\mathbf{x}^T(k)\mathbf{Q}_1\mathbf{x}(k) + \mathbf{u}^T(k)\mathbf{Q}_2\mathbf{u}(k)], \tag{15}$$

where $\mathcal{J}$ is the cost function, $\mathbf{x}$ is the state vector, $\mathbf{u}$ is the input vector, $\mathbf{Q}_1$ is the output weight function, and $\mathbf{Q}_2$ is the input weight function. The weighting

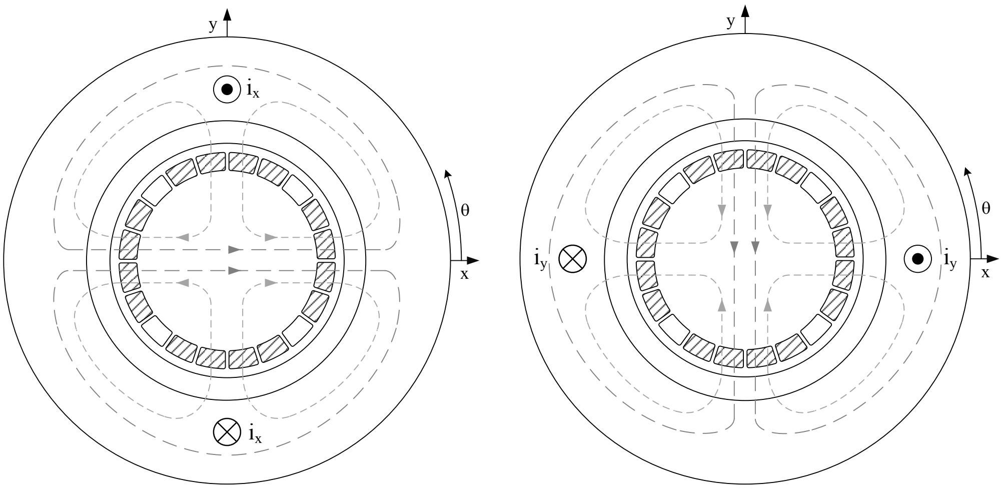

a) b)

Figure 6: Description of radial force generation in a permanent magnet bearingless motor. The three-phase windings are transformed into a two-phase presentation in the xy plane. The currents of the two-phase windings are denoted by i_x and i_y. The principle of producing radial force in the x-axis is shown in a). By applying current to the x phase windings, the flux is increased and decreased opposite to the air gap in x-axis. This flux unbalance produces the radial force. By applying negative current, the force direction can be reversed. In a similar fashion, the radial force in the y-axis can be produced by applying current in the y-phase winding.

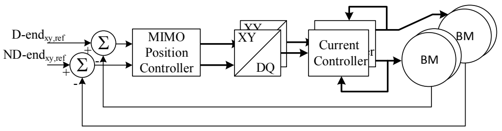

Figure 7: Block diagram of the position control loop.

functions are diagonal matrices that affect the states and inputs of the system. There are different methods to determine the weighting functions $\mathbf{Q}_1$ and $\mathbf{Q}_2$. One of the methods is called Bryson’s rule Franklin et al. (2010), where the effect of the state weight on the output follows

$$\mathbf{Q}_1 = \mathbf{C}^T \bar{\mathbf{Q}}_1 \mathbf{C}. \tag{16}$$

The weights are selected for the output by deciding how large a deviation of the output is acceptable

$$\bar{\mathbf{Q}}_{1,n} = \begin{pmatrix} 1/m_1^2 & 0 & \cdots & 0 \\ 0 & 1/m_2^2 & \cdots & 0 \\ \vdots & \vdots & \ddots & \vdots \\ 0 & 0 & \cdots & 1/m_n^2 \end{pmatrix}, \tag{17}$$

where m_n is the maximum deviation of the output signal. The weights for the inputs are selected by the maximum input signal amplitude

$$\mathbf{Q}_{2,n} = \begin{pmatrix} 1/u_{1max}^2 & 0 & \cdots & 0 \\ 0 & 1/u_{2max}^2 & \cdots & 0 \\ \vdots & \vdots & \ddots & \vdots \\ 0 & 0 & \cdots & 1/u_{nmax}^2 \end{pmatrix}, \tag{18}$$

where u_{nmax} is the maximum input signal deviation. Table 1 lists the values selected for the weights m and u based on several simulation iterations.

When designing the LQR-based controller, the degree of freedom is lower (two parameters) than with the pole placement method, where eight poles have to

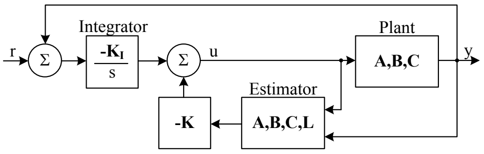

Figure 8: Block diagram of the state feedback controller. A state estimator is necessary for generating the full state vector including rotor acceleration, which is not measurable. Naturally, an integral action is added to remove the steady-state error.

be selected. This difference is amplified in the case of the flexible plant model, where more states are added to the system plant.

5 Experimental Results

Both controllers are tested with the prototype bearingless machine. First, the initial lift-up test is conducted and compared with simulations in Fig. 9. The rotor position is shown during the initial lift-up with the pole placement and the LQR controller. At the beginning of the test, the rotor is resting on the backup bearings, where it is levitated to the center of the air gap. Based on the simulations, it can be noted that the pole placement controller has a higher overshoot, but both controllers provide full levitation.

In Figs. 10 and 11, the current in the dq reference frame is shown for the pole placement controller and the LQR controller during the rotor lift-up sequence. Because of the unbalanced magnetic pull of the embedded magnets in the rotor, a high current peak is needed to lift the rotor away from the backup bearings to the center of the air gap. Based on the results, it can be concluded that both of the proposed controllers meet the requirement of levitating the rotor. It can also be seen that a good correspondence between the simulations and measurements is achieved. From the current RMS values in the steady-state situation we can notice that the LQR controller provides lower current demand. It is pointed out, however, that there is one notable difference between the BMs in the experimental test; the ND-end has a smaller current ripple than the D-end.

5.1 System Identification

As was shown in Fig. 9, both the proposed control approaches provided a stable fully levitated operation of the bearingless machine. Thus, system identification experiments can be carried out when the rotor is levitating by superposing artificially generated excitation signals to the control system. In this paper, an adaptive amplitude stepped sine signal is considered with a frequency band from 1 Hz to 750 Hz in order to validate the suitability of the control approaches for commissioning purposes. System identification experiments are carried out with both control approaches. In Fig. 12, the experimentally obtained frequency responses are shown. Uncertainty is shown in the low frequency area (<10 Hz) as it is challenging to identify the DC-area with the motor inverter. Also the closed loop controller influences to the low frequency region limiting the accuracy of identification. Nevertheless, identified rotor model for both controllers is matching closely to the initial rigid rotor model. Identified rotor model can be further use in the control design where the flexible part is included. Evidently, the system rotor dynamics can be identified in the full-levitation mode similarly as with the 5-DOF AMB system Vuojolainen et al. (2017).

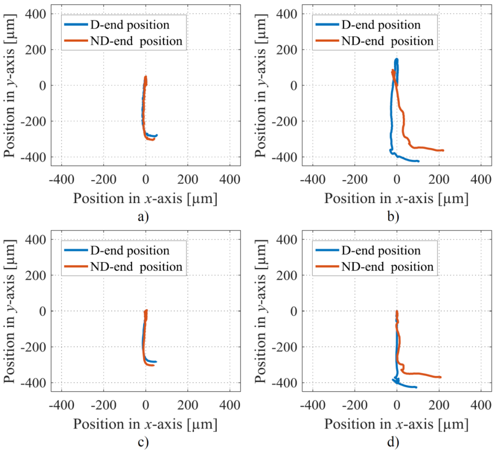

a)
b)
c)
d)

Figure 9: Simulated and measured rotor lift-up from the backup bearings. Initially, the rotor is lying on the backup bearings, and after the controller is enabled, the rotor is magnetically levitated to the operating point, that is the origin $(x, y) = (0, 0)$. Simulation and measurement results for the pole placement controller are shown in a) and b), and for the LQR controller in c) and d).

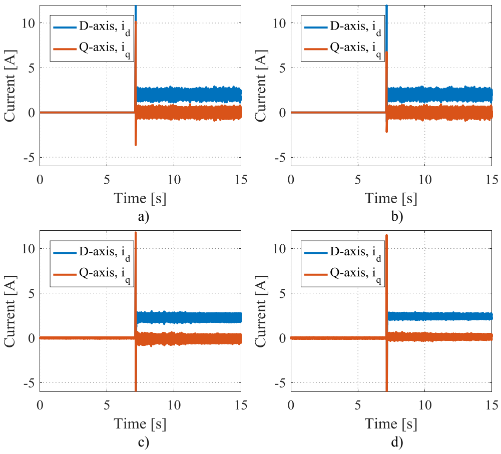

Figure 10: Simulated and measured DQ currents during the rotor lift-up with the pole placement controller. Simulation of the DQ axis current of the D-end and the ND-end motor are shown in a) and b), respectively. The measured DQ axis current of the D-end and the ND-end motor are shown in c) and d), respectively. Steady state RMS values for current in the simulation a) and b) are 2 A. For the measured steady state RMS current values c) 2.3 A and d) 2.4 A.

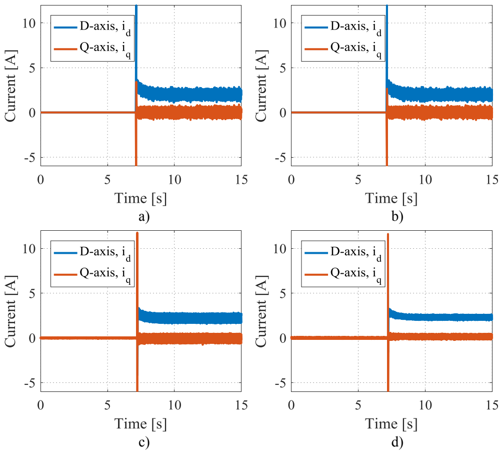

Figure 11: Simulated and measured DQ currents during the rotor lift-up when using the LQR controller. Simulation of the DQ axis current of the D-end and the ND-end motor are shown in a) and b), respectively. The measured DQ axis currents of the D-end and the ND-end motor are shown in c) and d), respectively. Steady state RMS values for current in the simulation a) and b) are 2 A. For the measured steady state RMS current values c) 2.2 A and d) 2.3 A.

5.2 Rotational tests

To further validate the observations reported in this paper, rotational tests are carried out with modest velocity of 150 and 300 r/min. The measured currents from the motor and levitation coils are shown with the measured position during the rotation test for both speeds in Fig. 13 and Fig. 14. Note, that, for illustrative purposes the rotational test are carried out only with the LQR based control approach. These results clearly indicate that the proposed control approach produces stable levitation also during rotation. Torque for the rotation is produced with the D-end motor windings without the decoupling in the levitation controller. The average fluctuation of the positon measurement during the rotation is 2.5 µm, which is caused by the sensor noise and the runout of the sensor surface together with the unbalance of the rotor. By comparing rotor position measurements in Fig. 13 and Fig. 14 it can be noticed that D-end orbit is affected the most from the rotation speed change. Fundamental orbit change of the rotor position with rotor speed from 150 to 300 r/min is for D-end from 2.15 µm to 2.1 µm and for ND-end 4.5 µm to 3.2 µm. Effect of the cross-coupling between the levitation and the torque windings in D-end is seen from the results.

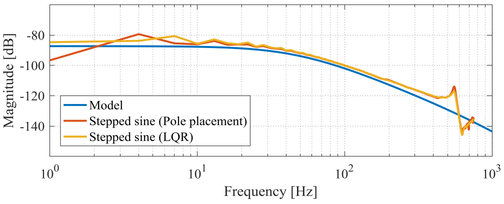

Figure 12: Frequency response plot where the result of the experimental identification with the stepped sine method is compared with the rigid body rotor model. The experimental result shows the first flexible mode peak.

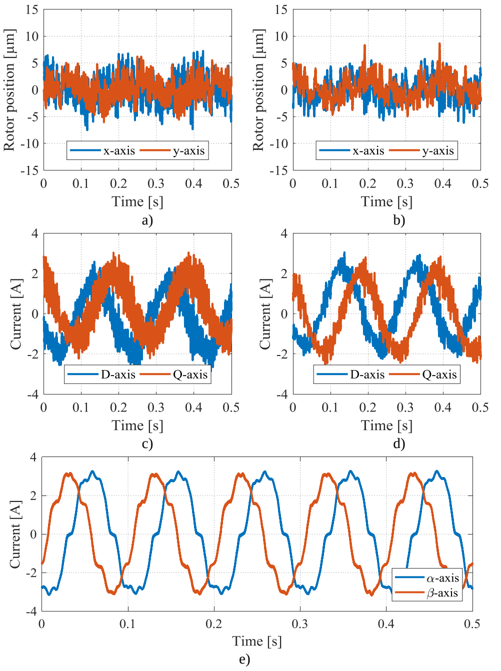

Figure 13: Rotation test with speed of 150 r/min. Measured rotor position is shown for D-end and ND-end in a) and b), respectively. Levitation winding current for D-end and ND-end is shown in c) and d). respectively. Torque producing current in the D-end motor windings is shown in e). The motor currents are represented in $\alpha\beta$ -armature reference frame.

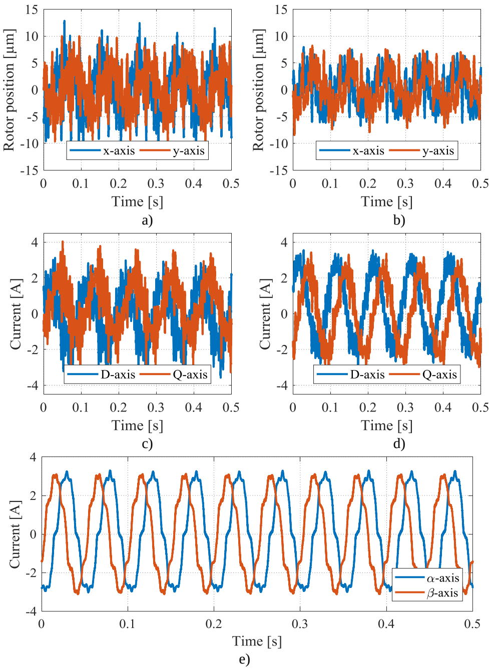

Figure 14: Rotation test with speed of 300 r/min. Measured rotor position is shown for D-end and ND-end in a) and b), respectively. Levitation winding current for D-end and ND-end is shown in c) and d). respectively. Torque producing current in the D-end motor windings is shown in e). The motor currents are represented in $\alpha\beta$ -armature reference frame.

6 Summary of the Commissioning Steps

A summary of the commissioning steps is given to explicate the connection between the proposed control methods and the control system.

- **Step I**: Derivation of the rigid system model (2) using the rotor mass m and the inertia J with the position stiffness K_x and current stiffness K_i parameters obtained from the FEM and validated by experiments (see Fig. 5). To derive the full model used for the control design (10), the inner current controller dynamics (14) is considered.
- **Step II**: MIMO state space controller design considering pole placement or LQR. The initial selection for the pole placement control is to place all the poles in the same location, that is, $z = e^{-\sqrt{\frac{K_x}{m}}\cdot T_s}$, which corresponds to the eigenvalue for a spring-mass-system with a negative stiffness. The LQR can be straightforwardly designed with Bryson's rule by selecting reasonable maximum input signal and output deviation limits for the controller. A good initial selection for the maximum output deviation is to consider smaller values for the deviation than the values given in the ISO standard ISO 14839-2:2004(E) (2004), where the acceptable rotor vibration with respect to the air-gap length in magnetic levitation applications is recommended. Here, a value of 0.083$\cdot C_{min}$ is considered, where C_{min} is the minimum clearance. The maximum levitation current can be used as

the initial value for the input deviation. An acceptable control effort can be achieved by tuning the input deviation, and thus, in this paper, the selected input deviation is 2 A.

- **Step III**: Estimator design (14) based on the system model, The estimator can be tuned by using the general guidelines given for instance in Messager and Binder (2016) , Franklin et al. (2010) so that the observer poles are around 4–10 times faster than the closed-loop poles. Here, a ten times faster design is considered.

- **Step IV**: Check in the simulation that the desired response and dynamics are obtained for the lift-up test (see example in Fig. 9 a) and c)). If the requirements are not met, redesign the controller and the estimator in **Steps II** and **III**.

- **Steps V–VI**: Experimental lift-up test, where the basic functionality of the controller is further verified. After that, identification tests supported with a model validation routine should be carried out. Here, the adaptive amplitude stepped sine Vuojolainen et al. (2017) is used as an excitation signal in the identification experiments.

After the proposed commissioning routine, the natural next step is the controller retuning based on the identified model, if the initial mathematical model does not correspond to the identified one. This step is important, especially if there is some identified dynamics, such as cross-coupling, which should be considered in the final controller design for the rotation over the whole speed range. To this end, previous studies focusing on the control of different bearingless machine applications Zhang et al. (2016), Zhao and Zhu (2017) have shown that PID-based controllers are useful tools for stabilizing a rigid rotor. However, a MIMO controller should be considered as a final controller as it is more straightforward to tune in order to adequately stabilize the complex dynamics in the case of a flexible rotor Yoon et al. (2013). Moreover, in general, when considering a magnetically levitated high-speed motor application with a very high speed requirement, the PID controller has certain shortcomings that can destabilize the system for example if there are flexible modes within the controller bandwidth. When commissioning is carried out with a MIMO controller, the final control law can be designed using the same algorithm straightforwardly. In this case, this ensures a better cooperation between bearingless motors for the stabilization of the system and stable rotational operation over the whole speed range.

7 Conclusion

Commissioning steps for fully levitated bearingless machine using the model based control approach is presented. It is beneficial to apply the MIMO control principles over very traditional PID-based control structures, which do not take into account the coupling of the rotor system. In this paper, it was shown that the well-established MIMO AMB control principles can be straightforwardly applied to a bearingless machine system. By comparing the adopted controllers, it is shown that the LQR outperforms the pole placement controller. Designing an LQR-based controller is much more straightforward as a result of the more intuitive tuning methods. Secondly, weighting-function-based controllers are not sensitive to a model order change as the weights affect the inputs and outputs but not the states themselves. Updating a rigid body rotor model to a flexible model would increase the number of poles to be tuned. Naturally, the pole placement controller is more suitable for simpler systems than a complex MIMO system, such as a 4-DOF levitated rotor system, but in this paper, it was only considered as an example MIMO control case for a bearingless machine.

The results presented in this paper are important as the 5-DOF operation of bearingless machines has not been comprehensively analyzed in the literature thus far. The 5-DOF operation was shown and analyzed with two distinct MIMO control approaches using simple rigid rotor model. The proposed controllers can be applied for commissioning purposes, and it was experimentally shown that artificial-excitation-based system identification experiments can be carried out during full levitation operation. Additionally, stability of the LQR based levitation controller was verified with the low-speed rotation tests.

References

Cao, X., Yang, H., Zhang, L., and Deng, Z. Compensation strategy of levitation forces for single-winding bearingless switched reluctance motor with one winding total short circuited. *IEEE Trans. on Ind. Electron.*, 2016. 63(9):5534–5546. doi:10.1109/TIE.2016.2558482.

Cao, X., Zhou, J., Liu, C., and Deng, Z. Advanced control method for single-winding bearingless switched reluctance motor to reduce torque ripple and radial displacement. *IEEE Trans. Energy Convers.*, 2017. PP(99):1–1. doi:10.1109/TEC.2017.2719160.

Chen, L. and Hofmann, W. Modelling and control of one bearingless 8-6 switched reluctance motor with single layer of winding structure. In *14th European*

Conf. on Power Electron. and Appl. (EPE). pages 1–9, 2011.

Chiba, A., Fukao, T., Ichikawa, O., Oshima, M., Takemoto, M., and Dorrell, D. G. *Magnetic bearings and bearingless drives*, pages 1–15. Elsevier, Amsterdam, The Netherlands, 2009. doi:10.1016/B978-0-7506-5727-3.X5000-7.

Chiba, A., Horima, S., and Sugimoto, H. A principle and test results of a novel bearingless motor with motor parallel winding structure. In *IEEE Energy Convers. Congr. and Expo. (ECCE)*. pages 2474–2479, 2013. doi:10.1109/ECCE.2013.6647019.

Franklin, G. F., Powell, J., and Workman, M. L. *Digital control of dynamic systems*, pages 364, 400–401. Ellis-Kagle Press, 1200 Pilarcitos Ave. Halfmoon Bay, CA 94019, 2010.

Gerhard Schweitzer, E. H. M. *Magnetic bearings*, pages 1–82. Springer-Verlag Berlin Heidelberg, Springer-Verlag Berlin Heidelberg, 2009. doi:10.1007/978-3-642-00497-1.

Hoshi, H., Shinshi, T., and Takatani, S. Third-generation blood pumps with mechanical non-contact magnetic bearings. *Artificial Organs*, 2006. 30(5):324–338. doi:10.1111/j.1525-1594.2006.00222.x. Cited By 153.

Huang, J., Li, B., Jiang, H., and Kang, M. Analysis and control of multiphase permanent-magnet bearingless motor with a single set of half-coiled winding. *IEEE Trans. on Ind. Electron.*, 2014. 61(7):3137–3145. doi:10.1109/TIE.2013.2279371.

ISO 14839-2:2004(E). Mechanical vibration – Vibration of rotating machinery equipped with active magnetic bearings – Part 2: Evaluation of vibration. Standard, International Organization for Standardization, Geneva, CH, 2004.

Jaatinen, P., T. Sillanpää, R. J., and Pyrhönen, O. Automated parameter identification platform for magnetic levitation systems: case bearingless machine. In *15th Int. Symp. on Magnetic Bearings*. 2016.

Kauss, W. L., Gomes, A. C. D. N., Stephan, R. M., and David, D. F. B. Lqr control of a bearingless machine implemented with a dsp. In *11th Int. Symp. on Magnetic Bearings*. pages 475–480, 2008.

Kolondzovski, Z., Sallinen, P., Belahcen, A., and Arkkio, A. Rotordynamic analysis of different rotor structures for high-speed permanent-magnet electrical machines. *IET Electric Power Appl.*, 2010. 4(7):516–524. doi:10.1049/iet-epa.2008.0272.

Messager, G. and Binder, A. Observer-based pole placement control for a double conical high-speed bearingless permanent magnet synchronous motor. In *18th European Conf. on Power Electron. and Appl. (EPE)*. pages 1–10, 2016. doi:10.1109/EPE.2016.7695264.

Mitterhofer, H. and Amrhein, W. Motion control strategy and operational behaviour of a high speed bearingless disc drive. In *6th IET Int. Conf. on Power Electron., Mach. and Drives (PEMD)*. pages 1–6, 2012. doi:10.1049/cp.2012.0297.

Noh, M., Gruber, W., and Trumper, D. L. Hysteresis bearingless slice motors with homopolar flux-biasing. *IEEE/ASME Transactions on Mechatronics*, 2017. PP(99):1–1. doi:10.1109/TMECH.2017.2740429.

Ooshima, M., Chiba, A., Rahman, A., and Fukao, T. An improved control method of buried-type ipm bearingless motors considering magnetic saturation and magnetic pull variation. *IEEE Trans. Energy Convers.*, 2004. 19(3):569–575. doi:10.1109/TEC.2004.832065.

Ooshima, M., Kobayashi, A., and Narita, T. Stabilized suspension control strategy at failure of a motor section in a d-q axis current control bearingless motor. In *IEEE Ind. Ind. Soc. Annu. Meeting*. pages 1–7, 2015. doi:10.1109/IAS.2015.7356813.

Qiu, Z., Dai, J., Yang, J., Zhou, X., and Zhang, Y. Research on rotor eccentricity compensation control for bearingless surface-mounted permanent-magnet motors based on an exact analytical method. *IEEE Trans. Magn.*, 2015. 51(11):1–4. doi:10.1109/TMAG.2015.2451163.

Schneider, T. and Binder, A. Design and evaluation of a 60 000 rpm permanent magnet bearingless high speed motor. In *7th Int. Conf. on Power Electron. and Drive Sys. (PEDS)*. pages 1–8, 2007. doi:10.1109/PEDS.2007.4487669.

Severson, E., Nilssen, R., Undeland, T., and Mohan, N. Design of dual purpose no voltage combined windings for bearingless motors. *IEEE Trans. Ind. Appl.*, 2017. PP(99):1–1. doi:10.1109/TIA.2017.2706653.

Smirnov, A. *AMB system for high-speed motors using automatic commissioning.* Ph.D. thesis, Lappeenranta University of Technology, Lappeenranta, Finland, 2012.

Sun, X., Shi, Z., Chen, L., and Yang, Z. Internal model control for a bearingless permanent magnet synchronous motor based on inverse system method. *IEEE Trans. Energy Convers.*, 2016a. 31(4):1539–1548. doi:10.1109/TEC.2016.2591925.

Sun, X., Xue, Z., Zhu, J., Guo, Y., Yang, Z., Chen, L., and Chen, J. Suspension force modeling for a bearingless permanent magnet synchronous motor using maxwell stress tensor method. *IEEE Trans. Appl. Supercond.*, 2016b. 26(7):1–5. doi:10.1109/TASC.2016.2599708.

Swanson, E. E., Maslen, E. H., Li, G., and Cloud, C. H. Rotordynamic design audits of amb supported machinery. In *37th Turbomachinery Symp.* pages 133–158, 2008.

Takemoto, M., Iwasaki, S., Miyazaki, H., Chiba, A., and Fukao, T. Experimental evaluation of magnetic suspension characteristics in a 5-axis active control type bearingless motor without a thrust disk for wide-gap condition. In *IEEE Energy Convers. Congr. and Expo. (ECCE)*. pages 2362–2367, 2009. doi:10.1109/ECCE.2009.5316174.

Vuojolainen, J., Nevaranta, N., Jastrzebski, R., and Pyrhönen, O. Comparison of excitation signals in active magnetic bearing system identification. *Modeling, Identification and Control*, 2017. 38(3):123–133. doi:10.4173/mic.2017.3.2.

Warberger, B., Reichert, T., Nussbaumer, T., and Kolar, J. W. Design considerations of a bearingless motor for high-purity mixing applications. In *SPEEDAM*. pages 1454–1459, 2010. doi:10.1109/SPEEDAM.2010.5545102.

Xue, B., Wang, H., Tang, S., and Liang, J. Levitation performance analysis for bearingless switched reluctance motor. In *18th Int. Conf. on Elect. Machines and Syst. (ICEMS)*. pages 264–270, 2015. doi:10.1109/ICEMS.2015.7385039.

Yamamoto, N., Takemoto, M., Ogasawara, S., and Hiragushi, M. Experimental estimation of a 5-axis active control type bearingless canned motor pump. In *IEEE Int. Electric Machines and Drives Conf. (IEMDC)*. pages 148–153, 2011. doi:10.1109/IEMDC.2011.5994829.

Yang, S. M. and Chen, C. C. Improvements of radial force control for a spm type pmsm self-bearing motor drive (ecce). In *IEEE Energy Convers. Congr. and Expo.* pages 3451–3455, 2009. doi:10.1109/ECCE.2009.5316514.

Yang, Y., Deng, Z., Yang, G., Cao, X., and Zhang, Q. A control strategy for bearingless switched-reluctance motors. *IEEE Trans. Power Electron.*, 2010. 25(11):2807–2819. doi:10.1109/TPEL.2010.2051684.

Yoon, Y., Lin, Z., and Allaire, P. E. *Control of surge in centrifugal compressors by active magnetic bearings*, pages 92–94. Springer-Verlag London, Berlin, Heidelberg, 2013. doi:10.1007/978-1-4471-4240-9.

Zhang, S., Liu, L., Wang, S., Jia, Y., and Qie, C. Complete control of radial suspension force for bearingless induction motors. In *IEEE 11th Conf. on Ind. Electron. and Appl. (ICIEA)*. pages 2180–2184, 2016. doi:10.1109/ICIEA.2016.7603950.

Zhao, C. and Zhu, H. Design and analysis of a novel bearingless flux-switching permanent magnet motor. *IEEE Trans. on Ind. Electron.*, 2017. 64(8):6127–6136. doi:10.1109/TIE.2017.2682018.

Publication VI

Jaatinen, P., Vuojolainen, J., Sillanpää, T., Nevaranta, N., Jastrzebski, R., and
Pyrhönen, O.
Motion control of a dual-motor interior permanent magnet bearingless machine

Reprinted with permission from
Proceedings of the IEEE 18th International Conference on Power Electronics and Motion Control (PEMC), Budapest, Hungary
pp. 717–722, 2018
©2018, IEEE

Motion Control of a Dual-Motor Interior Permanent Magnet Bearingless Machine

Pekko Jaatinen*, Jouni Vuojolainen*, Teemu Sillanpää*, Niko Nevaranta*, Rafal Jastrzebski* and Olli Pyrhönen*
*School of Energy Systems
Lappeenranta University of Technology, Finland, 53850
Email: pekko.jaatinen@lut.fi

***Abstract*—The bearingless machine construction is optimal for high-speed machines as it reduces the axial length of the machine. It is crucial that the vibration levels of the rotor are under control during rotation. In the bearingless machine, the rotor is magnetically levitated with an integrated winding system alongside a standard motor winding. In this paper, a control approach is presented to regulate the rotor position in the radial and axial directions together with the speed control of the machine. The rotor vibration levels are verified by rotational tests.**

I. INTRODUCTION

Currently, there is a growing need for high-speed direct drive motors especially in air compressor applications. The direct drive technology removes the need for a mechanical gear box calling for regular maintenance in traditional high-speed solutions. By replacing the traditional solution with a direct-driven one, the overall efficiency of the system can be improved. Operation in a high-speed region imposes certain requirements on the bearing technology applied. A modern solution is a system with active magnetic bearings (AMBs), which provide contactless suspension. It is an ideal solution for high-speed applications, as it removes mechanical friction present in traditional bearing technologies. Moreover, the contact-free operation reduces the need for regular bearing maintenance. A further benefit is that the rotor system equipped with AMBs is suitable for oil-free environments as no lubrication is needed.

Another type of a magnetic-levitated bearing system is a bearingless or a self-levitating motor [1]. This technology combines the levitation function of AMBs with the torque production of the standard electrical motor. The most common winding structure for the bearingless motor uses two winding sets in the stator unit; the first produces the required levitating force and the second the rotating torque. With this kind of a structure, the bearingless machine can be defined as a multiport machine [2], as the machine itself has several input and output ports. In Fig. 1, a schematic diagram of a multiport machine is shown. As the bearingless machine is a more integrated system, it reduces the overall axial length and the need for power electronic components.

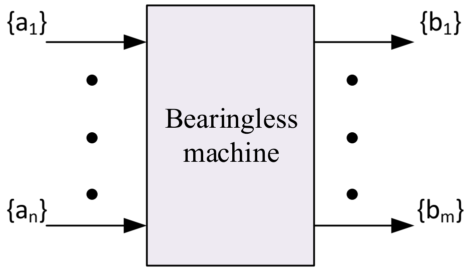

Fig. 1. General description of a multiport machine, where $a_n = [u_n, i_n]$ is a distinct input vector from the motor drive and b_m is the output vector, whose values are application dependent. In a bearingless machine, in general, the outputs are the torque, speed, and rotor position depending on the controlled degrees.

In this paper, the modeling and motion control of a dual-motor interior permanent magnet (IPM) bearingless machine with an additional axial magnetic bearing is presented. A prototype machine, which uses a separate winding configuration for force and torque generation is illustrated and used as an experimental test system. As the system is naturally of a multi-input multi-output (MIMO) type, it is beneficial to use an MIMO-based control approach for the regulation of the rotor radial position instead of a more traditional solution with PID controllers. In this paper, a linear quadratic regulator (LQR) based controller with a disturbance observer is applied to the MIMO control problem. The position of the axial direction is regulated by a separate single-input single-output (SISO) control loop. Moreover, this paper introduces the total configuration of the control system in detail. For torque generation, a centralized scalar U/f control is used as it is suitable for the speed regulation of a high-speed dual motor, where the motor units are on the same shaft [3]. The paper concentrates on the basic functionality of the system, and the system performance is verified with a low-speed test up to 1500 r/min. The rotor of the prototype machine is not prebalanced, and no special surface treatment is applied to the sensor surfaces. Finally, the system performance is studied from the viewpoint of rotor vibration levels, which are compared against ISO standards [4].

978-1-5386-4198-9/18/$31.00 ©2018 IEEE

978-1-5386-4198-9/18/$31.00 ©2018 IEEE

II. SYSTEM DESCRIPTION

A variety of machine configurations that combine AMBs with a bearingless machine have been proposed in the literature. A configuration where one end of the rotor is supported with the AMB and another with a bearingless motor (BM) has been presented in [5], [6]. The prototype machine studied in this paper uses a dual-motor structure similar to [7], [8]. A standard distributed winding construction with short-pitching is used. Contrary to the setup depicted in [8], the presented system uses separate variable frequency drives (VFDs) for torque production. An axial magnetic bearing is added to the center of the rotor to control the axial movement. With this setup, the rotor can be controlled with a five degrees of freedom (5-DOF) configuration. The cross section of the rotor is illustrated in Fig. 2, where the sides of the machine are denoted the drive-end (D-end) and the non-drive-end (ND-end).

In total, five VFDs are needed to control the rotor motion in 6-DOF including rotation. The overall configuration of the VFD setup is shown in Fig. 2. The control system is built by using Beckhoff industrial automation components. The communication between the VFDs, I/Os, and the industrial PC is carried out through an EtherCAT fieldbus. The upper-level block diagram of the control system is depicted in Fig. 3. This control layer includes separate controllers for the motor speed and an axial and radial position control. The sampling time in the industrial PC is 50 µs.

Every VFD is equipped with a custom field programmable gate array (FPGA) board, where the inner control loop is implemented. A simplified block diagram of the inner control loop is shown in Fig. 4. The inner current controller is used in the radial and axial position control and for torque production, and the voltage reference is directly provided to the modulator (simplified in the figure). The measurement system includes eddy-current sensors to attain the rotor radial and axial displacement. Additionally, a rotational encoder is needed, as with this type of a bearingless machine, the direction of the radial force depends on the rotor angle. A vector diagram of the stator and rotor coordinates is presented in Fig. 5. The measured rotor angle θ_r has to be synchronized between the rotor dq-coordinate and the stator xy-coordinate to determine the correct force direction.

III. MODELING AND CONTROL

A model-based control approach is adopted to the regulation of the rotor radial position. Typically, modeling of the dynamics of a high-speed motor application can be divided into three parts; the rotor model, the actuator model, and the force model. If the bandwidth of the actuator, which is the inner current control loop, is high compared with the outer position control loop, it can be neglected. The parameters of the prototype machine are listed in Table II.

General MIMO dynamic equation of the rotor about the center of mass is [9]

$$\mathbf{M}\ddot{\mathbf{q}}(t) + (\mathbf{D} + \Omega\mathbf{G})\dot{\mathbf{q}}(t) + \mathbf{K}\mathbf{q}(t) = \mathbf{F}(t), \tag{1}$$

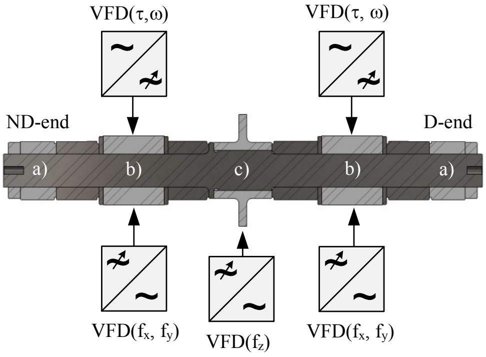

Fig. 2. Block diagram of the variable-frequency drive setup with a cross section of the rotor, where a) is the rotor position measurement surface, b) is the rotor lamination with interior permanent magnets, and c) is the axial disc. The upper VFDs are used for torque/velocity (τ, ω) generation and the lower VDFs to control the position in the x, y, z directions.

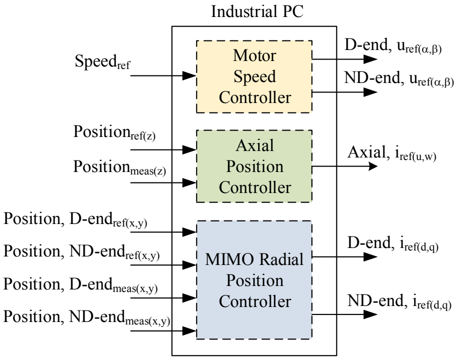
Industrial PC
Speed$_{ref}$
Motor Speed Controller
D-end, u$_{ref(\alpha,\beta)}$
ND-end, u$_{ref(\alpha,\beta)}$
Position$_{ref(z)}$
Position$_{meas(z)}$
Axial Position Controller
Axial, i$_{ref(u,w)}$
Position, D-end$_{ref(x,y)}$
Position, ND-end$_{ref(x,y)}$
Position, D-end$_{meas(x,y)}$
Position, ND-end$_{meas(x,y)}$
MIMO Radial Position Controller
D-end, i$_{ref(d,q)}$
ND-end, i$_{ref(d,q)}$

Fig. 3. Block diagram of the control system with three distinct control loops implemented in the Beckhoff industrial PC. In the motor control loop, a centralized speed controller provides the current reference to both motors. The axial position of the rotor is regulated by a PID controller, and an MIMO controller regulates the radial movement of the rotor at the both ends of the machine. The rotor position is measured in 5-DOF with the eddy-current displacement sensors. The current references provided by the controllers are transferred through an EtherCAT fieldbus to the industrial VFDs.

where $\mathbf{M}$ is the mass matrix, $\mathbf{D}$ is the damping matrix, $\mathbf{G}$ is the gyroscopic matrix, $\mathbf{K}$ is the stiffness matrix, Ω is the rotational speed, $\mathbf{q}$ is the vector of rotor position about the center of mass, and $\mathbf{F}$ is the applied force vector. The rotor equation can be simplified by assuming that the rotor is rigid and gyroscopic coupling is negligible [10]

$$\mathbf{M}\ddot{\mathbf{q}}(t) = \mathbf{F}(t). \tag{2}$$

As the motor and levitation windings are in the same stator unit, a coupling by mutual inductance is present. However, in the steady-state situation, the coupling is constant and it can

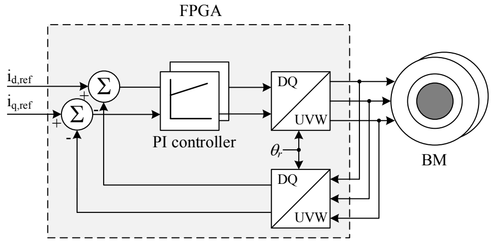

Fig. 4. Block diagram of the inner current control loop. Every VFD contains a custom FPGA control board where the inner PI current control loop is implemented. The rotor electrical angle θ_r, is measured with a contactless magnetic encoder. In the VFD that controls the axial bearing currents, the coordinate transformation is removed.

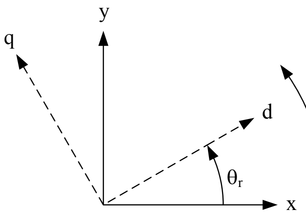

Fig. 5. For the purposes of stable radial force production, the rotor initial electrical angle has to be synchronized with the stator coordinate. At a certain angle, the d-axis current corresponds to the x-axis force and the q-axis current corresponds to the y-axis force. It is also valid at every 90 degrees; however, the direction of force with respect to the xy axes is switched.

be treated as a disturbing force. By treating the coupling as a disturbance, the general force model of a magnetic levitation system can be used [10]

$$\mathbf{F}(t) = \mathbf{K}_x\mathbf{q}(t) + \mathbf{K}_i\mathbf{i}_c(t), \tag{3}$$

where $\mathbf{K}_x$ is the diagonal position stiffness matrix, $\mathbf{K}_i$ is the diagonal current stiffness matrix, and $\mathbf{i}_c$ is the control current vector. The rotor position is presented at the center of mass, and thus, a coordinate transform is needed to change the position into a bearing coordinate

$$\mathbf{q}_b = \begin{pmatrix} -a & 1 & 0 & 0 \\ 0 & 0 & a & 1 \\ -b & 1 & 0 & 0 \\ 0 & 0 & b & 1 \end{pmatrix} \mathbf{q}, \tag{4}$$

where $\mathbf{q}_b$ is the vector in bearing coordinates, a is the drive-end bearing location, and b is the non-drive-end bearing location. By substituting (3) and (4) into (2), the rigid rotor model in the bearing coordinates is obtained

$$\mathbf{M}_b\ddot{\mathbf{q}}_b(t) = \mathbf{K}_{x,r}\mathbf{q}_b(t) + \mathbf{K}_{i,r}\mathbf{i}_c(t). \tag{5}$$

For the purposes of the MIMO control synthesis, the rigid rotor model is presented in the state-space form

$$\begin{aligned} \dot{\mathbf{x}}(t) &= \mathbf{A}\mathbf{x}(t) + \mathbf{B}\mathbf{u}(t) \\ \dot{\mathbf{y}}(t) &= \mathbf{C}\mathbf{x}(t) \end{aligned} \tag{6}$$

where $\mathbf{A}$ is the system matrix, $\mathbf{B}$ is the input matrix, $\mathbf{C}$ is the output matrix, $\mathbf{x}$ is the state vector, $\mathbf{u}$ is the input vector, and $\mathbf{y}$ is the output vector. The rotor model in (5) is transformed into the state-space form

$$\begin{aligned} \mathbf{A} &= \begin{bmatrix} \mathbf{0} & \mathbf{I} \\ -(\mathbf{M}_b)^{-1}\mathbf{K}_x & \mathbf{0} \end{bmatrix}, \\ \mathbf{B} &= \begin{bmatrix} \mathbf{0} \\ -(\mathbf{M}_b)^{-1}\mathbf{K}_i \end{bmatrix}, \\ \mathbf{C} &= \begin{bmatrix} \mathbf{I} & \mathbf{0} \end{bmatrix}, \\ \mathbf{x} &= \begin{bmatrix} x_d & y_d & x_{nd} & y_{nd} & \dot{x}_d & \dot{y}_d & \dot{x}_{nd} & \dot{y}_{nd} \end{bmatrix}^T, \\ \mathbf{u} &= \begin{bmatrix} i_{x,d} & i_{y,d} & i_{x,nd} & i_{y,nd} \end{bmatrix}^T, \\ \mathbf{y} &= \begin{bmatrix} x_d & y_d & x_{nd} & y_{nd} \end{bmatrix}^T. \end{aligned} \tag{7}$$

In order to synthesize the discrete time controller, the plant model has to be discretized. An external disturbance is included in the following discrete state-space model

$$\begin{aligned} \mathbf{x}(k+1) &= \mathbf{\Phi}\mathbf{x}(k) + \mathbf{\Gamma}\mathbf{u}(k) + \mathbf{\Gamma}_d\mathbf{w}(k) \\ \mathbf{y}(k) &= \mathbf{C}\mathbf{x}(k), \end{aligned} \tag{8}$$

where $\mathbf{\Phi}$ is the discretized system matrix, $\mathbf{\Gamma}$ is the discretized input matrix, $\mathbf{\Gamma}_d$ is the discretized disturbance input matrix, and $\mathbf{w}$ is the external disturbance vector.

The obtained discrete state-space equation is used as the plant model in control synthesis. A linear-quadratic regulator (LQR) is used as the feedback controller [11]. The feedback gain $\mathbf{K}$ is calculated by minimizing the quadratic cost function

$$\mathcal{J} = \frac{1}{2}\sum_{k=0}^{N}[\mathbf{x}^T(k)\mathbf{Q}_1\mathbf{x}(k) + \mathbf{u}^T\mathbf{Q}_2\mathbf{u}(k)], \tag{9}$$

where $\mathbf{x}$ is the state vector, $\mathbf{u}$ is the input vector, $\mathbf{Q}_1$ is the state weighting matrix, and $\mathbf{Q}_2$ is the input weighting matrix. The gains are typically selected by trial and error or by using a method with tuning guidelines such as Bryson's rule, where the cost functions are calculated from the maximum deviation of the inputs and outputs [12], [13].

A. Disturbance estimator

As the acceleration cannot be measured directly by eddy-current sensors, a state-estimator is needed. Additionally, the integral action is desired to remove the steady-state error caused by gravity. It is possible to implement a disturbance estimator, which includes both estimator and integral actions. A block diagram of the state feedback radial position controller together with the disturbance estimator is presented in Fig. 6.

Disturbance can be generally modeled in a time-continuous form as [13]

$$\begin{aligned} \dot{x}_d(t) &= \mathbf{A}_d\mathbf{x}_d(t) \\ w(t) &= \mathbf{C}_d\mathbf{x}_d(t), \end{aligned} \tag{10}$$

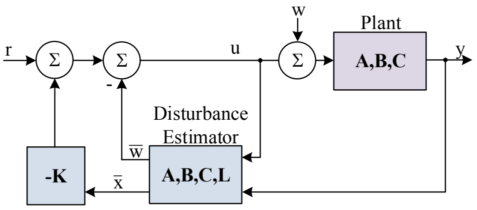

Fig. 6. Block diagram of the state-feedback radial position controller together with the disturbance estimator.

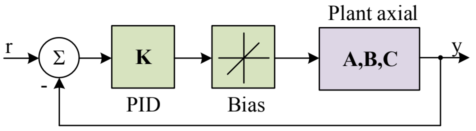

Fig. 7. Block diagram of the axial control loop.

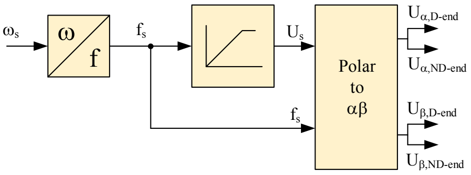

Fig. 8. Block diagram of the scalar U/f motor speed controller.

where $\mathbf{A}_d$ is the system matrix of the disturbance, $\mathbf{C}_d$ is the output matrix of the disturbance, $\mathbf{x}_d$ is the state vector of the disturbance, and w is the output of the disturbance model. The discrete version of the disturbance model can be expressed in the following form

$$\begin{aligned} x_d(k+1) &= \mathbf{\Phi}_d \mathbf{x}_d(k) \\ w(k) &= \mathbf{C}_d \mathbf{x}_d(k), \end{aligned} \tag{11}$$

where $\mathbf{\Phi}_d$ is the discretized system matrix of the disturbance. The disturbance model is incorporated into the system model by substituting 11 in 8 .

$$\begin{aligned} \begin{bmatrix} \mathbf{x}(k+1) \\ \mathbf{w}(k+1) \end{bmatrix} &= \begin{bmatrix} \mathbf{\Phi} & \mathbf{\Gamma}_d \mathbf{C}_d \\ \mathbf{0} & \mathbf{\Phi}_d \end{bmatrix} \begin{bmatrix} \mathbf{x}(k) \\ \mathbf{w}(k) \end{bmatrix} + \begin{bmatrix} \mathbf{\Gamma} \\ \mathbf{0} \end{bmatrix} \mathbf{u}(k) \\ \mathbf{y}(t) &= \begin{bmatrix} \mathbf{C} & \mathbf{0} \end{bmatrix} \begin{bmatrix} \mathbf{x}(t) \\ \mathbf{w}(t) \end{bmatrix} \end{aligned} \tag{12}$$

The steady-state error caused by gravity and the motor windings is constant, and thus, the disturbance model can be simplified to

$$\begin{aligned} \begin{bmatrix} \mathbf{x}(k+1) \\ \mathbf{w}(k+1) \end{bmatrix} &= \begin{bmatrix} \mathbf{\Phi} & \mathbf{\Gamma}_d \\ \mathbf{0} & \mathbf{I} \end{bmatrix} \begin{bmatrix} \mathbf{x}(k) \\ \mathbf{w}(k) \end{bmatrix} + \begin{bmatrix} \mathbf{\Gamma} \\ \mathbf{0} \end{bmatrix} \mathbf{u}(k) \\ \mathbf{y}(t) &= \begin{bmatrix} \mathbf{C} & \mathbf{0} \end{bmatrix} \begin{bmatrix} \mathbf{x}(t) \\ \mathbf{w}(t) \end{bmatrix} \end{aligned} \tag{13}$$

B. *Other Control Loops*

The control loop of the axial magnetic bearing is shown in Fig. 7. When operating in the magnetic center, the regulation of the axial direction position can be treated as a separate SISO control loop. A second-order point-mass plant model is used to calculate the initial gains for the PID controller [1]. In a permanent magnet bearingless machine, the magnets act as a biasing force to generate linear force with respect to the rotor position. However, an axial bearing is a traditional magnetic bearing, where two opposing coils produce the force. To linearize the force generation curve, the bias current is added to both coils.

The speed regulation of the dual-motor configuration is handled with a scalar U/f control. In Fig. 8, a block diagram of the scalar U/f controller is presented. From the reference speed, the corresponding stator reference frame voltages are calculated for both motors.

IV. EXPERIMENTAL VALIDATION

The rotor vibration levels of the prototype machine both in the radial and axial directions were verified by a set of rotational tests from 150 r/min to 1500 r/min. In the prototype machine, the rotor itself was unbalanced, and the measurement surfaces were not polished. There are four sources of rotor vibration; the first is the unbalance mass in the rotor, the second is the run-out caused by the uneven sensor surface, the third is the magnetic cross coupling, and the fourth is mechanical resonanses caused by the motor structure. The fundamental and harmonic components of vibration can compared with respect to the rotation speed by using the fast Fourier transform (FFT) algorithm. The rotor unbalance can be seen in the fundamental frequency as it is in the same phase with the rotational speed. The vibration caused by the run-out can be seen partly in the fundamental frequency and party in the harmonics of the fundamental frequency [14]. Acceptable rotor vibration with respect to the air-gap length in magnetic levitation applications has been recommended in the ISO 14839-2:2004 standard [4]. In Table I, the zone limits for the vibration are given. Zone A is for continuous operation, and the vibration should be less than 30 % of the full air-gap length.

The measured rotor orbit of the both ends of the motor at 1500 r/min is shown in Fig. 9. It can be seen that the orbits are not round, which indicates that there are dominant harmonic components present. The motor and levitation currents of the both ends are presented in Fig. 10. The corresponding current waveforms are seen in the ND-end levitation windings, where the controller compensates the vibration. The vibration level of the axial direction is illustrated in Fig. 11. An increase in amplitude and vibration can be seen in the axial direction

TABLE I
RECOMMENDED CRITERIA OF ZONE LIMITS [4]

Limit	Displacement D_{max}
Zone A	$< 0.3\ C_{min}$
Zone B	$< 0.4\ C_{min}$
Zone C	$< 0.5\ C_{min}$
Zone D	$> 0.5\ C_{min}$

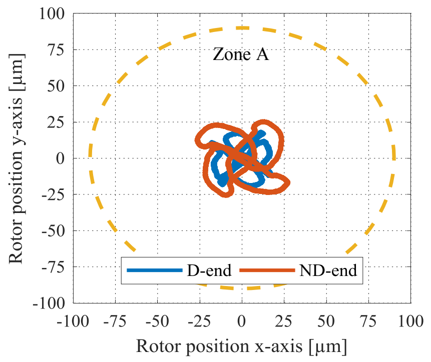

Fig. 9. Orbits of the rotor measured form both ends of the machine at 1500 r/min.

measurement. The vibration is in phase with the rotor mechanical speed, which indicates small cross coupling between the levitation and the motor windings. The frequency spectra of the rotor vibration of the both motor ends have been obtained by the FFT, and they are plotted in Figs. 12 and 13. It is clearly visible that the third harmonic is the dominant one in this speed range.

TABLE II
MACHINE PARAMETERS

Parameter	Symbol	Unit
Motor unit nominal power	P_n	5 kW
Rated speed	ω_n	30 000 r/min
Rated torque	τ_n	1.59 N
Rated voltage, motor	$U_{n,m}$	400 V
Rated current, motor	$I_{n,m}$	8.4 A
Rated voltage, levitation	$U_{n,l}$	400 V
Rated current, levitation	$I_{n,l}$	8 A
Position stiffness, radial	$K_{x,r}$	672 N/mm
Current stiffness, radial	$K_{i,r}$	29 N/A
Position stiffness, axial	$K_{x,a}$	847 N/mm
Current stiffness, axial	$K_{i,a}$	112.9 N/A
Rotor mass	m	11.65 kg
Rotor inertia	J	0.232 kgm^2
BM position	a, b	107.5 mm

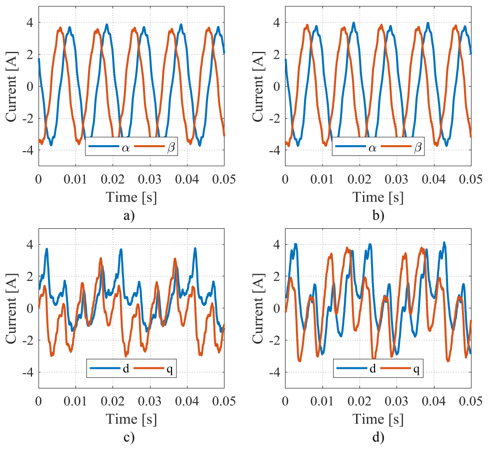

a)
b)
c)
d)

Fig. 10. Measured motor and levitation currents at 1500 r/min where a), c) D-end and b), d) ND-end of the machine.

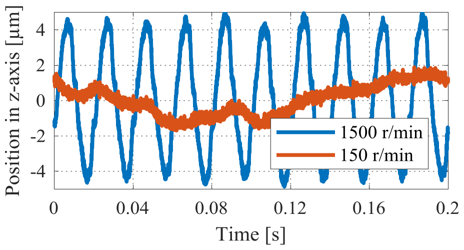

Fig. 11. Rotor vibration in the axial direction at the speeds of 150 r/min and 1500 r/min.

V. CONCLUSIONS

This paper presented an overall framework to implement a model-based radial position control for a dual-motor IPM bearingless machine with an axial magnetic bearing. Even though the U/f scalar control is simple, it is still a practical solution for high-speed applications with a constant operation speed. Rotation tests with a levitated rotor were run from 150 r/min to 1500 r/min. The vibration results show that at low speeds the vibration is mostly caused by the run-out effect. To keep the rotor orbit in a zone A at the nominal speed area, the rotor balancing is needed as the effect of the unbalance grows quadratic in function of rotational speed.

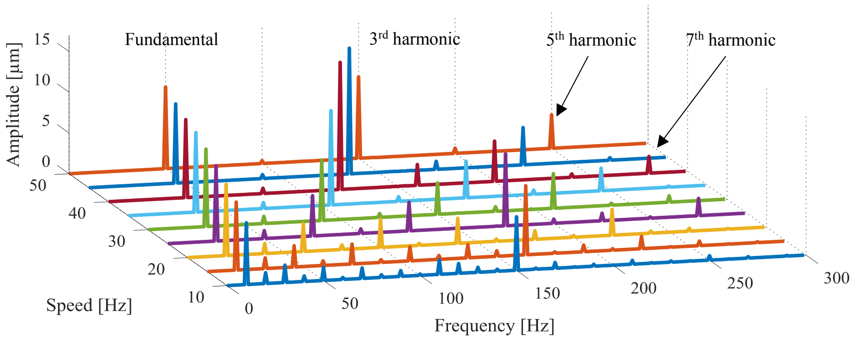

Fig. 12. Frequency spectra of the D-end rotor orbit from 150 to 1500 r/min. Electrical speed is used in the rotational speed axis.

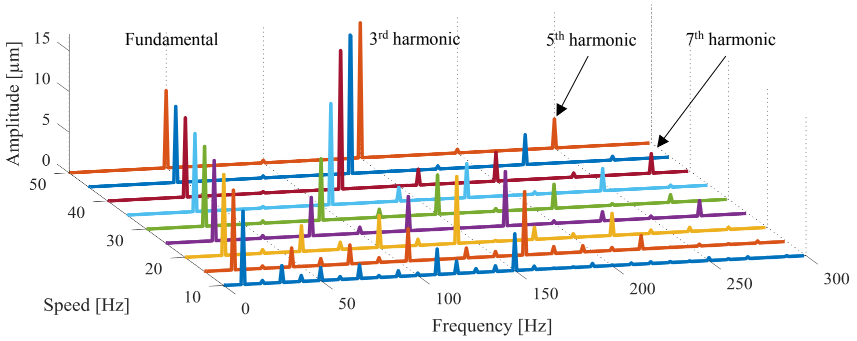

Fig. 13. Frequency spectra of the ND-end rotor orbit from 150 to 1500 r/min. Electrical speed is used in the rotational speed axis.

REFERENCES

[1] A. Chiba, T. Fukao, O. Ichikawa, M. Oshima, M. Takemoto, and D. G. Dorrell, *Magnetic bearings and bearingless drives*, Amsterdam, The Netherlands: Elsevier, 2009.

[2] M. Cheng, P. Han, G. Buja, M. G. Jovanoviċ "Emerging Multi-Port Electrical Machines and Systems: Past Developments, Current Challenges and Future Prospects," *IEEE Trans. on Ind. Electron.*.,vol. 65, no. 7, pp. 5422-5435, Jul. 2018.

[3] T. Halkosaari, "Optimal U/f-control of high speed permanent magnet motors," *IEEE Int. Sym. on Ind. Electron.*, Montreal, Que., pp. 2303–2308, 2006.

[4] ISO 14839-2:2004(en) "Mechanical vibration – Vibration of rotating machinery equipped with active magnetic bearings – Part 2: Evaluation of vibration," *International Organization for Standardization*, Geneva, CH, 2004.

[5] X. Cao, J. Zhou, C. Liu and Z. Deng, "Advanced Control Method for a Single-Winding Bearingless Switched Reluctance Motor to Reduce Torque Ripple and Radial Displacement," in *IEEE Trans. on Energy Convers.*, vol. 32, no. 4, pp. 1533–1543, Dec. 2017.

[7] M. Satoshi, S. Tadashi, O. Masaru, "Experiments on a Bearingless

[6] C. Redemann, P. Meuter, A. Ramella, T. Gempp, "30 kW Bearingless Canned Motor Pump on the Test Bed," Seventh *Int. Symp. on Magnetic Bearings*, ETH Zurich, Switzerland, Aug. 2000.

Synchronous Reluctance Motor with Load," Fifth *Int. Symp. on Magnetic Bearings*, Kanazawa, Japan, Aug. 1996.

[8] M. Ooshima, S. Miyazawa, A. Chiba, F. Nakamura, T. Fukao, "Performance Evaluation and Test Results a 11,000 r/min, 4kW Surface-Mounted Permanent Magnet-Type Bearingless Motor," Seventh *Int. Symp. on Magnetic Bearings*, ETH Zurich, Switzerland, Aug. 2000.

[9] M. I. Friswell, J. E. T. Penny, S. D. Garvey, A. W. Lees, '*Dynamics of rotating machines*, Cambridge University Press, 2010.

[10] E. H. M. Gerhard Schweitzer, *Magnetic bearings*, pp. 1–82. Springer-Verlag Berlin Heidelberg: Springer-Verlag Berlin Heidelberg, 2009.

[11] Y. N. Zhuravlyov,"On LQ-Control of Magnetic Bearing," *IEEE Trans. Control Syst. Technolo.*, vol. 8, no. 2, pp. 344–350, 2000.

[12] R. Jastrzebski, R. Pöllänen and O. Pyrhönen, "Linearization of Force Characteristics of Active Magnetic Bearings for the FPGA-based LQ-controller," *IEEE Int. Conf. on Ind. Tech.* (ICIT), Mumbai, India, pp. 2420–2426, Dec. 2006.

[13] G. F. Franklin, J. Powell, and M. L. Workman, *Digital control of dynamicsystems*, pp. 364, 400–401. 1200 Pilarcitos Ave. Halfmoon Bay, CA94019: Ellis-Kagle Press, 2010.

[14] Cheol-Soon Kim and Chong-Won Lee, "In situ runout identification in active magnetic bearing system by extended influence coefficient method," in *IEEE/ASME Trans. on Mechatronics*, vol. 2, no. 1, pp. 51–57, Mar. 1997.

Publication VII

Jaatinen, P., Nevaranta, N., Vuojolainen, J., Jastrzebski, R., and Pyrhönen, O.
H_∞ control of a dual motor bearingless machine

Reprinted with permission from
Proceedings of the IEEE International Electric Machines and Drives Conference (IEMDC), San Diego, CA, USA
pp. 875–881, 2019
©2019, IEEE

H_∞ Control of a Dual Motor Bearingless Machine

1st Pekko Jaatinen
Department of Electrical Engineering
LUT University
Lappeenranta, Finland
pekko.jaatinen@lut.fi

2nd Niko Nevaranta
Department of Electrical Engineering
LUT University
Lappeenranta, Finland
niko.nevaranta@lut.fi

3rd Jouni Vuojolainen
Department of Electrical Engineering
LUT University
Lappeenranta, Finland
jouni.vuojolainen@lut.fi

4th Rafal Jastrzebski
Department of Electrical Engineering
LUT University
Lappeenranta, Finland
rafal.jastrzebski@lut.fi

5th Olli Pyrhönen
Department of Electrical Engineering
LUT University
Lappeenranta, Finland
olli.pyrhonen@lut.fi

***Abstract*—It is beneficial to use model-based control approaches for the position control of high-speed machines with a magnetically levitated rotor system, as the system inherently involves multiple inputs and outputs. There is always uncertainty in the model parameters, and thus, a robust control approach is a preferable choice. In this paper, an H_∞ loop-shaping method for bearingless machine control synthesis is studied and compared with the widely used PID control approach. System identification experiments are conducted to validate the results and the controller performance in the prototype system.**

***Index Terms*—bearingless machine, identification, MIMO, robust control**

I. INTRODUCTION

High-speed compressors can be equipped with active magnetic bearing (AMB) technology to replace traditional retainer bearings. With AMBs, the rotation speed is only limited by the mechanical strength of the rotor structure. A drawback of AMBs is that they increase the rotor length as the additional active parts require space in the rotor. An alternative option is to apply bearingless or self-levitating motor technology [1]. In this approach, the motor units produce torque together with the levitating force. In a basic construction, this can be achieved by two different winding sets wound on one stator unit. An additional benefit when applying a solution based on bearingless technology is that standard industrial variable frequency drives can also be used for levitation winding control. Hence, a bearingless motor can be designed to be a more integrated system than a traditional AMB rotor system solution, which is beneficial in high-speed applications.

Approaches to control the rotor position in a bearingless machine are generally presented with a PID-based controller [2], [3]. The selection of the PID controller is supported by practical reasons such as the ease of implementation and an intuitive tuning approach. However, an actively levitated rotor system has to be supported with two bearing planes in the radial direction and one plane in the axial direction. This setup constitutes a multi-input multi-output (MIMO) system, where cross-couplings between the controlled axes are present. To effectively control the MIMO rotor system with a PID controller, additional cross-coupling gains must be included. This naturally increases the complexity of the PID controller. By adopting a model-based control approach, cross-coupling can be taken into account directly in the model applied to the control synthesis [4]. The model-based control solution allows the adoption of well-established control approaches such as state feedback with pole placement, optimal control [5], and robust control [6], to name but a few. Further, the same model-based control principles used for traditional AMB solutions can also be applied in the case of bearingless machines [7].

Different robust control methods for the position control of an AMB rotor system have been proposed in the literature. In [8], an H_∞ loop-shaping is considered for a magnetic bearing system. Another paper discusses a signal-based H_∞ control method for an active magnetic bearing application and compares it with loop-shaping in [9]. A mixed sensitivity-based approach for a high-speed machine with AMBs is reported in [10]. Finally, the control of a flexible rotor system using the μ-synthesis method is investigated in [11].

In this paper, the control of a dual motor interior permanent magnet bearingless machine is addressed by employing the H_∞ loop-shaping control method. The modeling of the rotor system is reported. The robustness of the system is analyzed and the results are compared with the standards related to the acceptable limits of mechanical vibrations in AMB systems [12], [13]. The performance of the synthesized multi-input multi-output (MIMO) H_∞ controller is verified by experimental tests on a 10 kW prototype machine. The well-known PID controller is used as a reference controller.

The paper is organized as follows. Section **II** describes the problem statement, and the system under investigation is introduced. Section **II** also approaches system modeling by presenting a MIMO rotor system model. The background theory and uncertainty modeling are discussed in Section **III**. The PID controller configuration applied in the study is described together with the tuning of the 4-DOF H_∞ controller with the loop-shaping method in Section **IV**. The experimental

978-1-5386-9350-6/19/$31.00 ©2019 IEEE

results are given in Section $\mathbf{V}$, where the performance of the H_∞ controller is compared with the PID controller. Section $\mathbf{VI}$ concludes the paper.

II. PROBLEM STATEMENT

A rotor system that is supported in five degrees of freedom constitutes a MIMO system, where cross-coupling between the controlled axes is present. PID-controller-based solutions are widely used in industrial applications, but the drawback of the PID approaches is that their tuning laws are designed for single-input single-output (SISO) systems. To take account of the full system with a PID controller, additional cross-coupling gains are required [1]. With a model-based approach, the MIMO rotor system dynamics can be straightforwardly incorporated in the control synthesis.

The are several standards that define the acceptable operating conditions for high-speed electrical machine application. For instance, the acceptable unbalance of the rotor with respect to the operating speed is studied in [14]. Moreover, the vibration and sensitivity peak of the rotor system equipped with AMBs are investigated in [12], [13]. The sensitivity against disturbances as a function of frequency is a further important performance metric addressed in the standard. By applying the H_∞ control approach, the controller design is carried out directly in the frequency domain by selecting the suitable weighting functions. By correct weight selection, the desired performance can be achieved and the requirements specified in the standards can be met. This paper studies the H_∞ loop-shaping method for bearingless machine control synthesis.

A. System description

The magnetically levitated rotor system under study consists of dual bearingless motor units and an axial AMB. The bearingless motor units include two separate distributed winding sets that generate torque and radial-direction levitation force. The rotor itself consists of two lamination stacks with interior permanent magnets along with the measurement surface for the eddy-current displacement sensors in five degrees of freedom (5-DOF). In addition to the rotor position measurement, the rotor angle is measured with a noncontact magnetic encoder. The position of the axial AMB is controlled with a separate PID controller. A photograph of the prototype machine is shown in Fig. 1. The system is driven with industrial three-phase variable frequency drives equipped with a custom control unit. The inner current control loop is implemented in the variable frequency drive, whereas the position control is implemented in Beckhoff TwinCaT using the Simulink/Matlab environment.

B. System modeling

The basic modeling of the system dynamics of a magnetic levitation system can be approached in two ways. The simplest approach is based on point mass modeling, which describes the basic operation of a magnetically levitated system in one degree of freedom (DOF). The second approach is a rigid body model, which represents the full rotor system in four degrees of freedom. The latter modeling approach combines the rigid rotor model together with a linearized force model. As the model is of the MIMO type, the state-space presentation is a convenient choice for such a system.

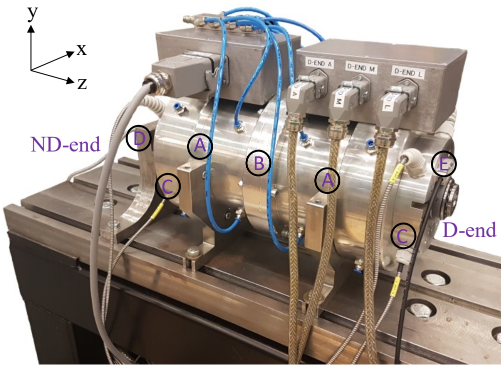

Fig. 1. Prototype machine, where a) is the location of the motor units, b) the location of the axial AMB, c) the measurement planes of the rotor radial position with the eddy-current sensors, d) the measurement of the rotor axial displacement with the eddy-current sensor, and e) the measurement of the rotor angle with a noncontact magnetic encoder.

$$\begin{aligned}\dot{\mathbf{x}}(t) &= \mathbf{A}\mathbf{x}(t) + \mathbf{B}\mathbf{u}(t)\\ \dot{\mathbf{y}}(t) &= \mathbf{C}\mathbf{x}(t),\end{aligned} \tag{1}$$

where $\mathbf{A}$ is the system matrix, $\mathbf{B}$ is the input matrix, $\mathbf{C}$ is the output matrix, $\mathbf{u}$ is the input vector, $\mathbf{x}$ is the state vector, and $\mathbf{y}$ is the output vector. The rotor model can be generally expressed with the equation

$$\mathbf{M}\ddot{\mathbf{q}}(t) + (\mathbf{D} + \Omega\mathbf{G})\dot{\mathbf{q}}(t) + \mathbf{K}\mathbf{q}(t) = \mathbf{F}(t), \tag{2}$$

where $\mathbf{M}$ is the mass matrix, $\mathbf{D}$ is the damping matrix, $\mathbf{G}$ is the gyroscopic matrix, $\mathbf{K}$ is the stiffness matrix, $\mathbf{F}$ is the force vector, and $\mathbf{q}$ is the rotor position around the center of mass. This equation can be simplified by assuming rigid behavior of the rotor, which reduces the system model into

$$\mathbf{M}\ddot{\mathbf{q}}(t) + \Omega\mathbf{G}\dot{\mathbf{q}}(t) = \mathbf{F}(t). \tag{3}$$

A further model simplification can be made by assuming that the rotor is not gyroscopic. This assumption is valid when the rotor axial length is greater than the rotor diameter. By including the linearized force model in the rotor model, an overall model is obtained

$$\mathbf{M}\ddot{\mathbf{q}}(t) = \mathbf{K}_x\mathbf{q}(t) + \mathbf{K}_i\mathbf{i}_c(t), \tag{4}$$

where $\mathbf{K}_x$ is the position stiffness matrix, $\mathbf{K}_i$ is the current stiffness matrix, and $\mathbf{i}_c$ is the control current vector.

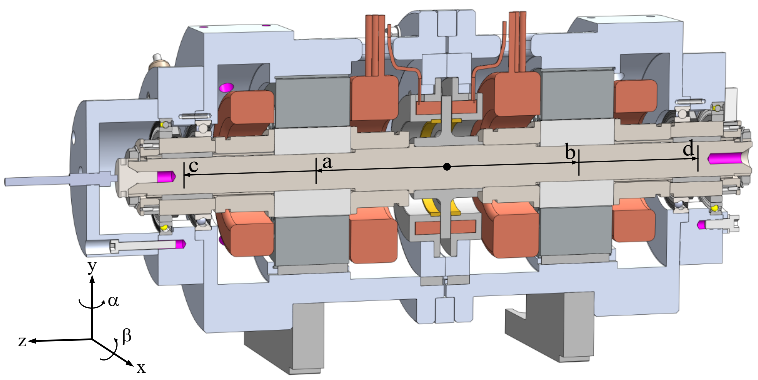

Fig. 2. Cross-sectional view of the prototype machine, where the locations of the motor units (a, b) and the rotor position measurement planes (c, d) are illustrated from the center of mass.

A cross-sectional view of the modeled prototype machine is illustrated in Fig. 2. The rotor movement $\mathbf{q} = \begin{bmatrix}\beta & x & \alpha & y\end{bmatrix}^T$, is presented around the center of mass, where x is the rotor position in the x-axis, α is the angle around the y-axis, y is the rotor position in the y-axis, and β is the angle around the x-axis, respectively. The control current vector is in the motor reference frame, whereas the rotor position is measured in different locations (reference frame). For this reason, the coordinate transformation matrices are needed to transfer the inputs and the outputs to the corresponding coordinate system

$$\mathbf{T}_{bc} = \begin{pmatrix} a & 0 & -b & 0 \\ 1 & 0 & 1 & 0 \\ 0 & a & 0 & -b \\ 0 & 1 & 0 & 1 \end{pmatrix}, \quad \mathbf{T}_{cs} = \begin{pmatrix} c & 1 & 0 & 0 \\ 0 & 0 & c & 1 \\ -d & 1 & 0 & 0 \\ 0 & 0 & -d & 1 \end{pmatrix}, \tag{5}$$

where $\mathbf{T}_{bc}$ is the transformation from the bearing into the center coordinate and $\mathbf{T}_{cs}$ is the transformation from the center into the sensor coordinate. By combining the coordinate transformations with the overall model, the state-space presentation takes the following form

$$\begin{aligned} \mathbf{A}_r &= \begin{bmatrix} \mathbf{0} & \mathbf{I} \\ (\mathbf{M})^{-1}\mathbf{T}_{bc}\mathbf{K}_x\mathbf{T}_{bc}^{\mathrm{T}} & \mathbf{0} \end{bmatrix}, \\ \mathbf{B}_r &= \begin{bmatrix} \mathbf{0} \\ (\mathbf{M})^{-1}\mathbf{T}_{bc}\mathbf{K}_i \end{bmatrix}, \\ \mathbf{C}_r &= \begin{bmatrix} \mathbf{T_{cs}} & \mathbf{0} \end{bmatrix}. \end{aligned} \tag{6}$$

The presented system model takes into account the noncollocated sensor locations [4]. The derived model is used for the control synthesis.

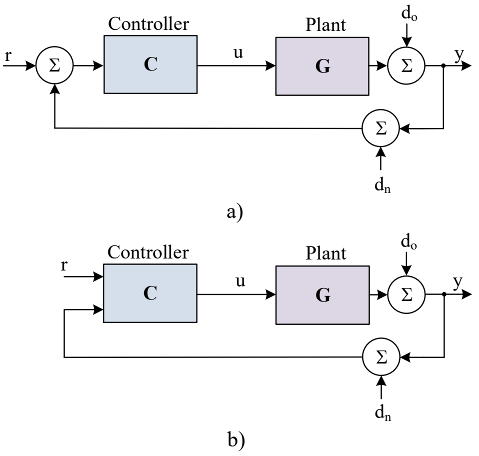

Fig. 3. Upper block diagram illustrates the general feedback control and the lower the two-degree-of-freedom control approach.

III. BACKGROUND THEORY

The objective of the feedback control is to stabilize the system so that it is insensitive to external disturbances and the system follows the reference. The block diagram of a feedback controller is shown in Fig. 3 b). From the figure, the plant can be determined

$$y = \mathbf{G}u + \mathbf{d}_o \tag{7}$$

where $\mathbf{G}$ is the linear plant model, $\mathbf{u}$ is the control input vector, $\mathbf{d}_o$ is the output disturbance, and $\mathbf{y}$ is the output vector. By closing the feedback loop we can get

$$\mathbf{y} = \mathbf{G}\mathbf{C}(\mathbf{r} - \mathbf{d}_n - \mathbf{y}) + \mathbf{d}_o \tag{8}$$

where $\mathbf{C}$ is the feedback controller, $\mathbf{r}$ is the reference vector, and $\mathbf{d}_n$ is the sensor noise vector. By solving the output vector $\mathbf{y}$, we obtain

$$\begin{aligned}\mathbf{y} = \underbrace{(\mathbf{I}+\mathbf{GC})^{-1}\mathbf{GC}}_{T(\mathrm{j}\omega)}\mathbf{r} - \underbrace{(\mathbf{I}+\mathbf{GC})^{-1}\mathbf{GC}}_{T(\mathrm{j}\omega)}\mathbf{d}_n \\ + \underbrace{(\mathbf{I}+\mathbf{GC})^{-1}}_{S(\mathrm{j}\omega)}\mathbf{d}_o,\end{aligned} \tag{9}$$

where the output is described with respect to reference, sensor noise, and output noise. In general, the transfer function $T(j\omega)$ refers to the complementary sensitivity and $S(j\omega)$ to the output sensitivity. The main challenge of the control design is introduced in (9), where the feedback control gains $\mathbf{C}$ should be selected so that the system will follow the reference signal together with the sensor noise attenuation and the output disturbance rejection. This seems to be an ambitious task; however, by inspecting the sensitivity functions in the frequency spectrum it is possible to find a trade-off solution. The sensitivity and complementary sensitivity functions can be used as tools to determine the system stability and robustness.

A. Uncertainty model

In general, the uncertainty of a system can be determined by a structured or an unstructured model. Structured uncertainty describes a certain parameter uncertainty in the model, whereas unstructured uncertainty defines the nonlinearity of the system. Depending on the control problem, a suitable uncertainty model must be selected, where the uncertainty can be an additive, multiplicative, or coprime-factorized perturbation.

In this case, the system model is presented by a coprime factorization method with perturbed uncertainty. The following form represents the left coprime-factorized weighted plant model

$$\begin{aligned}\mathbf{G}_s(s) = \mathbf{M}_s^{-1}(s)\mathbf{N}_s(s) = (\mathbf{M}_s + \mathbf{\Delta}_M)^{-1}(s) \\ + (\mathbf{N}_s + \mathbf{\Delta}_N)(s),\end{aligned} \tag{10}$$

where $\mathbf{G}_s(s)$ is the weighted plant model, $\mathbf{M}_s(s)$ and $\mathbf{N}_s(s)$ are the stable coprime transfer functions, and $\mathbf{\Delta}_N$ and $\mathbf{\Delta}_M$ are the unknown transfer functions that represent the perturbed uncertainty. The block diagram of the left coprime plant model with perturbed uncertainty is depicted in Fig. 4 in the dashed-line box. The control problem is then written as

$$\left\| \begin{bmatrix}\mathbf{K}_2 \\ \mathbf{I}\end{bmatrix} (\mathbf{I} - \mathbf{G}_s\mathbf{K}_2)^{-1}\mathbf{M}_s^{-1} \right\|_\infty \leq \epsilon^{-1} \tag{11}$$

where $\mathbf{K}_2$ is the feedback controller gain, $\mathbf{I}$ is the identity matrix, and ϵ is the stability margin that indicates the maximum perturbation level.

IV. ROTOR POSITION CONTROL

A rotor system whose axial length is greater than its radial diameter must be supported magnetically from two radial bearing locations for stable operation. In addition, to ensure a fully levitated rotor system, the axial direction must be controlled with a passive or active magnetic bearing. In this section, the PID- and H_∞-based controller designs are discussed.

A. PID control approach

To achieve full levitation in 5-DOF with PID controllers, one control loop for the axial direction and four control loops for the radial direction are required. The parallel-form PID controller can be written as

$$\begin{aligned}C_{(PID)}(z) = K_{P_{(PID)}} + K_{I_{(PID)}}\frac{Ts}{z-1} \\ + K_{D_{(PID)}}\frac{T_f}{1+T_f\frac{T_s}{z-1}}\end{aligned} \tag{12}$$

where $C_{(PID)}(z)$ is the PID controller transfer function, $K_{P(PID)}$ is the proportional gain, $K_{I(PID)}$, is the integral gain, $K_{D(PID)}$ is the derivative gain, T_s is the sampling time, and T_f is the time constant of the derivative filter. In this paper, the initial parameter tuning principles for the PID controller are adopted from [1], and the parameters are further tuned against the simulation model followed by final iterative tuning during the experimental test. The control parameters applied in the experimental tests are given in Table I.

B. H_∞ loop-shaping

The H_∞ loop-shaping control approach is used for the radial position stabilization of the MIMO bearingless system. A two-degree-of-freedom controller is selected, where the reference input has a separate weighting function. The block diagram of the 2-DOF control problem is depicted in Fig. 4, where the plant model is coprime factorized [15]. The design process begins by selecting a suitable prefilter $\mathbf{W}_1$ that shapes the open-loop response of the system in the frequency domain

$$\mathbf{G}_s(\mathrm{j}\omega) = \mathbf{G}(\mathrm{j}\omega)\mathbf{W}_1(\mathrm{j}\omega), \tag{13}$$

where $\mathbf{G}(\mathrm{j}\omega)$ is the open-loop plant and $\mathbf{G}_s(\mathrm{j}\omega)$ is the shaped plant. The weighting function $\mathbf{W}_{ref}$ is used to shape the behavior between the reference input and the output

$$\mathbf{W}_{ref}(\mathrm{j}\omega) = \mathbf{I}_{4\times4} \cdot \frac{\omega_{ref}^2}{s^2 + 2\omega_{ref}s + \omega_{ref}^2}, \tag{14}$$

where ω_{ref} is the designed bandwidth for the reference weight. A prefilter is designed to put more weight on the dc gain area to counter the disturbance in this frequency region

$$\mathbf{W}_1(\mathrm{j}\omega) = \mathbf{I}_{4\times4} \cdot \frac{s + w_{a1}}{s + w_{a2}} \cdot \frac{s + w_b}{w_b} \cdot \frac{w_c}{s + w_c} \tag{15}$$

where w_{a1} and w_{a2} are used to define the weight for the low-frequency behavior, and w_b and w_c are used to define the weight around the crossover frequency. With the scalar parameter ρ (see Fig. 4), the weight on the model matching can be further increased.

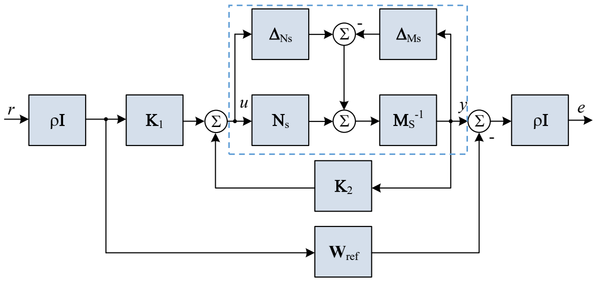

Fig. 4. Block diagram of the H_∞ loop-shaping with the 2-DOF design scheme.

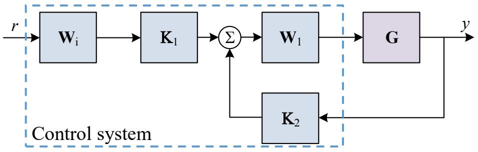

Fig. 5. Block diagram of the implemented H_∞ controller.

The reference input is scaled with the following constant to match the output with the reference model

$$\mathbf{W}_i \triangleq [(\mathbf{I}-\mathbf{G}_s(s))\mathbf{K}_2(s))^{-1}\mathbf{G}_s(s)\mathbf{K}_1(s)]^{-1}\mathbf{W}_{ref}(s)|_{s=0}, \tag{16}$$

where $\mathbf{K}_1$ is the feedback gain and $\mathbf{K}_2$ is the reference gain. The designed and implemented controller takes the form illustrated in Fig. 5.

C. System identification

In this paper, the experimentally identified sensitivity frequency responses are used for the control design validation and comparison. In general, the frequency response can be mathematically described as a relation of the input and output signals

$$G(\mathrm{j}\omega)=\frac{Y(\mathrm{j}\omega)}{U(\mathrm{j}\omega)}, \tag{17}$$

where $Y(j\omega)$ and $U(j\omega)$ are the Fourier-transformed system output and input signals, and $\mathbf{G}(j\omega)$ is the estimated system transfer function. The closed-loop system identification is carried out by including an additional excitation signal designed in a certain frequency range. The output sensitivity of the system can be determined with an experimental identification test, where the excitation signal is injected to the plant output as a disturbance. The sensitivity to the output disturbance is then calculated from the disturbance to the measured output as

$$S(\mathrm{j}\omega)=\frac{Y(\mathrm{j}\omega)}{D_o(\mathrm{j}\omega)} \tag{18}$$

where $Y(\mathrm{j}\omega)$ is the measured system output and $D_o(\mathrm{j}\omega)$ is the artificially generated excitation signal in the frequency domain. In this paper, a pseudorandom binary sequence (PRBS) is considered as an excitation signal that excites the system in the frequency spectrum from 1 to 750 Hz as in [16].

V. EXPERIMENTAL RESULTS

The traditional PID-controller-based solution is compared with the presented 4-DOF MIMO H_∞ approach. Both the controllers are implemented on the Beckhoff industrial PC operating at the 50 μs sampling time. The identified output sensitivity functions for both the controllers are depicted in Fig. 6. It can be seen that the sensitivity peak is lower in the case of the optimized H_∞ controller in Fig. 6 b).

To further analyze the performance, the limits of the sensitivity peaks described in the standard are shown in the output sensitivity plots [14]. In the case of the PID controller system, it can be seen that the sensitivity peak exceeds every limit. On the other hand, the peak of the H_∞ controller is around the A/B zone, which indicates that the output sensitivity should be acceptable in the normal operating point. Moreover, when comparing the experimental output sensitivity results with the simulated ones, we can see that the simulation produces a lower peak. This indicates that the model used for the control design deviates from the actual plant.

To verify the dynamics, the rotor model is identified by injecting a PRBS excitation signal to the current reference signal during the steady-state levitation and measuring the rotor movement with the eddy-current sensors. Thus, the open-loop rotor model can be identified from the signals used in (17). The identification results are illustrated in Fig. 7, where the response from the D-end x axis to the other axes is demonstrated. We can see that the modeled rigid modes correspond well with the identified one shown in Fig. 7 a. However, there is an unmodeled dynamics in the cross-coupling between the other axes. Therefore, to improve the control performance, a more accurate plant model must constructed. This, however,

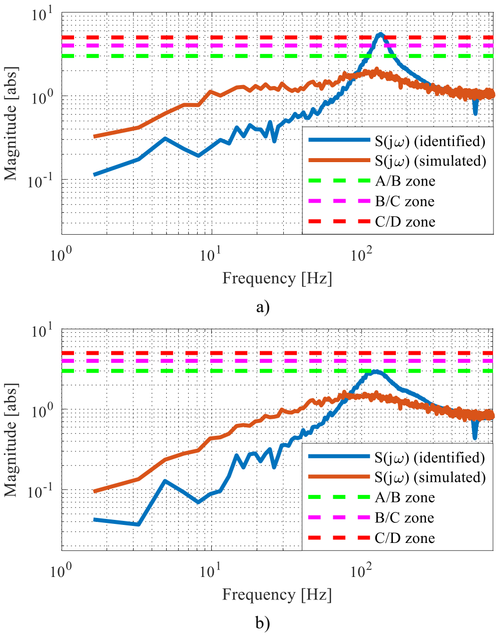

a)

b)

Fig. 6. Identified output sensitivity of the bearingless system controlled with a) PID- and b) H_∞-type controller.

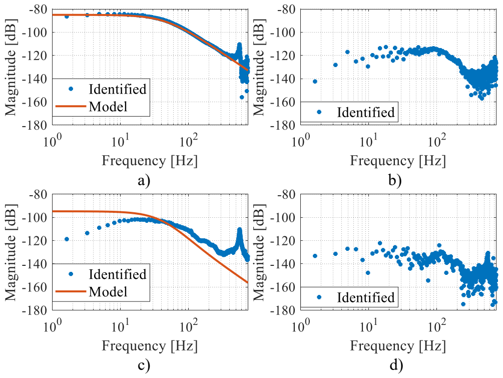

a)

b)

c)

d)

Fig. 7. Identified plant model compared with the analytical model. For simplicity, only one axis of the symmetrical system is illustrated; the subplots are a) D-end x-axis current reference to the D-end x-axis measured position, b) D-end x to D-end y, c) D-end x to ND-end x, and d) D-end x to ND-end.

will be a topic of a future publication. A comparison shows the drawback of the SISO-design-based PID controller solution, where the design does not include the effect of cross-coupling.

TABLE I
SYSTEM PARAMETERS

Parameter	Symbol	Value	Unit
Nominal speed	Ω_{nom}	30 000	r/min
Nominal power per motor unit	P_{nom}	5	kW
Rotor mass	m	11.65	kg
Rotor inertia	J	0.232	kgm^2
Resistance	R	0.27	Ω
Inductance	L	3.27	mH
Current stiffness	K_i	29	N/A
Position stiffness	K_x	672	N/mm
Distance to sensor location	c, d	211	mm
Distance to bearingless motor	a, b	107.5	mm
Sampling time	T_{s}	50	μs
Proportional gain	K_{P}	42000	A/m
Integrator gain	K_{I}	$8.2{\cdot}10^5$	As/m
Derivative gain	K_{D}	103	A/ms
Filter coefficient	T_{f}	100	
Prefilter parameter	w_{a1}	150	
Prefilter parameter	w_{a2}	0.1	
Prefilter parameter	w_{b}	600	
Prefilter parameter	w_{c}	800	
Reference model bandwidth	ω_{ref}	370	rad/s
Scalar gain	ρ	1	

VI. CONCLUSION

In this paper, an H_∞-based MIMO controller was applied to the radial position control of the dual-motor bearingless machine. The controller output sensitivity was used for performance evaluation in terms of standards provided for the actively controlled levitating systems. Additionally, the PID-based controller was used as a reference control law and compared with the proposed H_∞ design. For the validation purposes, the sensitivity functions from both control approaches were identified with experimental identification tests. The results of the experimental tests show that the H_∞ approach outperforms the PID controller. It was found that the identification results demonstrated unmodeled dynamics in the system model. The future work focuses on the system-identification-based modeling issues to improve the control synthesis and the system closed-loop behavior.

REFERENCES

[1] A. Chiba, T. Fukao, O. Ichikawa, M. Oshima, M. Takemoto, and D. G. Dorrell, *Magnetic bearings and bearingless drives*. Amsterdam, The Netherlands: Elsevier, 2009, pp. 1–15.

[2] J. Huang, B. Li, H. Jiang, and M. Kang, “Analysis and control of multiphase permanent-magnet bearingless motor with a single set of half-coiled winding,” *IEEE Transactions on Industrial Electronics*, vol. 61, no. 7, pp. 3137–3145, July 2014.

[3] M. Ooshima, A. Kobayashi, and T. Narita, “Stabilized suspension control strategy at failure of a motor section in a d-q axis current control bearingless motor,” in *2015 IEEE Industry Applications Society Annual Meeting*, Oct 2015, pp. 1–7.

[4] E. H. M. Gerhard Schweitzer, *Magnetic bearings.* Springer-Verlag Berlin Heidelberg: Springer-Verlag Berlin Heidelberg, 2009, pp. 1–82.

[5] Y. N. Zhuravlyov, "On lq-control of magnetic bearing," *IEEE Transactions on Control Systems Technology*, vol. 8, no. 2, pp. 344–350, March 2000.

[6] R. P. Jastrzebski, A. Smirnov, O. Pyrhoönen, and A. K. Piat, "Discussion on robust control applied to active magnetic bearing rotor system," in *Challenges and Paradigms in Applied Robust Control*, A. Bartoszewicz, Ed. Rijeka: IntechOpen, 2011, ch. 10.

[7] P. Jaatinen, J. Vuojolainen, N. Nevaranta, R. Jastrzebski, and O. Pyrhönen, "Control System Commissioning of Fully Levitated Bearingless Machine," *Modeling, Identification and Control*, vol. 40, no. 1, pp. 27–39, 2019.

[8] M. Fujita, K. Hatake, and F. Matsumura, "Loop shaping based robust control of a magnetic bearing," *IEEE Control Systems Magazine*, vol. 13, no. 4, pp. 57–65, Aug 1993.

[9] R. P. Jastrzebski, K. Hynynen, and A. Smirnov, "Case study comparison of linear $h\infty$ loop-shaping design and signal-based $h\infty$ control," in *2009 XXII International Symposium on Information, Communication and Automation Technologies*, Oct 2009, pp. 1–8.

[10] A. Noshadi, J. Shi, W. S. Lee, P. Shi, and A. Kalam, "System identification and robust control of multi-input multi-output active magnetic bearing systems," *IEEE Transactions on Control Systems Technology*, vol. 24, no. 4, pp. 1227–1239, July 2016.

[11] A. Mystkowski, "μ-synthesis control of flexible modes of amb rotor," in *ASME Smart Materials, Adaptive Structures and Intelligent Systems*, vol. 1, Sep 2009.

[12] ISO 14839-2:2004(E), "Mechanical vibration – Vibration of rotating machinery equipped with active magnetic bearings – Part 2: Evaluation of vibration," International Organization for Standardization, Geneva, CH, Standard, Mar. 2004.

[13] ISO 14839-3:2004(E), "Mechanical vibration – Vibration of rotating machinery equipped with active magnetic bearings – Part 3: Evaluation of stability margin," International Organization for Standardization, Geneva, CH, Standard, Mar. 2004.

[14] ISO 1940-1:2003(E), "Mechanical vibration – Balance quality requirements for rotors in a constant (rigid) state – Part 1: Specification and verification of balance tolerances," International Organization for Standardization, Geneva, CH, Standard, Aug. 2003.

[15] S. Skogestard and I. Postletwaite, *Multivariable feedback control analysis and design.* John Wiley Sons, 2001, pp. 372–376.

[16] J. Vuojolainen, N. Nevaranta, R. Jastrzebski, and O. Pyrhönen, "Comparison of Excitation Signals in Active Magnetic Bearing System Identification," *Modeling, Identification and Control*, vol. 38, no. 3, pp. 123–133, 2017.

ACTA UNIVERSITATIS LAPPEENRANTAENSIS

841. BELIAEVA, TATIANA. Complementarity and contextualization of firm-level strategic orientations. 2019. Diss.

842. EFIMOV-SOINI, NIKOLAI. Ideation stage in computer-aided design. 2019. Diss.

843. BUZUKU, SHQIPE. Enhancement of decision-making in complex organizations: A systems engineering approach. 2019. Diss.

844. SHCHERBACHEVA, ANNA. Agent-based modelling for epidemiological applications. 2019. Diss.

845. YLIJOKI, OSSI. Big data - towards data-driven business. 2019. Diss.

846. KOISTINEN, KATARIINA. Actors in sustainability transitions. 2019. Diss.

847. GRADOV, DMITRY. Experimentally validated numerical modelling of reacting multiphase flows in stirred tank reactors. 2019. Diss.

848. ALMPANOPOULOU, ARGYRO. Knowledge ecosystem formation: an institutional and organisational perspective. 2019. Diss.

849. AMELI, ALIREZA. Supercritical CO2 numerical modelling and turbomachinery design. 2019. Diss.

850. RENEV, IVAN. Automation of the conceptual design process in construction industry using ideas generation techniques. 2019. Diss.

851. AVRAMENKO, ANNA. CFD-based optimization for wind turbine locations in a wind park. 2019. Diss.

852. RISSANEN, TOMMI. Perspectives on business model experimentation in internationalizing high-tech companies. 2019. Diss.

853. HASSANZADEH, AIDIN. Advanced techniques for unsupervised classification of remote sensing hyperspectral images. 2019. Diss.

854. POPOVIC, TAMARA. Quantitative indicators of social sustainability applicable in process systems engineering. 2019. Diss.

855. RAMASAMY, DEEPIKA. Selective recovery of rare earth elements from diluted aqueous streams using N- and O –coordination ligand grafted organic-inorganic hybrid composites. 2019. Diss.

856. IFTEKHAR, SIDRA. Synthesis of hybrid bio-nanocomposites and their application for the removal of rare earth elements from synthetic wastewater. 2019. Diss.

857. HUIKURI, MARKO. Modelling and disturbance compensation of a permanent magnet linear motor with a discontinuous track 2019. Diss.

858. AALTO, MIKA. Agent-based modeling as part of biomass supply system research. 2019. Diss.

859. IVANOVA, TATYANA. Atomic layer deposition of catalytic materials for environmental protection. 2019. Diss.

860. SOKOLOV, ALEXANDER. Pulsed corona discharge for wastewater treatment and modification of organic materials. 2019. Diss.

861. DOSHI, BHAIRAVI. Towards a sustainable valorisation of spilled oil by establishing a green chemistry between a surface active moiety of chitosan and oils. 2019. Diss.

862. KHADIJEH, NEKOUEIAN. Modification of carbon-based electrodes using metal nanostructures: Application to voltammetric determination of some pharmaceutical and biological compounds. 2019. Diss.

863. HANSKI, JYRI. Supporting strategic asset management in complex and uncertain decision contexts. 2019. Diss.

864. OTRA-AHO, VILLE. A project management office as a project organization's strategizing tool. 2019. Diss.

865. HILTUNEN, SALLA. Hydrothermal stability of microfibrillated cellulose. 2019. Diss.

866. GURUNG, KHUM. Membrane bioreactor for the removal of emerging contaminants from municipal wastewater and its viability of integrating advanced oxidation processes. 2019. Diss.

867. AWAN, USAMA. Inter-firm relationship leading towards social sustainability in export manufacturing firms. 2019. Diss.

868. SAVCHENKO, DMITRII. Testing microservice applications. 2019. Diss.

869. KARHU, MIIKKA. On weldability of thick section austenitic stainless steel using laser processes. 2019. Diss.

870. KUPARINEN, KATJA. Transforming the chemical pulp industry – From an emitter to a source of negative CO2 emissions. 2019. Diss.

871. HUJALA, ELINA. Quantification of large steam bubble oscillations and chugging using image analysis. 2019. Diss.

872. ZHIDCHENKO, VICTOR. Methods for lifecycle support of hydraulically actuated mobile working machines using IoT and digital twin concepts. 2019. Diss.

873. EGOROV, DMITRY. Ferrite permanent magnet hysteresis loss in rotating electrical machinery. 2019. Diss.

874. PALMER, CAROLIN. Psychological aspects of entrepreneurship – How personality and cognitive abilities influence leadership. 2019. Diss.

875. TALÁSEK, TOMÁS. The linguistic approximation of fuzzy models outputs. 2019. Diss.

876. LAHDENPERÄ, ESKO. Mass transfer modeling in slow-release dissolution and in reactive extraction using experimental verification. 2019. Diss.

877. GRÜNENWALD, STEFAN. High power fiber laser welding of thick section materials - Process performance and weld properties. 2019. Diss.

878. NARAYANAN, ARUN. Renewable-energy-based single and community microgrids integrated with electricity markets. 2019. Diss.

LUT
University

ISBN 978-952-335-442-5
ISBN 978-952-335-443-2 (PDF)
ISSN-L 1456-4491
ISSN 1456-4491
Lappeenranta 2019